5-2017

Investigation of FeS2 Nanoparticles for Use in Optoelectronic and Thermoelectric Applications

Rick Tefal Eyi Nkoghe
University of Arkansas, Fayetteville

Investigation of FeS_2 Nanoparticles for Use in Optoelectronic and Thermoelectric Applications

A dissertation submitted in partial fulfillment
of the requirements for the degree of
Doctor of Philosophy in Engineering

by

Rick Tefal Eyi Nkoghe
Dublin City University
Master of Engineering in Electronic Systems, 2008
ESIGELEC
French Engineering Diploma in Embedded Systems, 2009

May 2017
University of Arkansas

This dissertation is approved for Recommendation to the Graduate Council

_____
Omar Manasreh, PhD
Dissertation Chair

_____
Simon Ang, PhD
Committee Member

_____
Jingyi Chen, PhD
Committee Member

_____
Roy McCann, PhD
Committee Member

DEDICATION

To my mum, my fiancée and my daughter.

ACKNOWLEDGEMENTS

I would like to express my gratitude to my supervisor, Prof. Omar Manasreh for the opportunity he gave me to pursue my PhD in his lab, the optoelectronic lab at the university of Arkansas. For all the support and guidance, he provided me throughout my research. I want to thank him for allowing the opportunity to visit other labs to do experiments and gain knowledge I could not in our lab, that ultimately help me complete my research

I would like to thank every single member I had the pleasure the meet while being at the optoelectronic lab: Jiang, Scott, Scott 2, Reddy, Yahia, Mahmoud, Ramesh, Sanghametra, Ahmed, Mohamed, Juan, and especially Seungyong for all the amazing discussions we had in the office.

I would like to thank Prof. Andreu Cabot of the Catalan Institute of Energy Research (IREC) for the opportunity he gave me to be part of his lab and for his continuous support while being there and even once I came back. I would like to give a special thanks to Maria, who guided me through my first ever hot injection synthesis. Her and Alexey were always available when I had questions related to chemistry. I would like to thank the members of the functional nanomaterials group at IREC: Alex, Fan, Wenhua, Doris, Raquel, Zhishan, Xuelian, Silvia, Joana, Adriana, Gihan, Oleksandr, Taisia.

I would like to thank Prof. Raymond Rumpf of the EmLab at the University of Texas at El Paso for the opportunity he gave me to be part of his lab and for his continuous support while being there and even once I came back. I like to thank members of the EmLab: Ubi, Carlos, Jose, Edgar, Noel, Eric, Nancy, Mark and especially Jesus for the conversations in the office.

I would like to thank all my amazing friends in Fayetteville, Barcelona and El Paso for making my stay in their cities so much better. I would like to thank the Feland Family, Ginger and John for their continuous help.

To finish I would like to thank my mother for being such an amazing person and my fiancée Rachel for all the support and the attention she provided during these years.

ABSTRACT

Iron pyrite (FeS_2) is the most abundant sulfide material on earth. This material has been widely investigated by researchers because of its optical properties. However, it has been difficult to produce High efficiency FeS_2 based solar cells. This is due to many different impurities that arise when making the materials. The ability to synthesize pure pyrite FeS_2 material is therefore critical for applications.

Pure Iron pyrite nanocrystals were synthesized using hot injection by mixing sulfur with an iron precursor in the presence of an amine. To improve the stability, shorter ligands replaced the native amines ligands. The stability of the iron pyrite after ligand exchange was investigated by looking at the changes in the properties of films deposited by spray pyrolysis before and after being stored in air and at room temperature for one year. Even when being deposited at high temperature, the pyrite films were not sulfur deficient. Quenching the PL emission of the nanocrystals and increasing their dark current was observed after ligand exchange. This was detrimental for the solar cells.

The use of FeS_2 for thermoelectrics was investigated because of its metal like conductivity. The nanoparticles were once again synthesized and the native ligands replaced. The nanoparticles were dried to make a powder and pressed to make pellets. Their thermoelectric properties were measured. The seebeck coefficient of the pellets showed a p-type conductivity and the highest value of the ZT in the 10^{-3}. To increase the ZT, the nanocrystals were doped for the first time with cobalt using a two-step hot injection method. The thermoelectric properties of the doped nanoparticles were measured. The ZT showed an increase of 2 order of magnitude, the highest reported ZT from iron pyrite.

To increase the optical properties of the iron pyrite, the nanoparticles were coupled with gold and silver. The idea was to use the plasmonic effect to enhance the optical properties. Absorption spectra and PL spectra were obtained before and after coupling. No significant changes were observed in the optical properties after the coupling. Finite difference frequency domain simulation was used to simulate the behavior.

TABLE OF CONTENTS

LIST OF TABLES

LIST OF FIGURES

ABBREVIATIONS

Oleylamine: OLA

Hexadecylamine: HDA

Oleic Acid: OA

Dimethylformamide: DMF

X-ray Power Diffraction: XRD

Perfectly Matched Layer: PML

CHAPTER 1: INTRODUCTION

The global energy consumption is expected to increase drastically in the next 50 years, thus there is a need to find ways to increase our production of energy. This has traditionally been accomplished by a more extensive use of fossil fuels, such as oil, gas or coal. The problem, however, is that there is a limited usable amount of these types of fuel and their prices depend on many external parameters. Fossil fuels are the primary source of greenhouse gas emissions, which slowly damage the ozone layer. To tackle the increasing energy demand and at the same time reduce the greenhouse gas emissions, research is undergoing in renewable or green sources of energy.

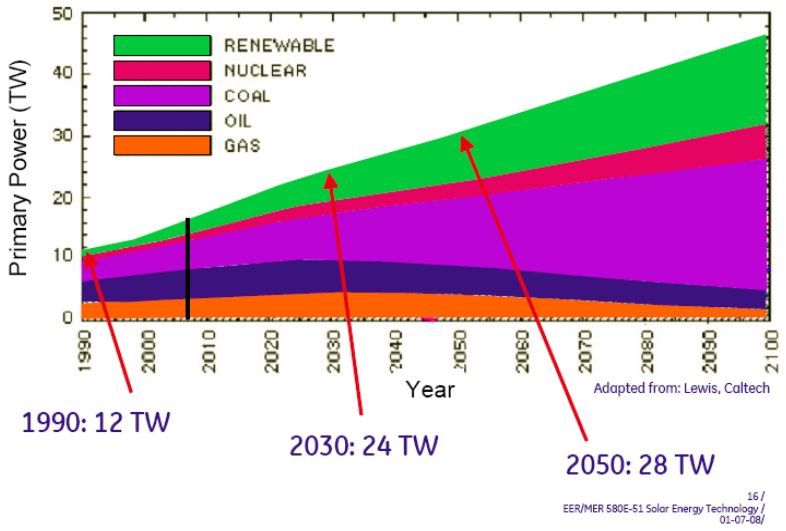

Figure 1: Power that the world needs since 1990 and its projection [1]

As it can be seen from Figure 1, the world will need to find how to produce an extra 13 TW [1] to meet its needs by 2050. Solar energy potential looks to be the best way to produce this extra power with its 120,000 TW. So far, due to its price and its low efficiency, solar cells cannot compete with fossil fuels for terrestrial applications. Second generation solar cells or thin films solar cells significantly reduced the cost of materials [2]. However, even if the efficiency of thin

film solar cells is lower than the efficiency of the first generation; it is somehow compensated by the price reduction of the materials used. Even with the second generation, solar cells have still significantly higher prices than fossil fuels. To achieve the price goal, two approaches can be taken. The first approach is the use of cheap material, the second approach is the use of less expensive fabrication processes.

Bulk silicon solar cells or first generation solar cells make up 90% of the solar cell market with efficiency ranging from 15 to 22% [2]. The only problem is that they use expensive fabrication procedures. Thin film solar cells were introduced to reduce the cost per watt of bulk silicon solar cell modules. The principle was to use less material to reduce the price. Thin film solar cells technology is based on amorphous silicon [3], [4] and also cells made up of chalcogen materials [5]–[10]. Thin film technology also comes with its package of problems; the low efficiency of amorphous Si, the toxicity of Cd and Pb and the scarcity of tellurium and indium being the primary issues. Indium is a byproduct of the extraction of zinc. This makes the process of recovery of indium expensive. Indium is also widely used in the vast majority of flat panel displays [10–11]. One other chalcogen based solar cell with more abundant material was investigated to further decrease the price of the solar cells. The materials that composed these types of cells are copper, zinc, tin and the chalcogen selenium and/or sulfur; they form $Cu_2ZnSn(Se,S)_4$ or CZTS [13] when combined. The highest efficiency so far is 11.1 % [9] and it was reported by *Mitzi et al.* at IBM T. J. Watson research center for $Cu_2ZnSn(Se,S)_4$. The efficiency is still low, but it was achieved using a solution process technique instead of a vacuum technique. Researchers have been focusing on finding new materials to reduce the current cost of electricity of solar cells to compete with fossil fuels and other alternative energy.

One material that scientists have been looking at is FeS_2 or iron pyrite. Iron pyrite is the most common sulfide, making it a commercially attractive material. Other benefits include its non-toxicity, adequate bandgap and high absorption coefficient [14]. Despite the fact that research for solar cell applications of iron pyrite has started over two decades ago [15], the cell efficiencies are still really low. The culprit is the difficulty to make pure iron pyrite. Even a small presence of different iron to sulfur ratios or the presence of marcasite or orthorhombic phase of FeS_2 is detrimental for the cell efficiency. Also, the stability of FeS_2 films is an issue as they tend to lose sulfur rapidly. To solve the purity problem, it is imperative to separate the nucleation process from the growth process when synthesizing iron pyrite nanocrystals. The nucleation process first involves the formation of FeS [16] and after a short period of time, more sulfur enters into the crystal to make FeS_2. For the stability of the films, surface passivation with different ligands seems to work [16–17]. Since the stability of FeS_2 is so critical for its applications, this report will only focus on ways to achieve stability of FeS_2 nanoparticles and films and how these techniques affect the electrical and the optical properties of the films. Three approaches were explored for this purpose. The first approach is done by using of ligands, the second is done by doping FeS_2 nanoparticles with cobalt and the last approach is accomplished by coupling the nanoparticles with metallic (Au and Ag) nanocrystals. For the doping, how it affects the electrical properties of the materials will be investigated. The possible use of the doping material in thermoelectric application will also be investigated. For the coupling method, it will be investigated if the metallic nanocrystals act as traps for the photogenerated carriers. In the event, such phenomenon occurs, it will be studied if the plasmonic effects overcome the effect of such traps. This investigation could help further decrease the thickness of the active layer of thin film solar cell or some other optoelectronic devices and further decrease their cost.

CHAPTER 2: LITERATURE REVIEW

This chapter will present state of the art research in iron pyrite. The first part of this chapter will deal with two applications of iron pyrite that will be presented in this report. These two applications are thermoelectric and photovoltaic. Iron pyrite is used in multiple applications such as li-on battery, formation of sulfur and sulfuric acid from coal mining and catalytic applications but it was decided to just focus on photovoltaics and thermoelectrics. The second part of the chapter will deal with the material itself. Its characteristics, the different methods that are used to synthesize the material and the problems encountered when using iron pyrite.

2.1. Applications

The world will need to find how to produce almost 13 TW to meet its need for 2050. The world will also have to consider global warming; a way to produce this extra energy without increasing greenhouse emission will need to be considered. Green power is the best solution to do so. Iron pyrite has potential in two green power or renewable energy applications, namely photovoltaic and thermoelectric.

The Solar energy with its 120,000 TW potential could be a good way to produce this power. So far due its high price and its low efficiency, the first-generation solar cells (crystalline silicone generation) cannot compete with fossil fuels. Therefore, the goals are to reduce the price and improve the efficiency. The low cost of iron pyrite associated with its high absorption coefficient could help achieve these two goals.

Thermoelectric modules do not have the same potential as photovoltaic but most of the energy generated by other forms of energy, especially fossil fuels, is wasted in the form of heat. The need to save this waste heat by transforming it into electricity is what makes thermoelectric so attractive. Unlike photovoltaic modules, thermoelectric modules do not need to compete with

any other forms of energy for the waste heat conversion. The efficiency does not need to be that high, it just needs to be around 10% with a reasonable price. Here again, the low cost of iron pyrite is one of the key reasons for its investigation.

The fundamentals of photovoltaic will now be presented, followed by the different types of solar cells. The fundamental of thermoelectric will be presented afterward, followed by the ways to improve the efficiency of thermoelectrics.

2.1.1. Solar Cell

This part will first present the principles of solar cells and the important parameters of solar cells. This will be followed by a discussion about the different type of solar cells.

Principles of solar cells

A Photovoltaic module or solar cell is a device that converts solar energy into electrical energy. To do so, the cells need to absorb photons from the light to generate photogenerated carrier pairs. These photogenerated carriers (hole and electrons) can only be dissociated at the junction between a p type and n type semiconductor, also known as the p-n junction. This process is shown in Figure 2

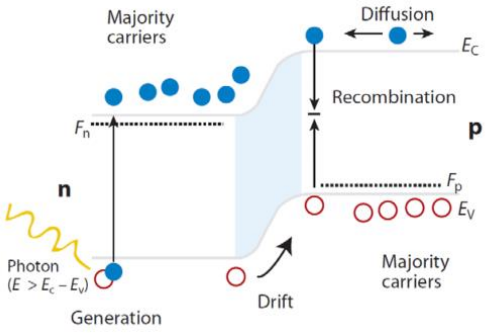

Figure 2: Mechanism of photogenerated carriers at the p-n junction [19]

As it can be seen from Figure 2, for the photon to be absorbed, its energy has to be higher than the bandgap, the energy difference between the lowest point of the conduction band and the highest point of the valence band of the semiconductor. If a photon with energy higher than the bandgap is absorbed, an electron (blue circles in the graph) is promoted from the valence band to the conduction. The electron leaves behind a hole. These two form the photogenerated electron-hole pair that will recombine unless separated.

The pair can only be separated if it reaches the p-n junction. There is a build-up potential difference between the p side and the n side of the p-n junction. This electric field will drive the two opposite charge carriers in different directions. The movement of opposite charge carriers will generate a difference of potential between the two sides of the solar cell and this will induce current flow. The curve of the current as a function of the voltage is the I-V curve and it is an important parameter for solar cells. An example of a solar cell I-V curve is presented in Figure 3

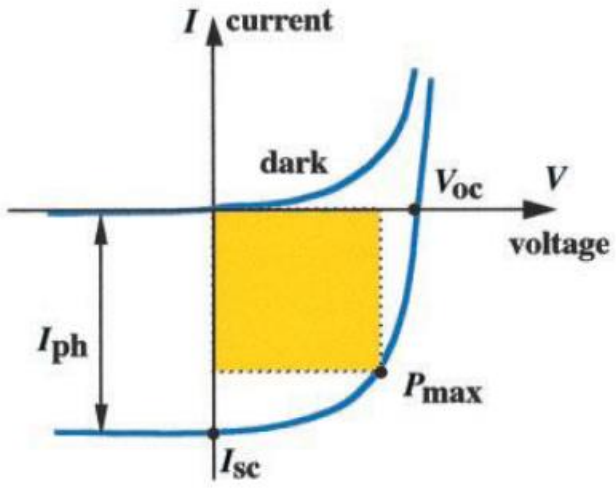

Figure 3: Representation of an I-V curve of a solar cell, this graph represents the variation of the current and the voltage when the light beam shines the material [20]

Air Mass (AM), it represents the volume of air that has uniform properties in term of temperature. It is used to see the amount of sunlight which reaches the surface.

Open-circuit voltage (V_{oc}), it represents the maximum voltage across the cells when there is no current flowing.

Short-circuit current (I_{sc}), it represents the current when the two electrodes of the device are short-circuited.

Maximum Power Point ($P_{\max}$): it represents the possible maximum power produced by the solar cell. It an I-V curve, it is the rectangle with the largest area. In the graph, it is the yellow rectangle. It is the product of maximum power point voltage V_{mpp} with the maximum power point current I_{mpp}.

Fill Factor (FF): it is the ratio between the maximum power point and the product between I_{sc} and V_{oc}.

$$\mathrm{FF} = \frac{I_{mpp} * V_{mpp}}{I_{sc} * V_{oc}} \quad (1)$$. It is an important parameter when describing the performance of the solar cell. The power conversion efficiency (PCE or η_e), which represents the percentage of the power that is really converted.

$$\eta_e = \frac{I_{mpp} * V_{mpp}}{P_{in}} = \frac{I_{sc} * V_{oc} * FF}{P_{in}} \quad (2).$$

After having presented the parameters of solar cells, the different types of solar cells can now be presented.

The different types of solar cells

Silicon, because of its abundance and the maturity of the silicon industry, is the material mainly used for solar cells [4], [20]. The problem with silicon made solar cells stems from the low absorption coefficient of the material [21]. Cells with thick (in the order of hundreds of microns) active layers must be produced. To avoid recombination of the electron hole pair because of impurities, high quality silicon single crystal films must be grown using expensive vacuum techniques. These types of thick active layer solar cells are the first-generation solar cells. To reduce the cost of first generation solar cells, the second-generation solar cells were introduced. The idea was to use less material in the active layers. Therefore, the other name of the second generation is thin film solar cells. The thickness of the active layer prevents the use of indirect low absorption coefficient materials such as silicon. The two materials that dominates the thin film spectrum are cadmium telluride (CdTe) and copper indium gallium disulfide or diselenide [Cu(In, Ga)S/Se_2]. They have cells with efficiencies [3], [22]–[27] in par with the best efficiencies of single crystal silicon solar cells for a fraction of the production cost. Thin film technology even enable solution processed solar cells to further decrease the production price [6], [28]. Thin film modules made of CdTe are even already successfully commercialized by First solar. However, the scarcity of tellurium and the toxicity of the heavy element cadmium represents a drawback for these cells. In the case of CuInGa(S, $Se)_2$ just like in the case of CdTe earlier, the problem comes from the scarcity of some of the material used in the process. Indium is a byproduct of the extraction of zinc, this makes the process of recovery of indium expensive. Taking this into consideration, and the fact that indium is also widely used in transparent conductive oxide in flat panel displays, makes it difficult to achieve the goal of 100 GW per year with CuInGa(S, $Se)_2$ based solar cells [10]. The vast majority of these flat panel displays uses indium tin oxide (ITO) [11] or indium

gallium zinc oxide (IGZO)[12]. The other copper chalcogenide, copper thin zinc sulfide or selenide (CZTS) and iron pyrite could use their abundance to position themselves but their efficiencies still need a boost especially in the case of iron pyrite. The new hot material for thin film solar cells is the hybrid inorganic-organic perovskite materials. The problem is that so far cells are not stable, but the lab efficiencies are high.

2.1.2. Thermoelectric

The need to find alternative ways to generate energy has fueled the research in renewable energy such as thermoelectric energy, solar energy, hydroelectric energy, wind energy, biomass and so on. Thermoelectric modules still have efficiencies not reaching the doubled digit [29] preventing its use to become mainstream, despite the potential in numerous applications [30]–[32]. A significant increase of the efficiency is needed before seeing an increase in the use of thermoelectrics in everyday applications. The fact that thermoelectric can transform waste heat energy into a useful energy [33] further increases the possible applications. One such application is to convert the waste heat generated by the car engines to make cars more fuel efficient. The idea is therefore to improve the efficiency of the thermoelectric modules and just like solar cells to reduce their cost. The efficiency of a thermoelectric module is measured by how long the module can keep a difference in temperature between its two sides. It is also measured on how fast electrons travel from one side to the other. There are basically two principles for thermoelectric. A difference in voltage can generate a difference in temperature, this is called the Seebeck effect. A difference in temperature can generate a difference in voltage, this is the Peltier effect. The factor that measures the quality of the thermoelectric material is what is called figure merit or (ZT).

The expression of the figure of merit is $ZT = \frac{\sigma S^2}{\kappa} T$ (3), where S, σ, T, κ are respectively,

the Seebeck coefficient, the electrical conductivity the temperature in Kelvin and the thermal conductivity [34]. Where the expression of the Seebeck coefficient is, $S = \frac{\Delta V}{\Delta T}$ (4). The formula of *ZT* shows that to have an efficient module, the electrical conductivity needs to be high but the thermal conductivity should be low. This makes perfect sense. The high conductivity will generate high current and generate more energy and the low thermal conductivity will keep the temperature difference for a long period. Another parameter that is often used is the power factor, $PF = S^2\sigma$ (5). Therefore the power factor has to be high and the thermal conductivity small [35–39] to have a high power factor. To improve the efficiency, the power factor needs to be increased while at the same time keeping κ constant or decreasing it. The carrier concentration is directly related to PF and can be increased by doping the material and phonon blocking can be used to decrease the thermal conductivity. After a threshold, further increase of *ZT* becomes complicated because of the non-independence of all its parameters. For example, the electrical conductivity is proportional to the thermal conductivities through the Wiedemann-Franz law, $\frac{\kappa}{\sigma} = LT$ (6) [40], where L is the Lorenz number. To further improve the *ZT*, people focus on either trying to decrease the thermal conductivity [30], [41], [42] or increasing the power factor by various techniques [37], [38], [43–45].

The reduction othe thermal conductivity is done using complex structure such as photon-glass electron-crystal (PGEC) [30] and alloys [35]. Alloying reduces the thermal conductivity because the resulting conductivity is lower than the conductivity of the material with the lowest conductivity. And the crystal of the PGEC induces phonon blocking. The thermal conductivity can also be reduced by using nanostructuring [46–50]. The photon blocking is done by the ground boundaries.

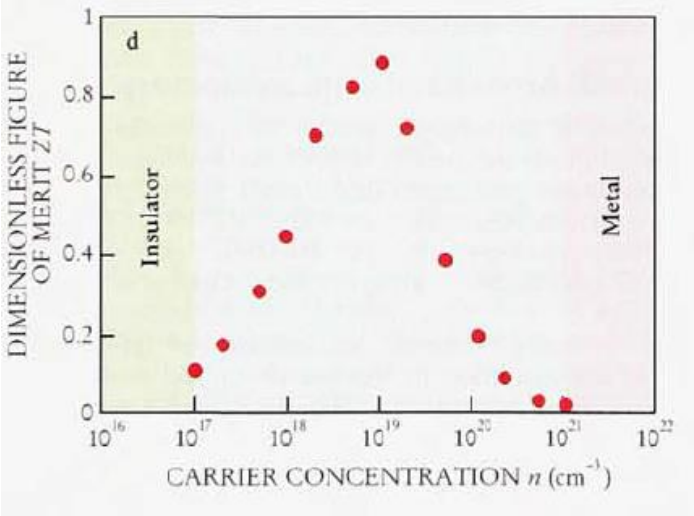

Figure 4: Figure of merit as a function of the carrier concentration [51]

The enhancement of the power factor is done by increasing of the carrier concentration. This is achieved by doping. High *ZT* happens for highly doped material. The idea in this report is to use the doping to increase the PF and the nanostructuring to reduce the thermal conductivity. Now, it is time to look at iron pyrite, characteristics, synthesis and problems.

2.2. FeS_2

Iron pyrite also known as fool's gold is the most abundant sulfide material on earth and for this reason it is also the secondary source of sulfur on earth after elemental sulfur. Iron pyrite is so common that is present in many other sulfides. It is also present in coal. During the extraction of coal, it reacts with water to form sulfuric acid. This is the cause of the acidity of multiple rivers near coal mine. Iron pyrite because of its photovoltaic and catalytic properties has the potential to be used in many different applications such has solar cells, batteries (already used in energizer batteries), hydrogen generation, photocatalytic and even more recently thermoelectric because of the high electrical conductivity caused by its impurities. To achieve the full potential of iron pyrite, it is imperative to synthesize pure iron pyrite and to solve its stability issues. There are multiple

iron to sulfur ratios. Also FeS_2 has another phase beside the pyrite phase. It is important to synthesize/make pure iron pyrite material for optimum potential.

They are different methods to synthesize iron pyrite, chemical vapor transport (CVT), chemical vapor deposition (CVD), hot injection method, heat up method, spray pyrolysis and hydrolysis.

In this first part of literature review chapter, the characteristics of iron pyrite will first be presented, followed by the ways to synthesize the material and to finish by the possible problems of iron pyrite. The second part of the chapter will deal with the different application of the iron pyrite that will be discussed in this report, photovoltaic and thermoelectric.

Characteristics

Iron pyrite as already mentioned is the most abundant sulfide on the Earth crust. It is a semiconductor with an indirect bandgap, but because of its d band [the electronic configuration $Fe^{2+}(3d^6)S^{2-}(3S^4 3p^{10})$], it has a high absorption coefficient in the visible region. The absorption coefficient represents, the amount of light that can be absorbed by a particular thickness of a material. The higher the absorption coefficient, the lower the thickness required to absorb all the light. Generally, indirect bandgap materials just like silicon, have a low absorption coefficients [19–21]; therefore higher thicknesses are needed for solar cells made of silicon. While direct bandgap materials have high absorption coefficients [22–25] and require thinner films for the same amount of absorbed light. This principle is not the case for iron pyrite, which despite its indirect bandgap behaves just like a direct bandgap material in the visible region of the solar spectra.

Iron pyrite, has a Pa3 non-symmorphic [58], [59] with a lattice constant is around $5.417 \mathring{A}$. Iron pyrite has a cubic primitive lattice. The iron atoms are at the positions of the fcc lattice and the centers of the sulfur atoms forming the dumbbell are also at the position of the fcc lattice[60].

The distance between the two sulfur atoms of the dumbbell is $2.16\mathring{A}$. The distance between iron and sulfur is $2.263\mathring{A}$ [61]. The position of all the atoms in the lattice of the cubic iron pyrite is presented in the Tab. 1. The parameter u is equal to 0.386 for iron pyrite[60].

F	S
	(u,u,u)
	$(-u,\ -u,\ -u)$
$(0,\ 0,\ 0)$	$\left(u-\frac{1}{2},-u+\frac{1}{2},-u\right)$
$\left(0,\ \frac{1}{2},\ \frac{1}{2}\right)$	$\left(-u+\frac{1}{2},u-\frac{1}{2},u\right)$
$\left(\frac{1}{2},\ 0,\ \frac{1}{2}\right)$	$\left(-u,\ u-\frac{1}{2},\ -u+\frac{1}{2}\right)$
$\left(\frac{1}{2},\ \frac{1}{2},\ 0\right)$	$\left(u,\ -u+\frac{1}{2},\ -u+\frac{1}{2}\right)$
	$\left(-u+\frac{1}{2},\ -u,\ u-\frac{1}{2}\right)$
	$\left(u-\frac{1}{2},\ u,\ -u+\frac{1}{2}\right)$

Table 1: Position of the atom in the iron pyrite crystal [60]

The crystal structure of iron pyrite has been characterized using XRD. Iron pyrite, because it is so common on the earth crust, was one of the first structure to be analyzed using XRD by W. Lawrence Bragg in the beginning of the 20th century [62]. A typical XRD of iron pyrite is presented in Figure 5. The results- are similar to the reference number JCPD 024-0076 with the peaks at 28.5, 33, 37, 40, 47, 56, 59, 61, 64, 76 and 78 representing respectively the (111), (200), (210), (211), (220), (311), (220), (023), (321), (331), and (420) orientations.

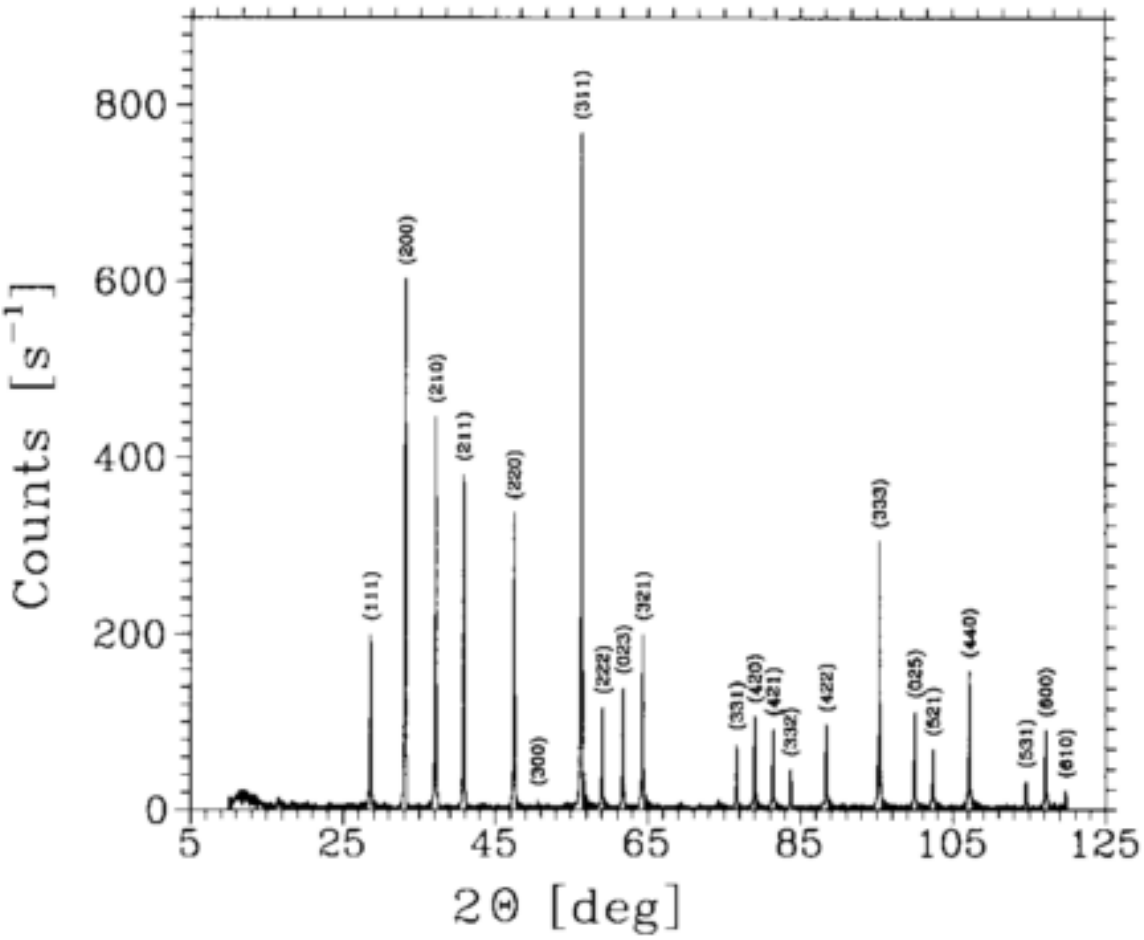

Figure 5: X-ray diffraction of iron pyrite [63]

To further characterize the material, the infrared lattice vibrations of the iron pyrite were calculated by doing reflectivity at room temperature at an angle near the normal angle of incidence. Pyrite structure has 12 atoms in the primitive cell, 4 iron atoms and 8 sulfur atoms. This configuration allows 3 acoustical and 33 optical vibration modes [29–31]. The reflectivity is analyzed by representing the infrared active modes as a damped classical oscillator [26], [32–34]. This fitting allows the calculation of the high frequency dielectric constant; therefore, allowing the calculation of the long wavelength transverse optical (TO) and the longitudinal optical (LO) modes.

The 36 possible displacements of the atom of the unit cell can be decomposed into:

$$\Gamma = A_g + E_g + 3T_g + 2A_u + 2E_u + 6T_u \quad (7)$$

$$\Gamma_{IR} = 5T_u \quad (8)$$

$$\Gamma_{inactive} = 2A_u + 2E_u \quad (9)$$

$$\Gamma_{acoustic} = T_u \text{ (Rigid lattice translation)} \quad (10)$$

$$\Gamma_{Raman} = A_g + E_g + 3T_g \quad (11)$$

The iron atom being almost twice as heavy as the sulfur atom, it almost does not participate in the raman vibrations. The center on inversion being at midpoint, the two sulfur atoms of the dumbbell have to move in opposite directions with the same amplitude while Fe remains still [69], [70]. The different raman vibration modes of iron pyrites are presented below.

A_g mode (symmetric)

The two sulfur atoms of the dumbbell pair perform stretching on the dumbbell plane and this movement is in phase throughout the entire crystal.

E_g mode (double degenerate)

The two sulfur atoms move in a direction perpendicular to the dumbbell plane. The phonons are said to be in libration [71].

T_g mode (triply degenerate)

It's a combination of stretchings and librations. The main restoring force is the interaction between the different atoms. The frequencies of the different modes are presented in the Table 2. Some peaks are difficult to observe when doing experiments because of their proximity with another bigger peak. One of such peaks is the T_g peak at 377 cm^{-1}, because it is close to the peak at 379 cm^{-1}. Another such peak if the peak at 350 cm^{-1}, because of its proximity to the peak at 343

cm^{-1}. The different peaks are also presented in Figure 6. The raman in the figure are measured at different angles of incidence and the scattered electric fields. The strength of the different peaks depends on the orientation, and the direction of the electric fields.

A_g	379
T_g	377
E_g	343
T_g	350
T_g	430

Table 2: Raman active vibration modes of iron pyrite [58]

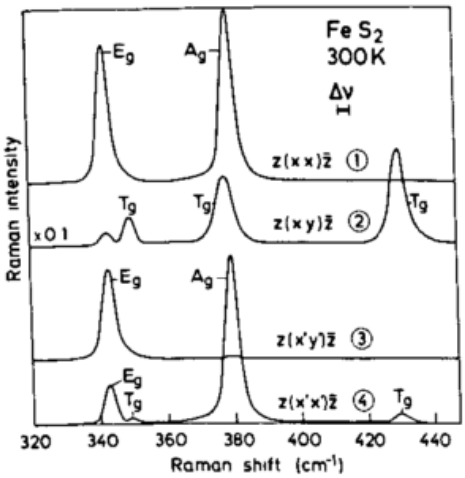

Figure 6: First order Raman spectra of FeS_2 [58]

The absorption coefficient of iron pyrite has been calculated from reflectivity measurement using ratio record technique. The Tauc plots were used to calculate the direct and indirect bandgap of iron pyrite, using $(\alpha.h\nu)^{1/2}$ for indirect bandgap and $(\alpha.h\nu)^2$ for direct bandgap. The indirect bandgap of the iron pyrite is around 0,9 eV, giving a Queissner limit of around 20% efficiency possible [72]. Two direct bandgaps at around 1.5 and 2.4 eV were also found. The absorption coefficient and the Tauc plots are presented in Figure 7. It shows an absorption coefficient around

1.8 * 10^5 cm^{-1} in the visible region [400 nm - 700 nm]. The high absorption coefficient in the visible region is due to the position of these two direct bandgaps in the visible region.

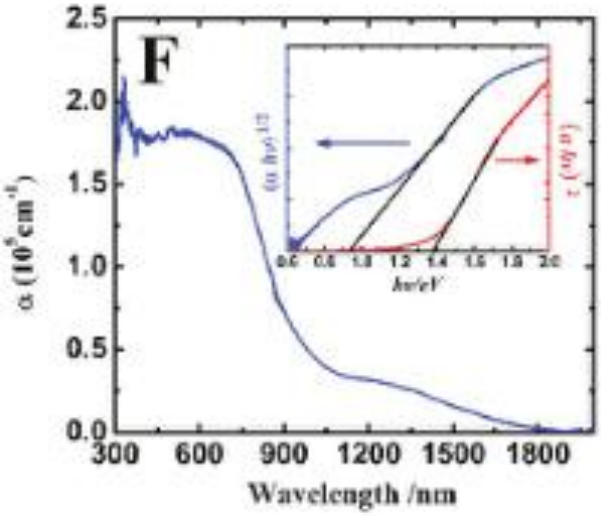

Figure 7: Absorption spectrum of iron pyrite and Tauc plots [17]

There were conflicting values of the work function of iron pyrite in the literature. Values of 3.3. 3.5 and 3.9 eV were found in [73], [74], while 5 eV was found in [75], [76]. Atomic force microscopy (AFM) of the samples in this report could not be measured to have an accurate value of the work function. This made it difficult to properly discuss electron transfer between the metal and the semiconductor in the last chapter as the cause of the decrease of photoluminescence. The iron pyrite carrier concentrations varied from 10^{15} range to 10^{18} range [45–48]. The high value of the second number could suggest plasmonic effects. The Seebeck of the single crystal found in nature varies from 200 to 300 $\mu V/K$ [81], [82]. The seebeck of the synthesized single crystal varied from -10 to -500 $\mu V/K$ [63], [83]. The seebeck coefficient for synthesized polycrystalline varied from 101 to 128 $\mu V/K$ [78]. Now that, the different characteristics of iron pyrite have been presented, the next part will discuss the different methods to synthesize the material.

Different synthesis methods

The different ways to synthesize iron pyrite are chemical vapor transport (CVT) [79] , chemical vapor deposition (CVD) [84], hot injection method [85], heat up method, spray pyrolysis [86] and hydrolysis [87]. The three methods that will be presented below are chemical vapor transport and two chemical synthesis method, heat-up and hot injection

Chemical vapor transport

Chemical vapor transport is a good technique to grow pure crystal of chalcogenide material [39–42]. The process happens in a quartz ampoule. The initial material are powders of the transitional material and the chalcogen material. They are loaded with stoichiometric ratios. A transport agent is also loaded into the quartz. In the case of iron pyrite, the transport agents are bromine[63], iodine[92], Mn[93], Cl[92], [94], and $FeBr_3$ [77]. The type of the semiconductor depends on the transport agent and the temperature gradient. Basically, the quartz containing the materials is introduced in a furnace. A temperature gradient is applied between the two ends of the quartz. The higher of the two temperatures is applied to the side with the starting material, usually the right part of the quartz. The powders undergo a sublimation process and become gases. The gases go from the higher to the lower temperature. Once the gases reach the colder region of the flask they react to form the crystal of the metal transitional chalcogenide. An example of the chemical equation for CVT grown iron pyrite is presented here

$FeS_2(s) + 2FeHal_3(g) \Leftrightarrow 3FeHal_2(g) + S_2(g)$ [92] where (g) is for the gas phase and (s) is for the solid phase. Hal represents the halogens (Cl, Br and I) that were used in the paper. The gas on the left goes from cold to hot and the gases in the right side go from hot to cold [63]**.**

Heat-up method

In this method all the different materials necessary for the synthesis are introduced in the flask from the start and the temperature is increased until nucleation temperature is reached [95]. If they are not all introduced from the start, the remaining materials are introduced at low temperature. In this method, there is first an accumulation of monomers due to the decomposition of the precursors. As the temperature increased, this supersaturation of monomers will induce a burst in nucleation. The burst considerably decreases the numbers of monomers and the rest of monomers will only participate in the growth of the already formed nuclei. In the case of iron pyrite, the burst happens at temperature lower than the nucleation temperature use in hot injection. To reduce the surface energy, the iron pyrite nanoparticles synthesized using heat-up method usually have a cubic shape [48–50]. The proposed model for the formation of different shapes of nanoparticles is presented in Figure 8.

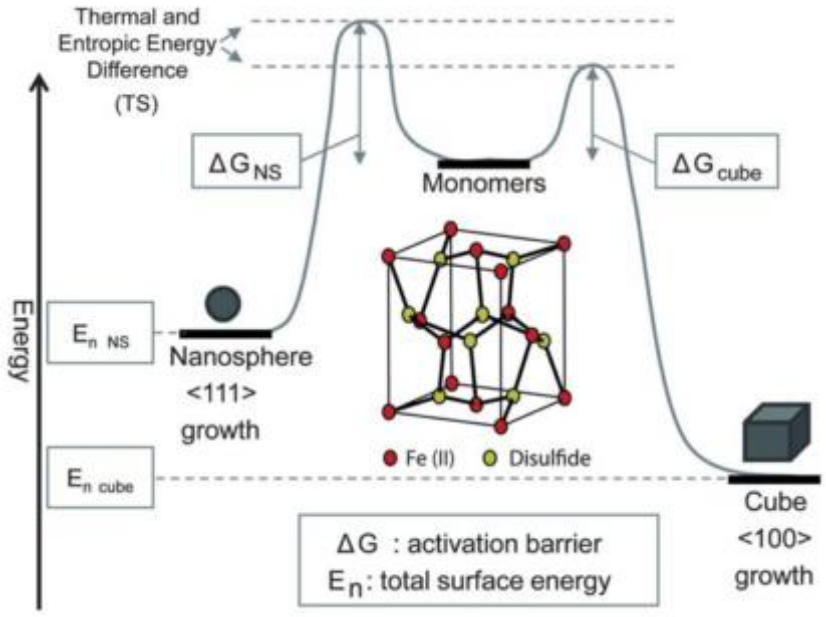

Figure 8: Model for the formation of two different shapes iron pyrite nanoparticles [97]

In a typical synthesis of iron pyrite using heat-up method, the iron precursor usually $FeCl_2$ or $FeCl_3$ is introduced in a three-neck flask containing an amine (octadecylamine, oleylamine, hexadecylamine). In a second flask, sulfur elemental is dissolved in a solvent, usually diphenyl ether. The two flasks are degassed to completely remove moisture. After that the sulfur content is injected into the iron flask and the temperature is raised.

Hot injection method

In the case of hot injection, unlike heat-up where all the reactants were heated together until the synthesis temperature was reached, some of the reactants are injected inside the flask when it reaches the synthesis temperature. Here the high supersaturation of monomers also induces a burst in nucleation [99]. The important decrease of monomers also limits further nucleation, making possible monodisperse nanoparticles synthesis [57–61]. The speed of introduction of the reactants can create multiple supersaturations and different nucleation regimes.

Date	Time	Chemicals	Temp.	Notes
06/14/13	*12:15*	$FeCl_2$-4 H_20:100 mg (1)	RT	
	12:15	HDA: 11.6 g	RT	
	12:17	Sulfur: 96 mg (2)	RT	
	12:18	Diphenyl Ether: 5 mL	RT	
	12:18	Solution (1)	RT	Set 70°C + Ar flow
	12:18	Solution (2)	RT	Set 70°C + vacuum
	1:00	Solution (1)	70°C	Set 120°C + vacuum. Completely melted, brownish solution
	2:40	Solution (1) and 2	120°C, 70°C	Ar flow
		Solution (1)	120°C	Set 220°C
	2:43	Solution (1)	220 °C	Add solution 2, solution turned black.
	5:43		220 °C	Stop heating. Cool down in a water bath
	5:45		90°C	3 mL of OA
	5:46		75°C	5 mL of Chloroform ($CHCl_3$)

Figure 9: Procedure of the synthesis FeS_2 nanoparticles, adapted from [85]

The regular hot injection method used to synthesize iron pyrite nanoparticles is presented in Figure 9. In a typical synthesis of iron pyrite using heat-up method, the iron precursor usually $FeCl_2$ or $FeCl_3$ is introduced in a three-neck flask containing an amine (octadecylamine, oleylamine, hexadecylamine). In a second flask sulfur elemental is dissolved in a solvent, usually diphenyl ether. The two flasks are degassed to completely remove moisture. After that the temperature of the Fe-amine complex is raised to the reaction temperature. The sulfur content is injected into the iron flask when the temperature is reached.

Problems with iron pyrite

Despite its high absorption coefficient, iron pyrite has not been able to achieve its full photovoltaic potential yet. The highest efficiency recorded for a cell made of iron pyrite is 2.8 % [105]. This is due to the different impurities that arise when synthesizing the material and later on when using it [106]. The low open voltage of the iron pyrite based solar cells is due to the many surface defect states, but also the fermi level pinning and its bandgap [75–77]. Although, the surface defects were first thought to be caused by the sulfur vacancies, one study shows that it might not be the case [109]. Ultimately the results of the surface defects is the creation of a metal-like shell for the semiconductor shell [106]. Therefore, finding a way to prevent these surface defects from happening is key to achieving decent iron pyrite solar cells efficiency. To do so, surface passivation has been done using TOPO [17] ligands at the surface of the nanoparticles. The lack of decomposition was due to the passivation of both sulfur and iron by TOPO. While the passivation was a success, with the nanoparticles not changing phase after one year of storage in air, TOPO is an expensive ligand and add extra cost.

The problem with pure iron pyrite for use in thermoelectric application is that despite the fact that its conductivity is high for photovoltaic, it is low when compared with the conductivity

of materials used in thermoelectric such as Bi_2Te_3, Bi_2Se_3 [110] and other chalcogenide material [68–71], [79–81]. Therefore, there is a need to increase the thermoelectric properties of iron pyrite. Doping using cobalt, arsenic and nickel was done to improve the electrical conductivity and the results are presented in Table 3**.** Doping with cobalt significantly increased the conductivity. The cobalt doping generates more charge carriers then the nickel doping because the two electrons from the nickel atom are involved in the creation of an orbital state. The state is near the middle of the bandgap and the electrons are not charge carriers. The only electron from the cobalt is directly injected into the conduction band. More energy is needed to bring the Ni electrons to the conduction band resulting in a lower conductivity compared with the cobalt doped [77].

	Resistivity	Carrier concentration	Hall mobility	Hall mobility
Co-doped	$0.009-0.02\Omega.cm$	$10^{18.7}-10^{19}$	$60-270cm^2v^{-1}s^{-1}$	
As-doped		$10^{14}-10^{18}$	$0.2-55cm^2v^{-1}s^{-1}$ (electrons)	$0.1-11.3cm^2v^{-1}s^{-1}$ (holes)
Ni-doped		$10^{15}-10^{16.6}$	$60-270cm^2v^{-1}s^{-1}$	
undoped	$15-85\Omega.cm$	$10^{15}-10^{16.6}$	$8-70cm^2v^{-1}s^{-1}$	

Table 3: Electrical characteristic of iron pyrite undoped and doped [77]

Learning from the result of this study, another study was performed [78]. In that study, the thermoelectric properties of iron pyrite and iron pyrite co-doped nanoparticles were investigated. The doping was done by mechanical alloying. The percentage of cobalt in the pyrite crystal varied from 0 to 5 %. The electrical conductivity increased with decreasing the size of the nanoparticles. It went from 0.02 $S.cm^{-1}$ for 70 nm particle to 3.1 $S.cm^{-1}$ for 16 nm particles. The seebeck coefficient decreased with decreasing the size of the particles from 128 $\mu V.K^{-1}$ to 101 $\mu V.K^{-1}$.

After doping the conductivity went from p-type to n-type and the thermal conductivity increased but not as much as the electrical conductivity for the 5 % sample. The ZT coefficient increased by a factor of 5 for cobalt doped pyrite. The ZT was $1.9*10^{-3}$ for 46 nm and for $3.8*10^{-3}$ for 16 nm and for $2*10^{-2}$ for 5 % cobalt. While there was a significant increase, it is still low compared to state of the art ZTs that are presented in Figure 10.

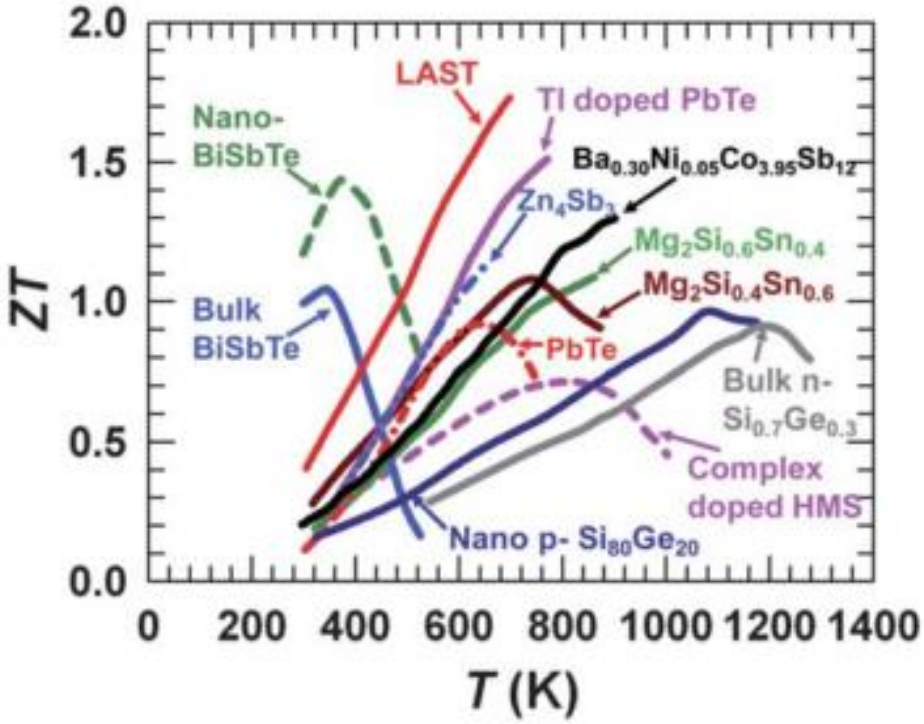

Figure 10: State of the art ZTs [35]

CHAPTER 3: EXPERIMENTAL TECHNIQUES, MATERIAL PREPARATION AND FABRICATION

3.1. Spectroscopy

3.1.1. Ultraviolet-Vis (Uv-Vis) spectroscopy

Ultraviolet-Vis spectroscopy, usually just called Uv-Vis allows you to determine the absorption, emission, and reflectance spectra of a material. Although, its name only mention visible and ultraviolet light, current Uv-Vis can go to the infrared region of the light spectrum. Absorption is probably one of the most important optical properties of a material and a semiconductor in particular, as in order to use light energy it must first be absorbed. Semiconductors like all materials just absorb a portion of the sun's spectrum, the range of wavelengths that they absorb represents their absorption spectrum. The absorption is often related to the refractive index of the material.

The refractive index of a semiconductor is complex and can be described by the Equation (12):

$$\dot{n} = n + ik \tag{12}$$

n, the real part of the refractive index of the material; it is directly related to its absorption.

k, the imaginary part of the refractive index; it is related to the extinction of the light. The reflectance, the amount of the light which is reflected back at the surface of the material compared to the incident light, can be expressed by the Fresnel formulae [113] presented in Equation (13):

$$R = \frac{(n-1)^2 + k^2}{(n+1)^2 + k^2} \tag{13}$$

3.1.2. Photoluminescence (PL) spectroscopy

As the excited state is not the normal state of the molecule, the behavior of the molecule is to return to the more stable state with the return of the electron to the ground state. The first step of this return is to go to the lowest energy level of the excited state. If the electron is already there nothing happens, but if not it must undergo vibrational relaxation, to go to a lower energy level. The electron must liberate its excess of energy in the form of thermal energy [114]. At the lowest energy level of S1, different things can happen. One such thing is radiative relaxation. Such radiative relaxation is called fluorescence. The electron returns to the ground state and releases its excess of energy in the form of a photon. It can be noticed here that the wavelength of the photon emitted due to the return of the electron will be different, because of the vibrational relations, than the one of the photon absorbed. The wavelength of a photon is related to the energy of this one through the formula below:

$$E = \frac{h*c}{\lambda} \tag{14}$$

E : energy of the photon (eV)

h : Planck's constant

c : speed of light in the free space

λ : wavelength of the photon (nm)

$h*c = 1240$ (15)

The electron could have undergone several vibration relaxations, the photon emitted and the photon absorbed don't have the same energy; therefore, they also have different wavelengths. The wavelength and the energy are indirectly related, when the energy decreases, the wavelength increases. The emitted photon will have a longer wavelength that the absorbed photon. The

absorption spectrum is shifted to longer wavelengths; this is the Stokes shift and it is presented in Figure 11 .

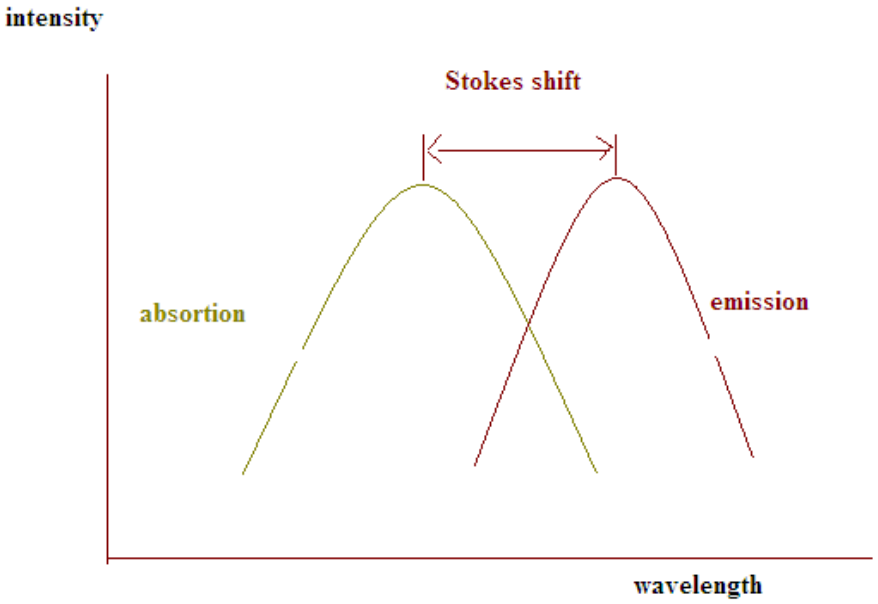

Figure 11: Representation of the Stokes shift

The electron can also go to the triplet excited state. It must undergo rotational conversion (Intersystem crossing; ISC) [114] as electrons in the single excited state do not have the same spin that the ones of the triplet state. After its conversion, it can relax to the ground state by either emitting light (phosphorescence) or not.

3.1.3. Raman Spectroscopy

Raman spectroscopy studies the inelastic scattering of light shining on a material. It is called inelastic because the emitted light does not have the same frequency than the incident light. There is either a red shift or a blue shift, this is called the raman effect. If a photon is absorbed by a material, some of the energy of the photon can be used to induce a raman mode in the material and the emitted photon will have a frequency lower than the incident photon. This new raman

frequency is the Stokes frequency. If a photon is absorbed by a raman active material, some of this energy can be transferred to the photon. The new photon will be emitted with a frequency higher than the frequency of the incident photon. This new raman frequency is the Anti-Stokes frequency. This can give information regarding the vibrational modes of the crystal of the material and can be used to identify a compound.

3.1.4. X-Ray Diffraction (XRD)

X-Ray diffraction takes advantages of the fact that an incident X-ray will interact with a material. If the material is a periodic structure in any kind, there will be constructive and destructive interference. The signal can then be detected and used to tell the crystalline structure of the material. This a very powerful technique.

3.1.5. Fourier Transform Infrared (FTIR) Spectroscopy

The technique takes advantage of the fact that organic molecules depending on their bonds absorb specific region of the infrared spectrum. The ability to detect these absorbed frequencies can then be used as a fingerprint for the molecule or the family of molecule like amines. In the case of the amine, there is a feature in their FTIR spectra between 2800 cm^{-1} and 3000 cm^{-1} that represents their carbon-hydrogen vibration modes.

3.2. Material synthesis and preparation

3.2.1. Synthesis using hot injection method

The synthesis of the FeS_2 nanoparticles was done using a simple hot injection method. First, two flasks were prepared. In the first flask, an iron precursor was dissolved in an amine

solution. For the iron precursor, Iron chloride ($FeCl_2$-$4H_2O$) was used and for the amine, hexadecylamine (HDA) and oleylamine (OLA) were used. In the second flask, elemental sulfur was dissolved in diphenyl ether. The molar ratio between Fe and S that works the best was found to be 6. The excess of the chalcogen material is common in chalcogenide material syntheses. It is also important here because the formation of FeS_2 is not a direct reaction. First, FeS is formed and as time goes, more and more sulfur is incorporated into the matrix to form the final molecule.

The first flask was put under argon atmosphere when using HDA, and the temperature was set to 70°C; once HDA completely dissolved, the flask was put under vacuum and the temperature was set to 120°C. If using OLA instead of HDA, there is no need to put argon atmosphere first, as it is a liquid and not a powder like HDA. Also, if there is no vacuum pump or if the vacuum is not good enough, the temperature should be set above 180°C to completely remove any moisture. The reaction is moisture sensitive, therefore the amount of moisture inside the flask should be minimized or removed completely. The second flask temperature was set to 70°C and it was put under vacuum. The two flasks were agitated during the entire process using two magnetic stirrers.

After complete dissolution of HDA, the color of the solution in the first flask was brownish and color of the solution of the second flask was yellow. The two solutions were put under vacuum for 1 hour to remove the moisture. Once the moisture was removed, both flasks were put under argon atmosphere. The first flask temperature was set to 220°C (the nucleation temperature of FeS_2). The content of the second flask was collected using a syringe and injected inside the first flask when its temperature reached 220°C. The injection step is a critical step to have monodispersed and pure FeS_2 nanoparticles. First, the injection should be fast (the applied pressure should not be too strong as to push the content of the flask outside). This helps to synthesize monodispersed nanoparticles. Second, the temperature of the solution after injection should not

fall below 200°C, or other phases could appear during the synthesis and not just the pyrite phase of FeS_2. To do that, the ratio of the first solution volume over the second solution volume should be over 3. It can be done by having a highly concentrated second solution. Also, the temperature of the first flask can be first set to a temperature higher than 220°C when switching between vacuum and argon. The temperature can then be set back to 220°C after the injection.

After injection of the sulfur precursor solution, the solution turned from brownish to black. The flask was then left under argon atmosphere for 3 hours. This reaction takes such a long time due to the absence of direct FeS_2 reaction as mentioned earlier. At the end of the synthesis, the hot plate was turned off and the solution was cooled down using a water bath. At 90°C, oleic acid solution was added to replace the loosely attached amine ligands. This latter step also makes it easier to clean. At 75°C chloroform (CH_3Cl) was added to stop the reaction. This step was then followed by a purification step. For the first step of the purification, the solution of the nanoparticles was put in a centrifuge to separate the nanoparticles from the solvent and the organic impurities. The speed was set to 4000 rpm for a duration of 2 minutes. The nanoparticles precipitated. The solvent was discarded and more chloroform was added. The same step was repeated and the nanoparticles precipitated again. Ethanol was then added and the centrifugation speed was changed from 4000 to 8000 rpm. The nanoparticles precipitated again and ethanol was discarded and the particles were dispersed in chloroform and stored for characterization purpose. After the synthesis, the nanoparticles were characterized to make sure that the synthesized material was FeS_2 nanoparticles of pyrite phase.

3.2.2. Ligand Exchange

When synthesizing nanoparticles using chemical method, ligands are usually used. They served different purposes. They are used to control the dimension and or the morphology of the

nanoparticles during the synthesis. For example, for the same material one ligand can be used to synthesize cubic shape nanoparticles and different one will be needed for spherical nanoparticles. They basically work by attaching themselves to a particular area of the nanoparticle surfaces as they grow. Depending on the area where they are attached, they will favor growth in one or more directions. Ligands also play a role, in the solubility of the nanoparticles. Depending on what ligands is attached at their surfaces, the nanoparticles will be soluble in a particular solvent or not. In the case reported here, the ligands anchored at the surface of the nanoparticles are HDA or OLA. They were needed for the synthesis but for application, they are not helpful as they do not prevent oxidation of the particles and the films. Furthermore, they are poor conductors, which is not good for solar cell and other optoelectronic applications. It was therefore decided to replace the native ligands by shorter and more conductive ligands. The ligands of choice were inorganic Fe, Sb and $(NH_4)_2S$. The first two were chosen because they have already been used as ligands in other chalcogenide materials; the last one was chosen hoping that it would have the same effect that Cd has, when used as a ligand to improve the efficiency of CdTe solar cells.

The method used for the ligand exchange/displacement was a simple biphase process. The precursor of the ligands was dissolved in formamide. Iron chloride was used as the precursor for Fe, antimony chloride was used as the precursor for Sb and ammonium sulfide was used as precursor for the last ligand. A 0.1 M of the new ligands in formamide solution was mixed with a 10g/L solution of the nanoparticle dissolved in chloroform in a 1:2 ratio. Chloroform being denser that formamide, the nanoparticles solution precipitated to the bottom of the tube, with the formamide solution staying on top. The mixed solution was then agitated, and this agitation induced a displacement of the ligand at the surface of the nanoparticles. This nanoscopic phenomenon could be observed at the macro scale as the nanoparticles move from the chloroform

phase still at the bottom of the tube to the formamide phase. The Figure 12 presents the different steps of biphase ligand exchange. First, the nanoparticles are in the bottom of the flask in the chloroform phase. Second, after agitation the nanoparticle moved to the formamide phase. A syringe was used to extract and discard chloroform from the bottom of the tube. More chloroform was added and the process was repeated multiple times (at least 3 times), to ensure complete transfer. After this process, acetone was added to the nanoparticles in formamide solution to start the purification process. Multiple purification steps were required and during some of these steps, few drops of the new ligand precursor in formamide were added. At the end of the purification process, the nanoparticles were dispersed in either ethanol or dimethylformamide (DMF) for later use.

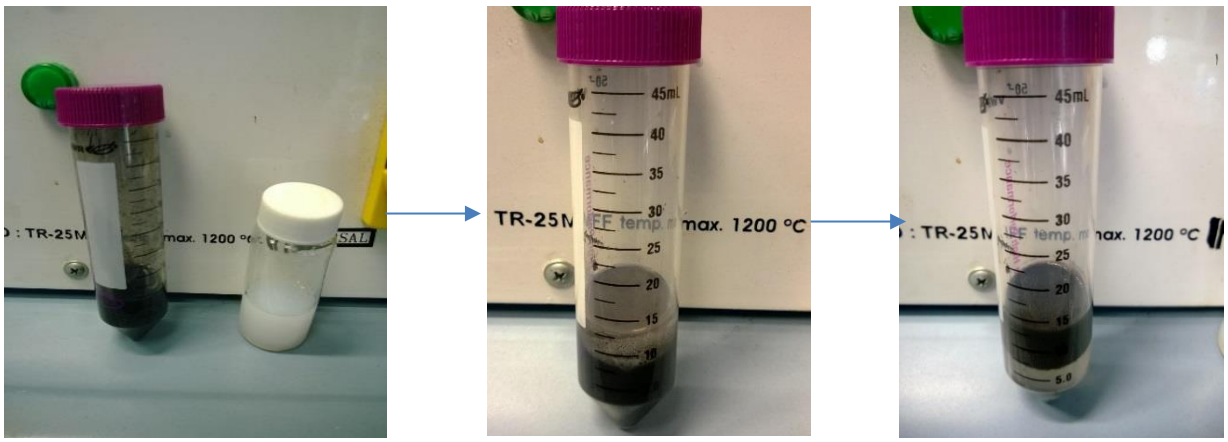

Figure 12: Presentation of the biphase ligand exchange process

3.3. Deposition techniques

3.3.1. Spray pyrolysis

Spray pyrolysis is a technique that consists in depositing material dissolved in a solvent at a temperature close to the boiling temperature of the solvent. When solution based film dried; the solvent leaves the film by creating cracks. These cracks are detrimental for the performance of the films in applications. To overcome the formation of the cracks after solvent evaporation, post

processing of the films is needed. In the spray pyrolysis case, no need to try to overcome the cracks, as it is possible to have a crack free film with this technique. With the temperature of the substrate, where the film is to be deposited at, close to the boiling temperature of the solvent, this latter evaporates; therefore, only the material reaches the surface. This results in crack free films. An automated pulsed spray pyrolysis setup was used for this. The system employs a nozzle, where nitrogen is used as the carrier gas. The system is controlled by an electronic valve. The thickness of the film can be controlled by the concentration of the material, the duration of the pulse, the time between each pulse, the temperature of the substrate and the number of pulses. In this report, the pulse duration will be 0.5 seconds and the duration between pulses will be 30 seconds unless otherwise mentioned. Spray pyrolysis was used to make the iron pyrite films.

3.3.2. Spin coating

Spin coating is another deposition technique that uses centrifugal force to deposit a material on a substrate. The solubility of the material in the solvent is critical in this method. A low solubility does not allow for high spin speed as material do not stick to the surface; however low spin speeds do not create uniform films. One way to overcome that is to start with low speed spins to have some material on the surface. The low speeds are then followed by step of high speed spin once there is enough material on the surface. The material is more likely to stick if there is already some of it on the surface. Even though this technique is intensively used in lab because of its ease of use, it is difficult to use it for mass production. It is a wasteful method as most of the material does not stay on the surface but it is thrown away. It is impossible to spin large area. The system was used to deposit iron pyrite onto FTO and ITO substrate for micro raman and micro PL measurements.

CHAPTER 4: STABILIZATION OF NANOPARTICLES

Once the synthesis is done, different characterizations are needed to make sure that it was in fact the proper material that was synthesized. Different characterization techniques were done: XRD, SEM, TEM, absorption, PL and Raman spectroscopy.

4.1. Characterization of FeS_2 nanoparticles

4.1.1 XRD

The X-Ray diffraction of the FeS_2 nanoparticles was measured to make sure that they had the pyrite phase. The XRD is presented in Figure 13.

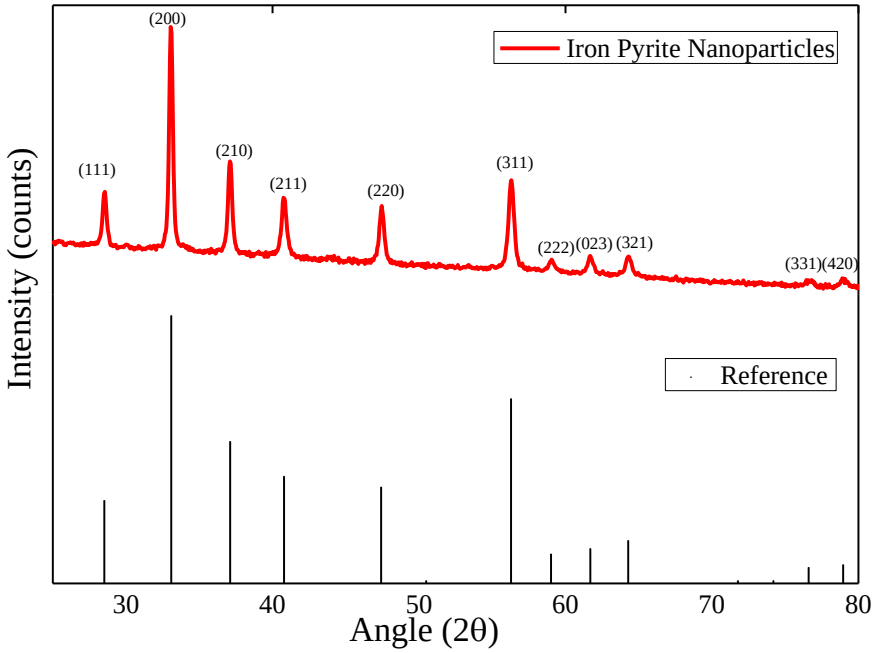

Figure 13: XRD Spectrum of FeS_2 nanoparticles

The XRD results are compared to the XRD of FeS_2 pyrite phase. The results- are similar to the reference number JCPD 024-0076 with the peaks at 28.5, 33, 37, 40, 47, 56, 59, 61, 64, 76 and 78 representing respectively the (111), (200), (210), (211), (220), (311), (220), (023), (321), (331), (420) orientations. The XRD is a first proof that the synthesized nanoparticles were pure

pyrite phase FeS_2. Using the Scherrer formula from Equation (15), the average size of the nanoparticles was approximated to be 20.46 nm.

$D = \frac{K\lambda}{\beta \cos\theta}$ (16). K, λ, β and θ are respectively, the shape factor, the X-ray wavelength, The FWHM and the Bragg angle. The peak used for the calculation was the peak at 33.08. The K used was 0.9. $\lambda(Cu) = 1.5404\text{Å}$.

4.1.2 TEM

The TEM of the nanoparticles is presented in Figure 14. It shows that the particles have random shapes and sizes. The particles from the TEM image were not monodispersed.

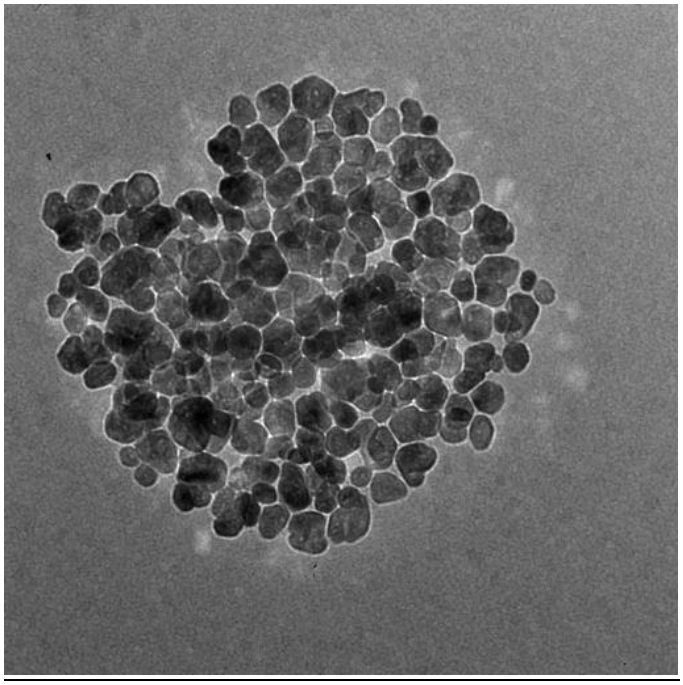

Figure 14: TEM image of FeS_2 nanoparticles after synthesis

4.1.3 Raman spectroscopy

The nanoparticles were also characterized using raman spectroscopy. The Figure 15 presents the raman spectrum of the nanoparticles. The laser used was a red laser at 632 nm. The raman spectrum is similar to raman spectrum of pure iron pyrite. The three main peaks at 343, 380 and 430 cm^{-1} are present. The highest peak at 380 is the A_g mode; the two sulfur atoms of the dumbbell pair perform stretching on the dumbbell planes and this movement is in phase throughout the iron pyrite crystal. The second highest at 343 is the E_g mode; the two sulfur atoms move in a direction perpendicular to the dumbbell plane. The phonons are said to be in libration. The last peak at 430 is the T_g mode. It is a combination of different librations and stretchings. This last mode is triply degenerate. The other two peaks of the T_g are difficult to measure with the equipment and are at 350 and 377 cm^{-1}.

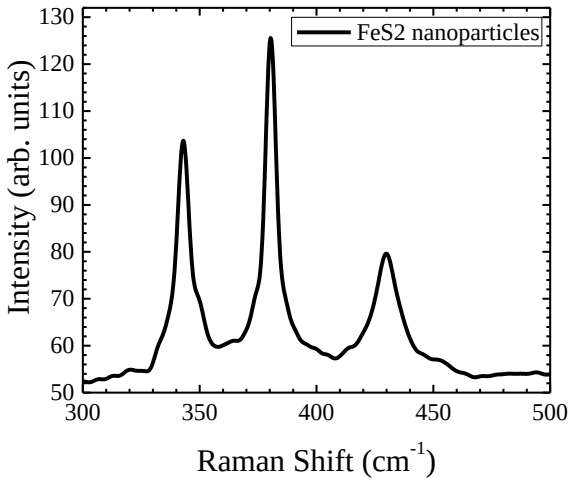

Figure 15: Raman spectrum FeS_2 nanoparticles

4.1.4 Absorption

The nanoparticles were characterized using Uv-Vis spectroscopy and the results are presented in Figure 16. The absorption spectrum was used to extrapolate the bandgap and the bandgap was found to be around 1 eV which is close to the theoretical value of the bandgap of iron

pyrite. Using finite difference frequency domain (FDFD), the absorption coefficient was simulated. The absorption coefficient was calculated by finding the transmission of two different iron pyrite thin films and using the formula from Equation (17), $\ln\frac{T_2}{T_1} = \alpha(T_2 - T_1)$ (17). T_1 and T_2 are the transmissions of the first and second thin films and α is the absorption coefficient. The absorption coefficient was used to make the Tauc plots in order to calculate the indirect and the direct band gaps. Using $(\alpha.h\nu)^{1/2}$ for indirect bandgap and $(\alpha.h\nu)^{2}$ for direct. The Tauc plot confirmed the indirect bandgap around 1 eV. Two directs bandgap were found, one at 1.7 eV and a second one around 2.51 eV. The simulated absorption coefficient and the Tauc plots are presented in Figure 17. As expected, the absorption coefficient in the visible region in the order of 10^5.

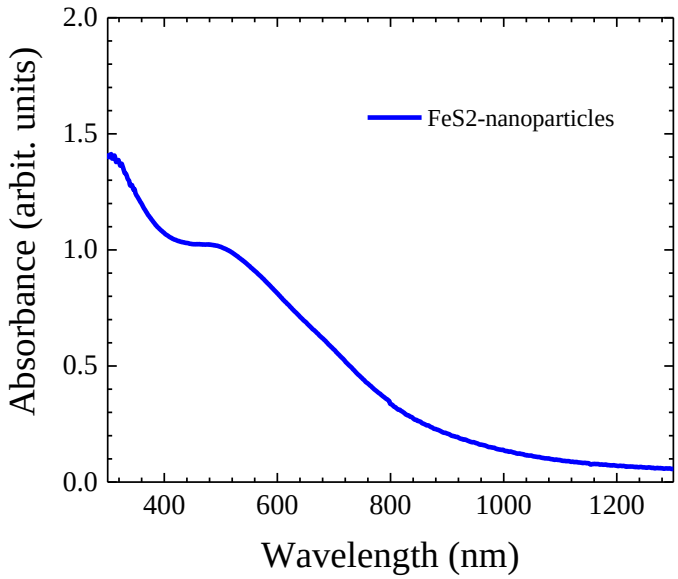

Figure 16: Absorption spectrum of FeS_2 nanoparticles

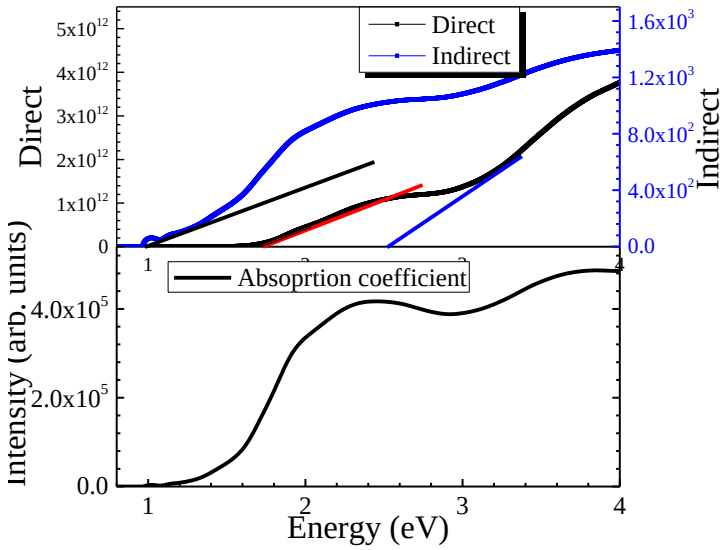

Figure 17: Absorption coefficient of FeS_2 simulated using finite difference frequency domain and Tauc plots

4.1.5 Photoluminescence

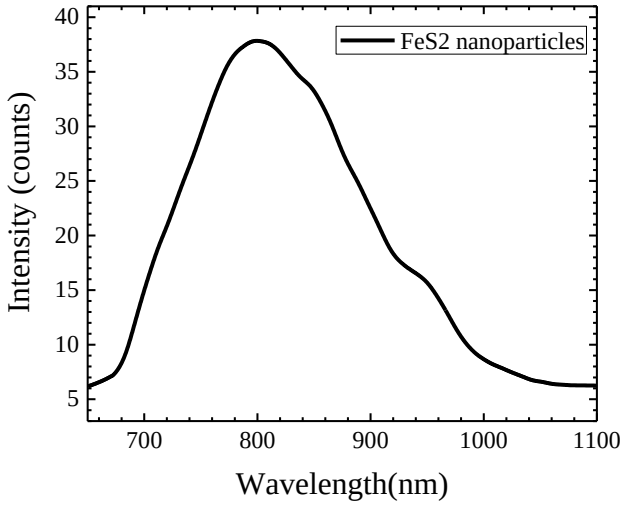

Figure 18: PL spectrum of FeS_2 nanoparticles

The nanoparticles were characterized using PL spectroscopy and the results are presented in Figure 18. The PL spectrum shows the PL peak around 800 nm or around 1.6 eV, which is close to the first direct bandgap of the iron pyrite that was measured using the Tauc plot.

After the different characterizations ensure the growth of pure iron pyrite nanoparticles, the next step is to improve the stability of the nanoparticles and the iron pyrite films. To do so, the long organic amine ligands were replaced by shorter inorganic ligands. The results are presented in the next part of this chapter.

4.2. Ligand Exchange

4.2.1. Ligand exchange characterization

The ligand exchange was observed during the transfer of the nanoparticles from the chloroform to the formamide phase but some experiments are still necessary to confirm that there was in fact displacement of ligands at the surface of the nanoparticles. One such experiment is Fourier transform infrared (FTIR) spectroscopy.

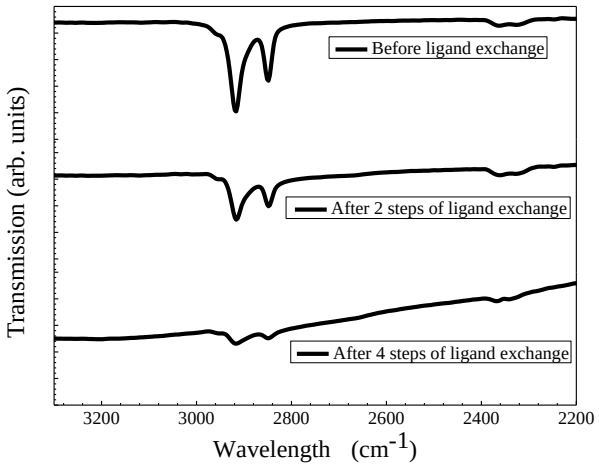

Figure 19: FTIR of FeS_2 nanoparticles before and after several step of ligand exchange

The technique takes advantage of the fact that organic molecules depending of their bonds absorb specific region of the infrared spectrum. The ability to detect these absorbed frequencies can then be used as a fingerprint for the molecule or the family of molecules, like amines. In the

case of the amine, there is a feature in their FTIR spectra between 2800 cm^{-1} and 3000 cm^{-1} that represents their carbon-hydrogen vibrations mode.

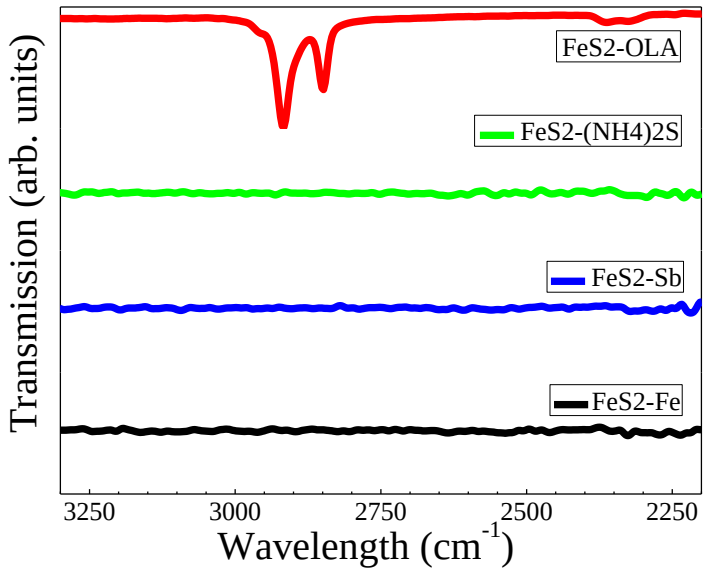

Figure 20: FTIR spectra of FeS_2 nanoparticles before and after ligand displacement

The FTIR showed that the carbon-hydrogen vibration mode is present before ligand displacement and completely disappears after the exchange. This is a good indication that the procedure was a success. The absence of signature at another place also showed that the new ligands were not organic, which was the case in the experiment. The FTIR spectra of the particles before and after ligand exchange are presented in Figure 20. The Figure 19 shows the FTIR spectra of the nanoparticles at different steps of the ligand exchange. As expected, the molecular vibrational signature of the amine disappears after complete ligand exchange.

When it is confirmed that the exchange was a success, it is critical to make sure that the process did not change the phase of the nanoparticles and that they remain pyrite. The same techniques that were used to characterize the nanoparticles after synthesis were once again used to

compare the material before and after the ligand exchange. Uv-Vis of the nanoparticle before and after ligand exchange was measured and the results are presented Figure 21.

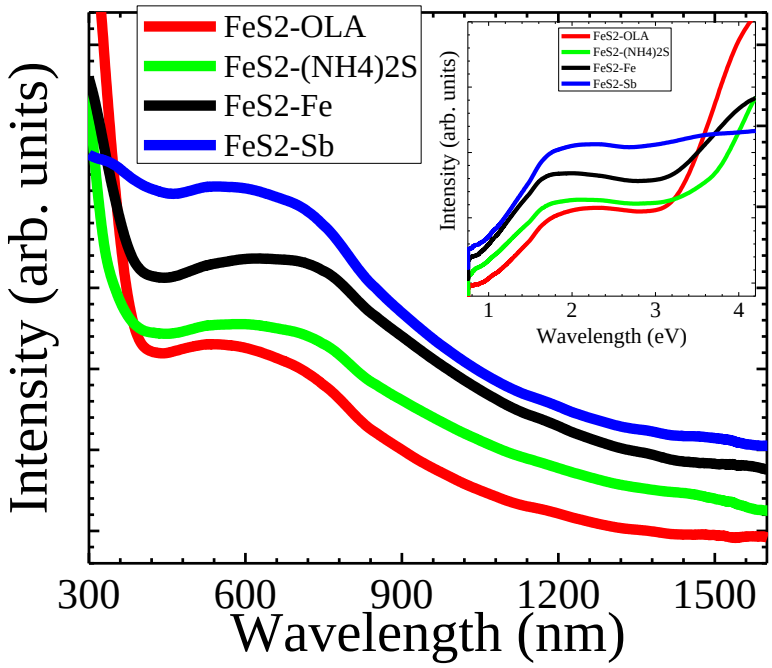

Figure 21: Absorption spectra of FeS_2 nanoparticles before and after ligand exchange

The spectra are quite similar, there are just small differences. The small shift in the optical absorption is due to the change of the dielectric constant at the surface of the particle by another anchor group. The approximated band gap varies between 0.85 – 0.9 eV depends on the ligands used. This is due to fact that each ligand injects different number of carriers inside the iron pyrite. These injected carriers are sufficient to vary the bandgap, or it could be just be experimental error. The second difference is the absorption at high energy photon. The absorption spectra rise fast for 3 of the ligands, amines, Fe and $(NH_4)_2S$, but remains steady for the Sb ligands. The reason of this behavior remains unclear.

The XRD of the nanoparticles before and after ligand exchange was measured and the results are shown in Figure 22. The results are also similar, the only noticeable difference is the ratio of the peaks at the 311 and 210. Only for the $(NH_4)_2S$ is this ratio higher than 1. The ratios are respectively 0.88, 0.83, 1.34 and 0.91 for the nanoparticles with OLA, Sb, $(NH_4)_2S$ and Fe as ligands.

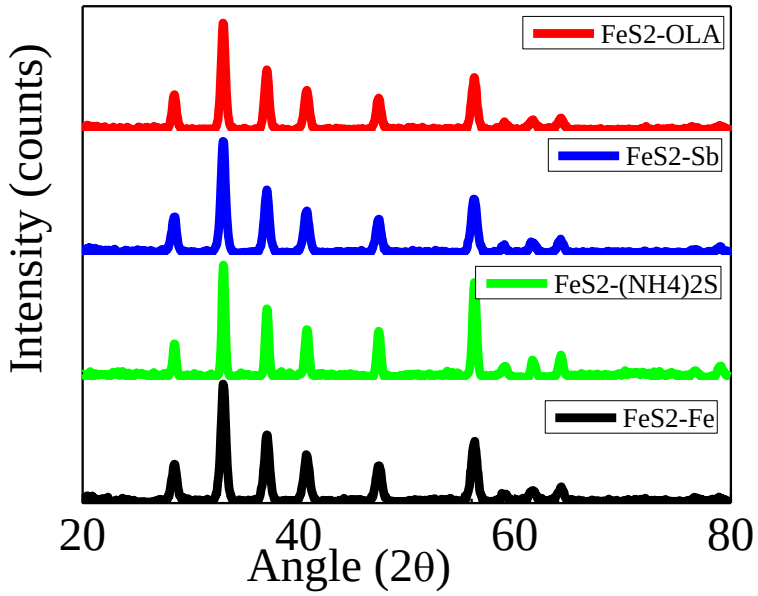

Figure 22: XRD spectra of FeS_2 nanoparticles before and after ligand displacement

The PL of the different nanoparticles after ligand exchange was measured and the results are presented in Figure 23. The PL is quenched after ligand exchange. This is because the other ligand introduced states inside the bandgap that act as traps reducing the number of radiative decays to the valence band from the conduction band. Another consequence of the traps is the shift of the PL peaks. The peak position is respectively at 800, 774, 770 and 840 nm for the nanoparticles with OLA, $(NH_4)_2S$, Sb and Fe as ligands. The full width at half max was also increased after ligand exchange as many traps were probably introduced. This would be bad if the nanoparticles were used for an emission device such as LED but it might not have a detrimental effect on solar

cells or photodetectors. Even though the traps could increase the dark current of the nanoparticles, and this later effect could reduce the efficiency of the solar cells or photodetectors.

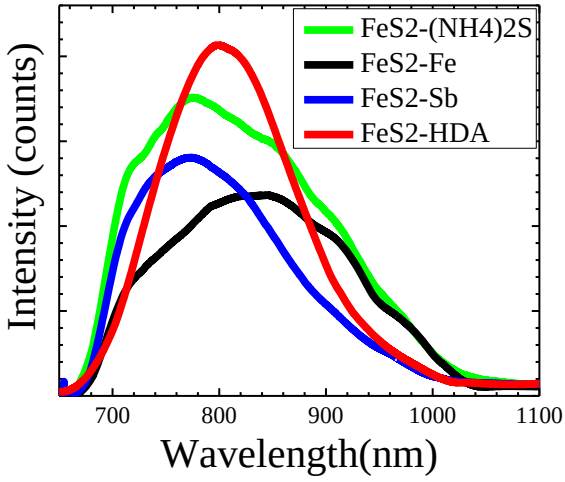

Figure 23: PL spectra of FeS_2 nanoparticles before and after ligand exchange

4.3. Stability investigation

As previously mentioned, one of the major problem with iron pyrite, as nanoparticles or films is stability. Iron pyrite tends to oxidize when it is exposed to air; the film and the nanoparticle therefore need to be stored in an oxygen free environment. Iron pyrite also loses sulfur at temperatures even a little higher than room temperature. It was for this reason that the effects of the ligands on the stability of the films and the nanoparticle was studied. Two things will be investigated here. The possibility of FeS_2 to remain pyrite when deposited at high temperature and its air stability. To investigate the air stability, the nanoparticles and the films were stored for 1 year in air. The films and the particles were characterized before and after the 1 year.

4.3.1. Film deposition film and high temperature stability

To study the benefit ligands, it was decided to deposit them at high temperature. Then, the thing to consider was what type of solution deposition technique to use and what solvent would be the most appropriate for the deposition? The choice of the deposition went for the pulsed spray pyrolysis technique and the solvent of choice was dimethylformamide (DMF). The technique was not only used because it allows to deposit at high temperature but also because it can make crack-free films. Formamide was used because of its boiling point (around 153°C) despite the fact that it is toxic, the deposition happened in a fume hood. It was later found that DMF dissolves sulfur from the nanoparticles and was therefore not good for air stability.

Spray pyrolysis consists on making films by depositing a solution containing the nanoparticles onto a substrate that is in contact with a hot surface (the temperature of the substrate, should be close to the boiling point temperature of the solvent for optimum results). The principle is to have the solvent evaporates before reaching the substrate. This allows deposition of films that are cracks free, as cracks usually appear when the film dries up and the solvent evaporates. The substrates that were used were 800 nm thick molybdenum films that were deposited by DC sputtering on 2 mm soda lime glass. 300°C, 250°C and 200°C were used at the deposition temperatures for the spray system. When the spray temperature was set to 300°C, the temperature at the surface of the substrate was around 200°C and when the spray temperature was set to 200°C, the temperature at the surface of the substrate was around 145°C. Each pulse lasted half a second and 30 seconds to 1 minute were allowed between each pulse for temperature recovery and 60 cycles were needed. The concentration of the solutions used was set to 5 g/L. To make sure that the concentration was always the same, the nanoparticles were dried under vacuum after their synthesis or the ligand exchange. The dried samples were then crushed to make a powder and the

powder was weighed and put in DMF for the deposition. When using 5 g/L as the concentration, films with thicknesses of around 2 microns were obtained when using 200˚C and films with thicknesses of around 1.5 micron were obtained when using 300˚C.

After deposition, the films were characterized using EDX and it was found that they were still FeS_2 and did not lose sulfur for the films after ligand exchange. The Figure 24 shows the SEM of a film after deposition and the EDX of this film. The EDX shows that the film did not lose sulfur as the sulfur-to-iron ratio is around 2. If nanoparticles with incomplete or no ligand exchange were used to make films, these films were sulfur deficient. The EDX of films made with incomplete ligand exchange is shown in Figure 25.

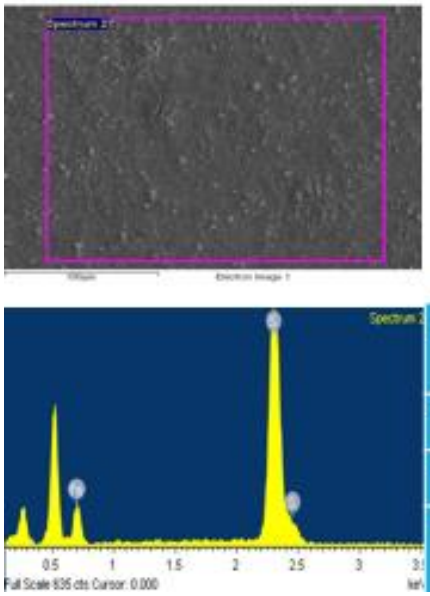

Element	Weight%	Atomic%
S K	53.47	66.68
Fe K	46.53	33.32
Totals	100.00	100.00

Figure 24: SEM image of the FeS_2 thin film and its EDX measurements

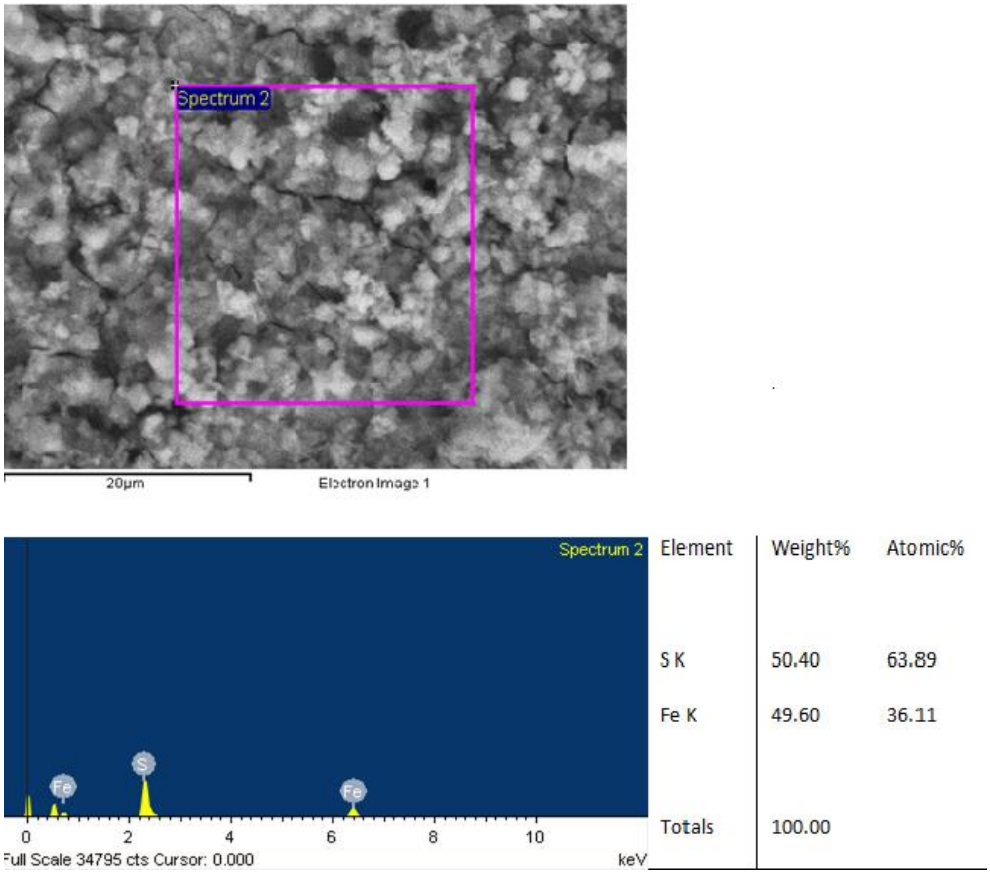

Figure 25: SEM image of the FeS_2 – amine thin film and its EDX measurements

The pyrite phase of the films was later confirmed by doing XRD. The films with Fe, Sb and $(NH_4)_2S$ ligands did not change phase, but films with amine ligands remaining did not conserve their phase. The XRD of the films with Fe, Sb and $(NH_4)_2S$ ligands deposited at 300˚C, with the XRD of Mo are presented in Figure 26. With DMF attacking the nanoparticles depriving them of sulfur rather quickly (from hours to a day depends of the ligands), the films were deposited right after the ligand exchange and the dispersion in DMF. If the nanoparticles were allowed to stay in DMF after a day, the films did have phase change.

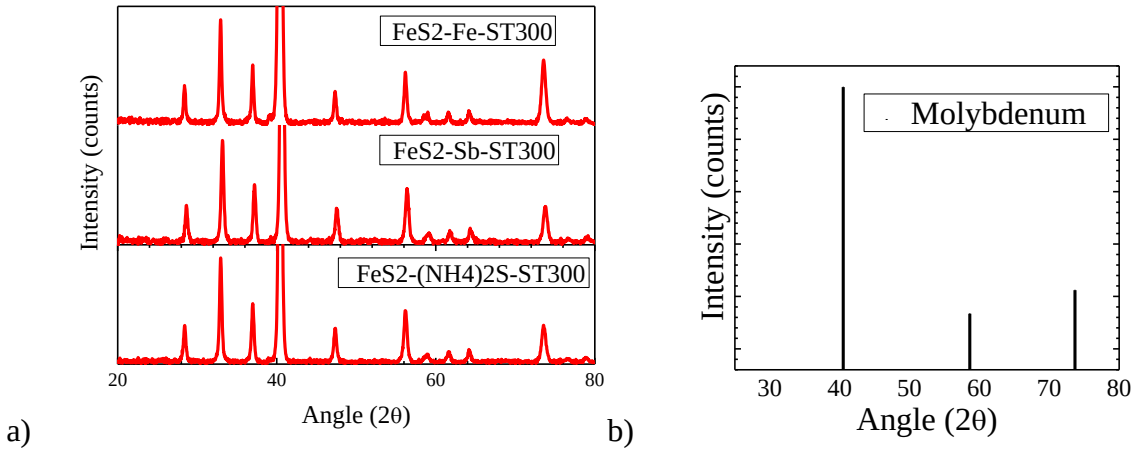

Figure 26: XRD of a) the FeS_2 films and the b) molybdenum reference

The effect of DMF on the nanoparticles was investigated by measuring the XRD of nanoparticles after being stored for 1 week in DMF. The nanoparticles were then used to make films. The films were annealed after in a sulfur atmosphere under argon. The films before and after the annealing were also characterized using XRD. The results of the XRD of the nanoparticles after being stored in DMF for one week are presented in Figure 28. It shows that after two weeks in DMF, only the nanoparticles with $(NH_4)_2S$ ligands remain somehow pyrite when the rest completely lose their phase. The ammonia ligand are more strongly attached to the nanoparticles than the other ligands. The Figure 27 presents the results of the XRD of the films before and after annealing in sulfur atmosphere at 475˚C for 1 hour. The films were deposited at 250 ˚C. The films right after the deposition are not pyrite anymore. Only the FeS_2-$(NH_4)_2S$ films have some pyrite peak but they also have some extra peak not belonging to pyrite. This agrees with the fact that the bond between the ammonium ligand and nanoparticles is the strongest. The films that were made with iron pyrites nanoparticles with ligands different than ammonium sulfide do not have any of the pyrite peaks anymore, just different peaks. These peaks are probably a mix of different sulfur

to iron ratio peaks and peaks due to oxidization of the films. After sulfurization, the FeS_2-$(NH_4)_2S$, and FeS_2-Fe films recovered their pyrite phase but the FeS_2-Sb film did not recover their phase.

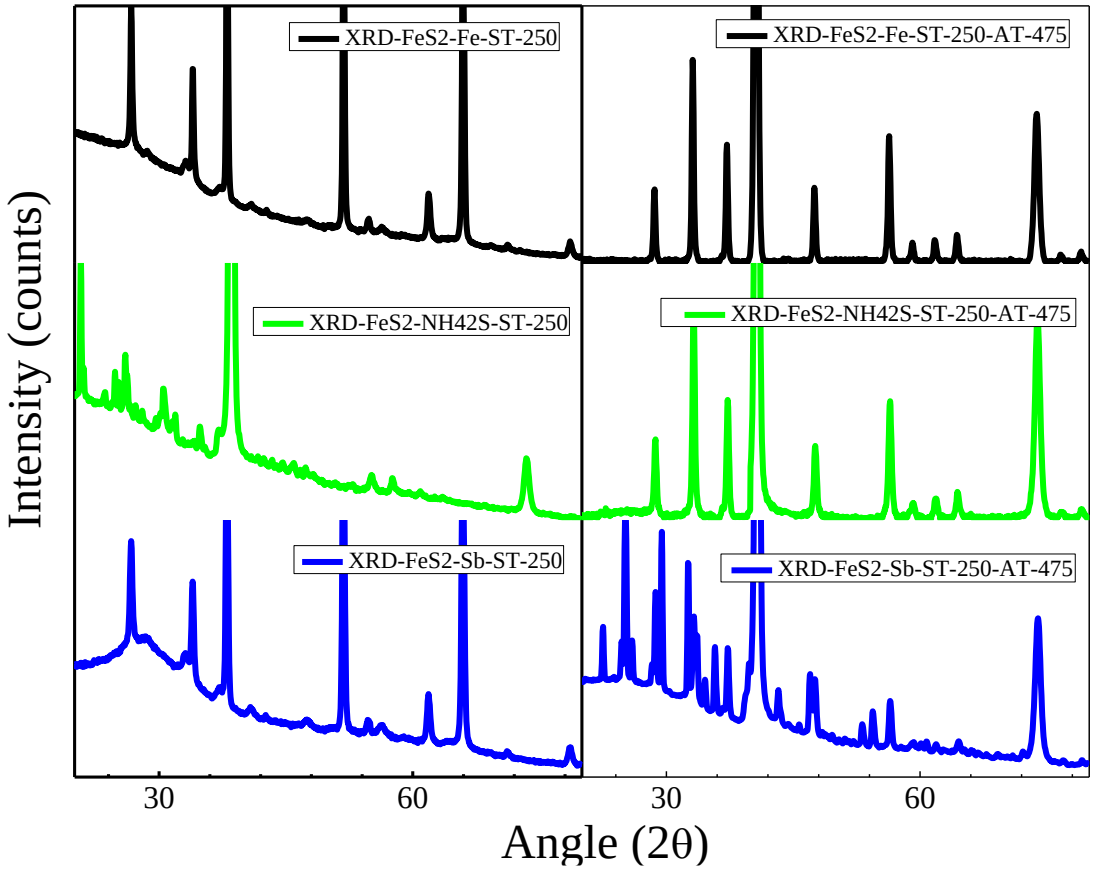

Figure 27: XRD spectra of FeS_2 film deposited using spray pyrolysis using nanoparticles with different stored in DMF for 1 week, before and after annealing at 475˚C

4.3.2. Air Stability

The second stability that was studied was the air stability. As it was already mentioned, DMF dissolved the ligand and accelerated the desulfurization of the iron pyrite nanoparticles. Even after a few days most nanoparticles did not exhibit any recognizable phase as it can be shown in Figure 28. The most robust ligand was $(NH_4)_2S$, which took a little bit over two weeks to

completely lose any trace of the pyrite phase. Fe ligands were second as it took them a little bit under a week to lose the cubic phase. The worst ligand was Sb, which took a few hours to degrade.

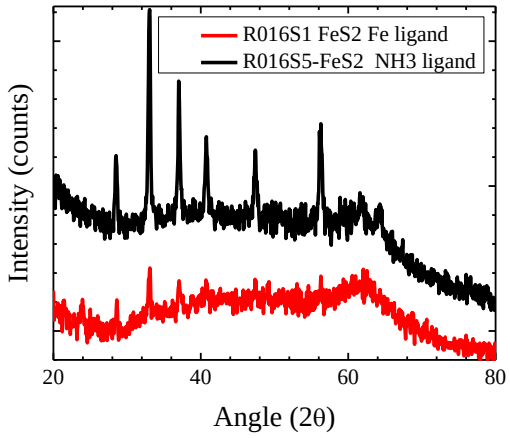

Figure 28: XRD spectra of FeS_2 nanoparticles with different ligand after one week in DMF

The stability of the films and nanoparticle was investigated by measuring raman of the film after being stored in air for one year. Raman was used for this particular investigation, because raman spectroscopy is more sensitive to phase change in iron pyrite than XRD. The films remain pyrite even after being exposed to air at room temperature for one year. The film did not lose sulfur as is the tendency for iron pyrite. The raman spectra of the nanoparticles after one year of being stored in air is presented in Figure 29. The raman does not show any sign of phase change. There is even the presence of the second Tg mode at 350 cm^{-1} in the spectra of the particles with $(NH_4)_2S$ and Sb as ligands. The third Tg mode at 377 because of its proximity to the Ag mode is overshadowed by it. The peaks are not exactly at the same position for the different ligands. For example, the 380 peak, at 380.34, 380.65 and 381.3 cm^{-1} for $(NH_4)_2S$, Fe and Sb ligands. The raman spectra of films being stored for one year in air are presented in Figure 30. The raman of the films shows that they remain pyrite after the storage.

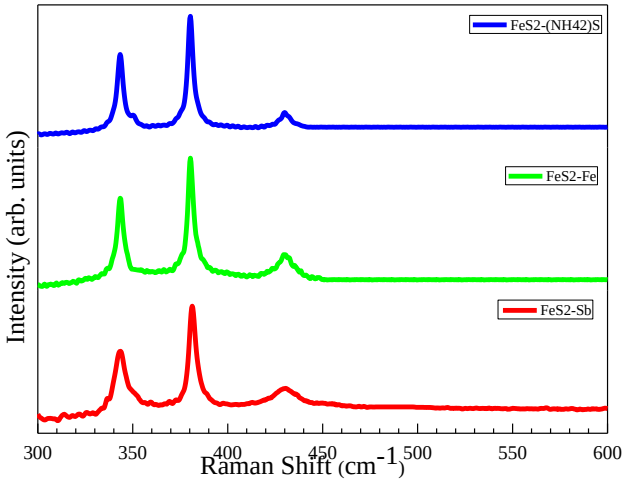

Figure 29: Raman spectra of FeS_2 nanoparticles after ligand exchange

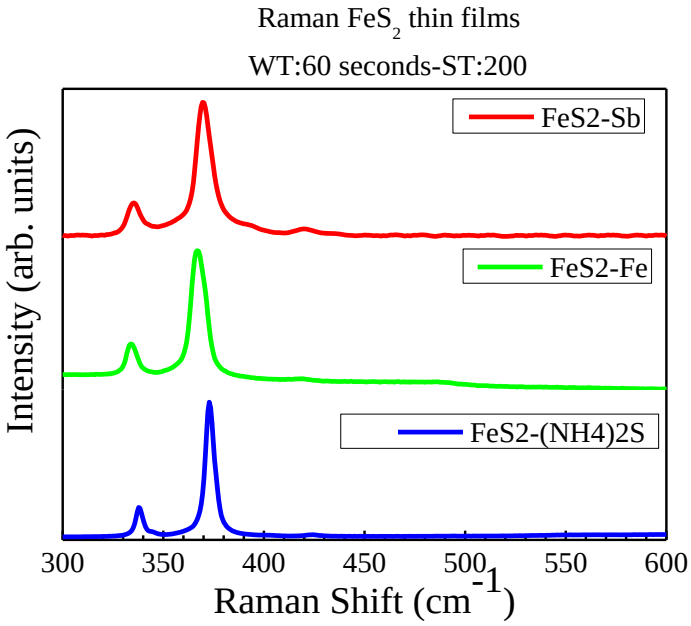

Figure 30: Raman spectra of FeS_2 thin film with ligand exchange after one year in air

4.4. Crystallization study

The effect of the ligands on the crystallinity of the films was also investigated. The films were deposited at 200˚C. The films were then annealed at 475˚C and 525˚C and Cross section images of the films were obtained for each annealing temperature using SEM and the results are presented in Figure 31. From the picture, it shows that there is a small crystallization after the deposition for the Fe ligands. The films from the $(NH_4)_2S$ are also showing a little bit of crystallization, while the films with Sb ligands completely broke apart. At 475˚C, the crystallization of the film with $(NH_4)_2S$ and Fe start to deteriorate and further deteriorate when the annealing temperature was increased. In order to investigate this counterintuitive observation, EDX of the film was performed. It was noticed the presence of traces of sodium in the films. Sodium from the soda lime must have migrated into the film and while, it helps for the crystallization of other chalcogenide materials. It does not seem to be have the same effect in iron pyrite.

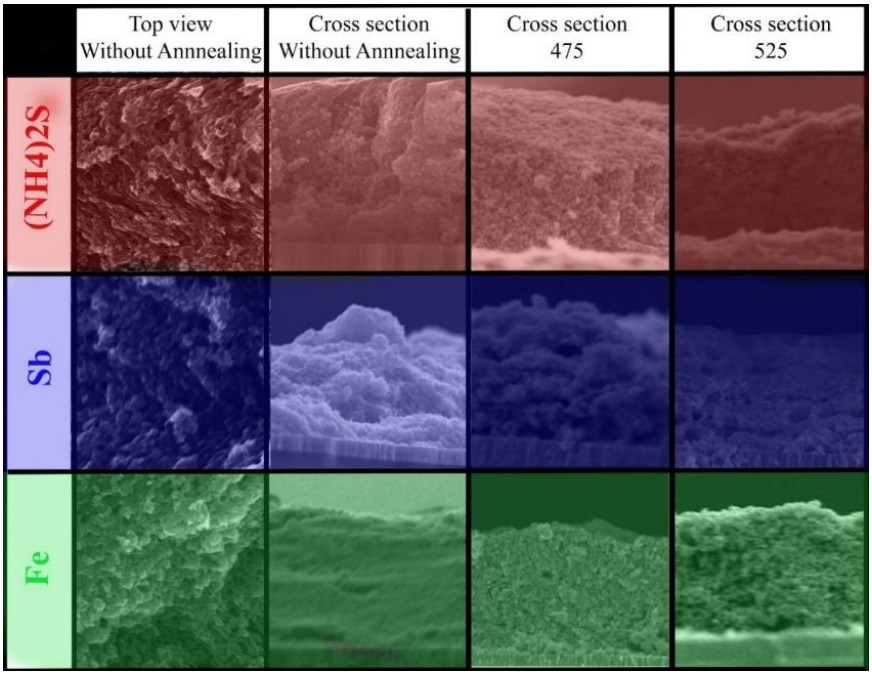

Figure 31: Crystallization study of the different ligands

Solar cells were fabricated by depositing cadmium sulfide as the window layer using chemical bath deposition and depositing zinc oxide and aluminum doped ZnO oxide as the front contact using sputtering. The solar cells did not exhibit any photovoltaic effects. This was due to the high conductivity of the iron pyrite films.

Iron pyrite nanoparticles were successfully synthesized using a hot injection method. The nanoparticles were characterized to confirm the pyrite phase. The ligands at the surface of the particles were replaced to improve the air and temperature stabilities of iron pyrite. The problem is that the ligands also introduced states inside the bandgap of the materials. These states were ultimately detrimental for the iron pyrite solar cells. In the next part of this report, these effects will be put to good use.

CHAPTER 5: THERMOELECTRIC PROPERTIES

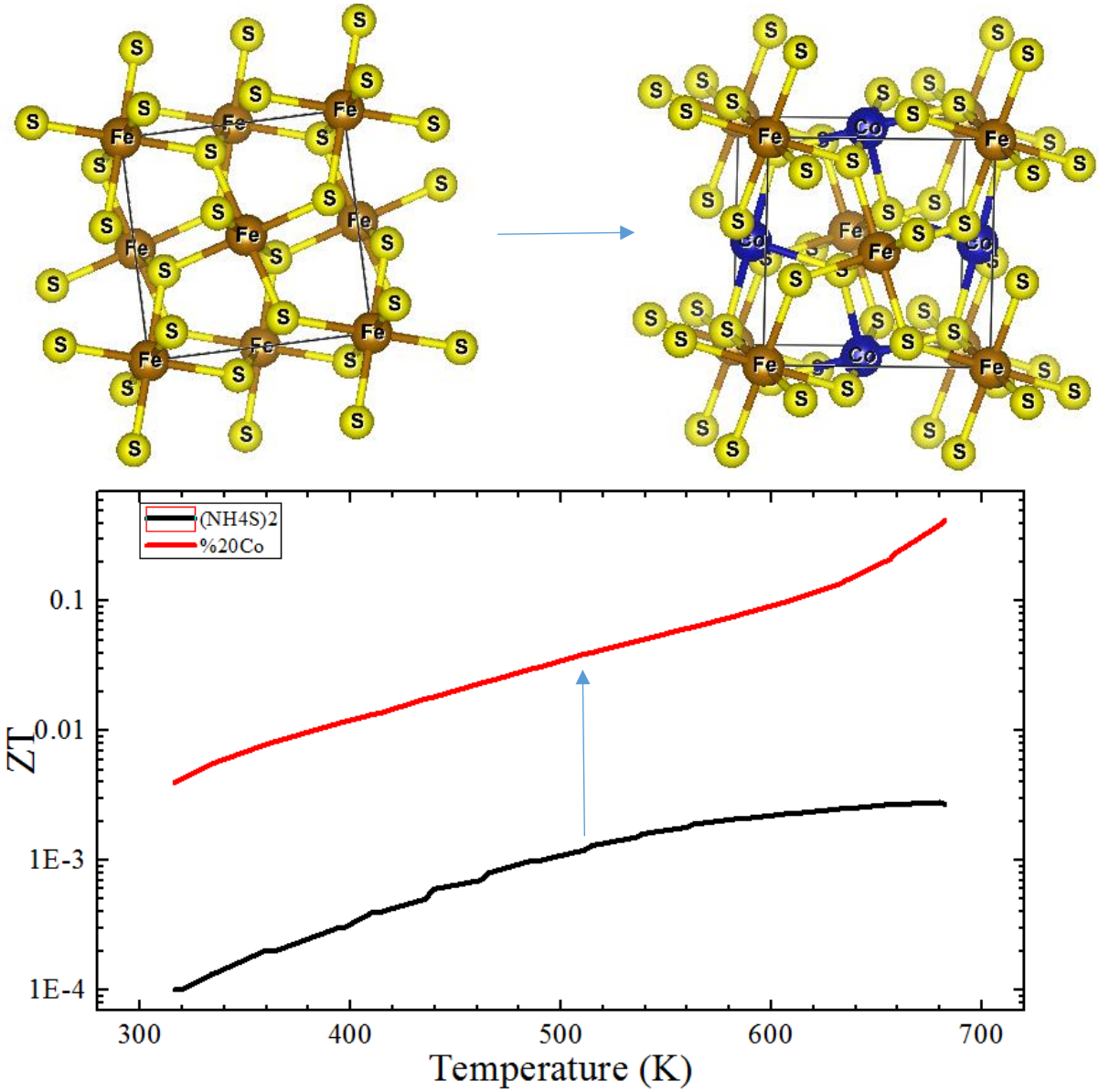

Figure 32: Chapter 5 Highlights

FeS_2 has been investigated because of its interesting characteristics that made it suitable for various energy applications, from solar cells, to batteries. Regarding solar cell applications, its unique properties are a high absorption coefficient allowing it to absorb most of the visible light at thicknesses lower than 100 nm, and its price as it is the most common sulfide mineral. Despite

these advantages, making viable solar cells based on iron pyrite proves to be a daunting task. Many defects arise during and after the synthesis and cause the low performances of the cells. One of the defects results sometimes in the metal like conductivity of the FeS_2 films. While this defect makes iron pyrite not yet suitable for solar, other applications could take advantage of it. The idea was to see if this metal like conductivity could be put to good use in thermoelectric applications. The hope was that FeS_2 would conduct electrons just like a metal but will differ from metal when it comes to heat propagation. The figure of merit, which dictates how good a thermoelectric material performs is calculated using the following equation.

$ZT = \frac{\sigma S^2}{\kappa} T$, Figure of merit

- Peltier effect: ΔT from ΔV
- Seebeck effect: ΔV from ΔT

$$S = \frac{\Delta V}{\Delta T}$$

Seebeck coefficient

σ: electrical conductivity

κ: thermal conductivity

5.1. Thermoelectric properties of undoped FeS_2

The thermoelectric properties of iron pyrite were measured. It was investigated, how the ligands impacted the thermoelectric properties of the FeS_2. First, the thermoelectric properties of the iron pyrite nanoparticles before ligand exchange were measured. To do so, the nanoparticles were synthesized using the hot injection method synthesis previously described. After the synthesis, the nanoparticles were dried under vacuum for several hours. Once dried, the particles

were crushed in a mortar to make a powder. It was followed by the annealing of the powder at 400°C under argon atmosphere. This is done to increase the size of the grains. Grains size impacts the electron transport in the material. The annealing also decomposed any remaining organic impurity at the surface of the nanoparticles. Grains size also impacts phonon transports, therefore there needs to be a compromise for the optimum size of the grains. The annealing also serves to tell if iron pyrite could change phase during the measurement. After annealing, the powder was loaded into a graphite die and the it was put under a hot-pressed machine to make the iron pyrite pellet. Around 1 g of material was needed to make each pellet. The hot-press was custom made. Its mode of operation is the following. First, the machine applied 40 MPa axial pressure, then the sample is heated up to 400°C. This temperature is maintained for 5 minutes. At the end, the pressure is relaxed and the sample is cooled down. The thickness of the pellets was around 1 millimeter. The density of the pellets was measured with a pycnometer and was found to be around 85 %. Three pellets were made and the results presented here are the average of the three values. It is the same principle for the undoped particles after ligand exchange and the doped nanoparticles.

The thermal conductivity was calculated by using the following the formula from Equation (18), $\kappa = DC_p\rho$ (18). D is the thermal diffusivity, C_p is the heat capacity and ρ is the density. The thermal diffusivity was measured using a XFA 600 Xenon Flash, heat capacities were approximated from the literature [115] and the density was measured using the Archimedes principle.

After having looked at the thermoelectric properties of the nanoparticles before ligand exchange, it is time to look at the thermoelectric properties of iron pyrite nanoparticles after ligand exchange. The amount of material that was required to make the pellets was so important, that it was decided to only use one set of ligands. To decide which samples to choose, three samples with

each ligand were annealed at 400°C for 1 hour. After the annealing step the samples were characterized using XRD, to see which sample ligand was the most stable at that temperature. Only the sample with $(NH_4)_2S$ ligands remained pure pyrite. This agreed with the results from the previous chapter where it was found that the nanoparticles with $(NH_4)_2S$ ligands exhibited the best stability; therefore the $(NH_4)_2S$ ligands were chosen. The XRD of the iron pyrite nanoparticles $(NH_4)_2S$ ligands in solution, powder and powder after annealing are presented in Figure 33. The XRD in solution was done before ligand exchange. This can be easily seen by the increase of (311) peak, that was also seen when the XRDs after ligand exchange were presented in the previous chapter. As it can be seen the change of the pyrite did not change after annealing.

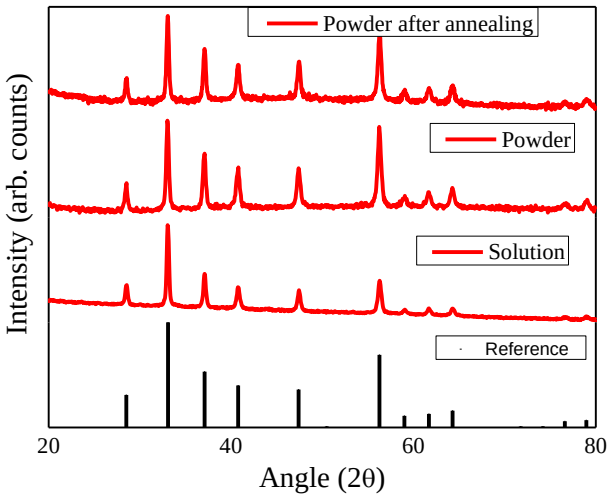

Figure 33: XRD of FeS_2 in solution as a powder and after annealing

The powder was then hot pressed to make a pellet. The thermoelectric properties of the pellets were measured. First, the conductivity as a function of the temperature was measured. The measurements were done using a LSR-3 Linseis instrument. The instrument uses the four-point probe technique to calculate the resistivity. The temperature was varied from room temperature to

400˚C. The results of the electrical conductivity and the seebeck coefficient are presented in Figure 34.

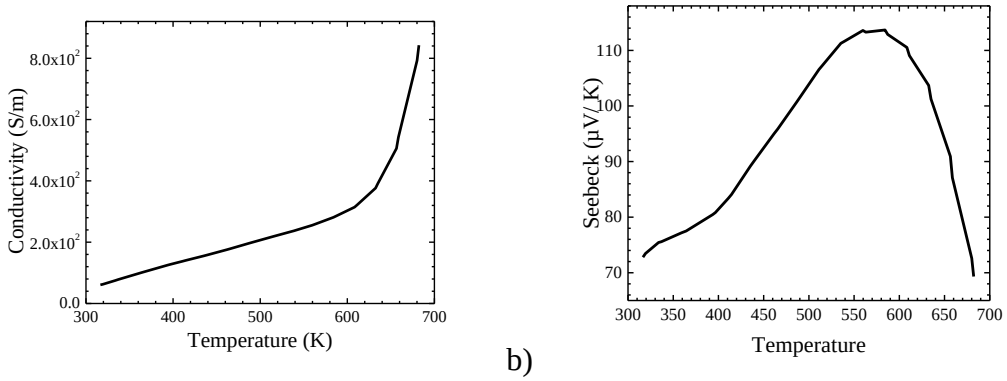

a) b)

Figure 34: Electrical properties of iron pyrite nanoparticle, a) the electrical conductivity and b) the seebeck coefficient.

The conductivity at room temperature is around 60 S/m and gained more than 1 order of magnitude at 400˚C. The graph of the conductivity is composed of two linear parts with two different slopes. The first slope is lower than the second slope. The first slope is mainly due to the thermal activation that allows the promotion of charged carriers. The second higher slope is due to inversion of the charged carriers responsible for the current. At the beginning, only holes are responsible for the conductivity. This later point is correlated by the seebeck coefficient. Positive seebeck, means that the conductivity is p type, therefore hole-type conductivity. As the temperature increases, an inversion in the type of the charge carriers responsible for the conductivity start to occur. This phenomenon is shown by the change of sign of the seebeck coefficient slope around 550 K. The seebeck goes from 113 μV/ K back to 70 μV/ K for temperature between 560 K and 682 K. The seebeck would have eventually become negative if the temperature was increased further. The participation of the electrons in the conductivity justify the higher slope, electrons have higher mobility than holes.

The thermal conductivities were calculated next and the data were used to find the thermopower. The results are presented in Figure 35. The thermal conductivity is not high. It varies in the interval between 1.1 and 1 Wm-1/K. The thermal conductivity first increases as the temperature increases but then started to decrease and then remained steady around 1 Wm-1/K. The decrease is probably due to the grain boundaries which started to prevent the propagation of the phonon. The thermopower was calculated and it was considerably low, in the order of 10^{-3}. The thermopower was one order of magnitude lower than the record of iron pyrite ZT from the literature [78]. The ZT was this low because despite the low thermal conductivity, the electrical conductivity was also low. The thermo-power was considerably low, in the order of 10^{-3}. To further increase the conductivity, the nanoparticles will be doped using cobalt in the next part of this chapter. The hope was that the electrical conductivity will increase but the grain boundaries will prevent the same type of increase for the thermal conductivity.

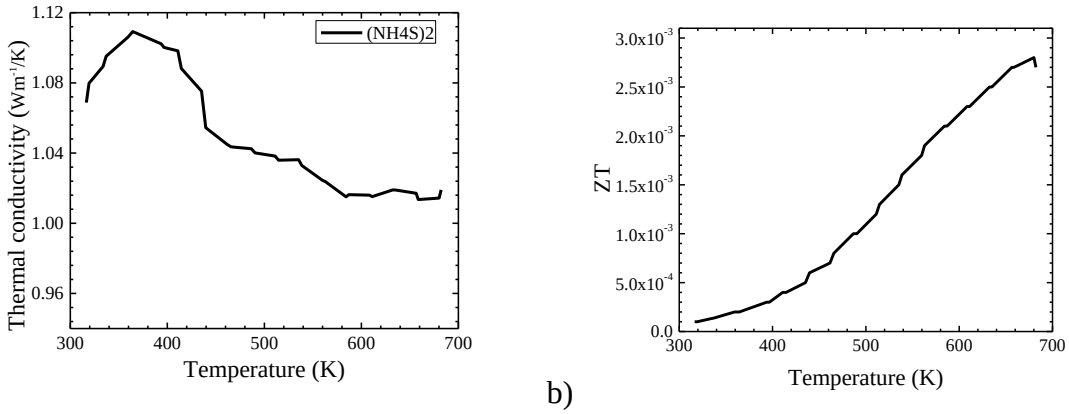

a) b)

Figure 35: The thermal properties of iron pyrite nanoparticles, a) thermal conductivity and b) thermo-power or ZT

5.2. Thermoelectric properties of doped FeS_2

To increase the electrical conductivity of the iron pyrite pellet, it was decided to dope it. The choice of the dopant went to cobalt, because of the advantages it present compared to the other

possible dopant like nickel and arsenic [77]. The hope was that the doping would boost the conductivity by more than 1 order of magnitude, while at the same time keeping the thermal conductivity mostly unchanged. This would put the ZT in the order of 10^{-1}. Once the dopant was chosen, the next step was to figure out how to do it with hot injection method, or if another method would be required. The nucleation temperature of CoS_2 is lower than the nucleation temperature of FeS_2, making it difficult to synthesize $Fe_{1-x}Co_xS_2$, without making at the same time CoS_2, using hot-injection method. The answer on how to do it using hot injection came from a paper by Prof. Stoldt at the University of Colorado [98]. In this paper, the author synthesized big cubic iron pyrite nanoparticles by separating the nucleation step from the growth step. First the nucleation step was done by synthesizing iron pyrite, the regular way. After the nucleation step, the flask was cooled down to room temperature. While still circulating argon in the flask, more iron precursor, sulfur elemental and amine were added into the mix. The flask was then heated up again but the temperature this time was a lower temperature than the nucleation temperature. To reduce the surface energy, the already synthesized particles came together to form cubes. The extra precursors were also used for the growth of the cubes as the temperature did not allow nucleation. The idea was to use the same principle, separate nucleation of the iron pyrite, and then add some cobalt into FeS_2 matrix during the growth step. First, the experiment with just iron pyrite was done to make sure it was reproducible. The results are presented in Figure 36. Using the Scherrer method on the (200) peak located at $2\theta = 33$, the average sizes of the nanoparticles were approximated to be 21 nm after the nucleation, 53 nm after the first growth and 78 nm after the second growth. As expected the average size of the particles increase after each step, showing that step 2 and 3 are in fact growth steps.

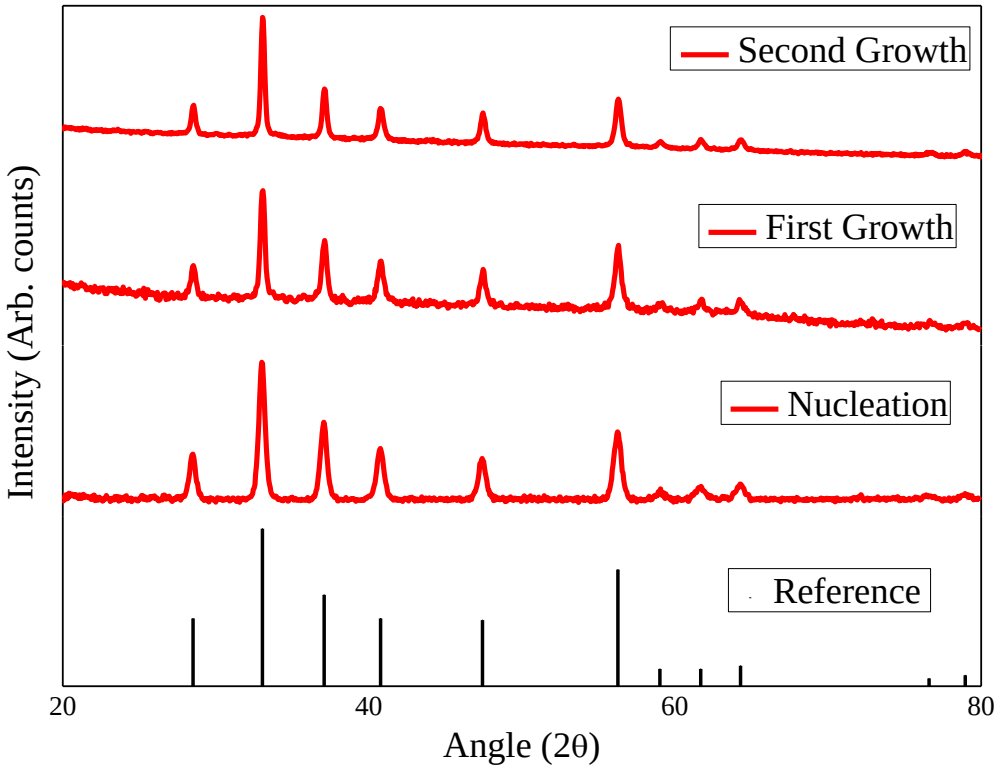

Figure 36: XRD of iron pyrite nanoparticles after the nucleation, first growth and second growth steps

Now, that the reproducibility of the method was verified, the next step was the doping. One key element is still missing, the nucleation temperature of CoS_2. To find the temperature, a sweep of temperatures was done starting from 100˚C and going up. Nothing happened until 180˚C. The nanoparticles synthesized at 180˚C are presented in Figure 37 along with the XRD. There are some impurities but the nanoparticles at that temperature started to have the cobalt pyrite phase. The temperature for the growth step should then be below 180˚C

a)

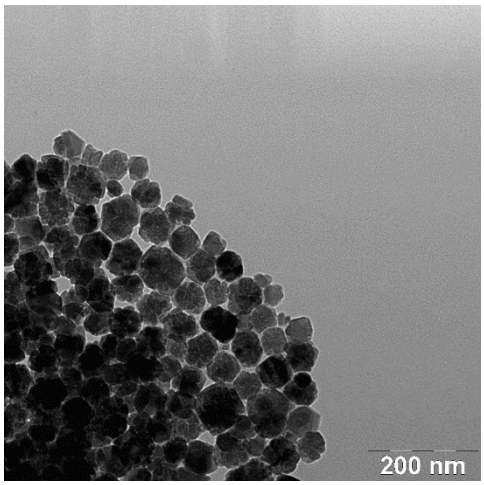

b)

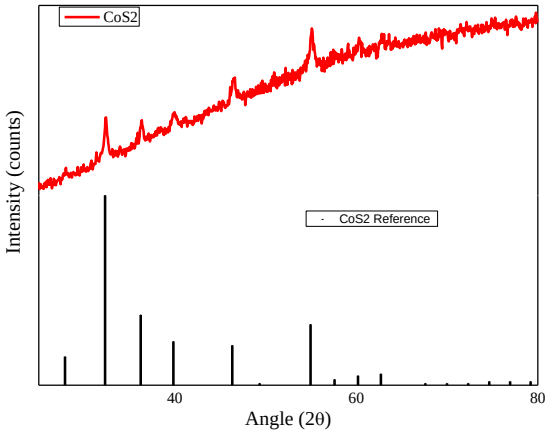

Figure 37: a) TEM image of CoS2 nanoparticles synthesized at 180˚C and their b) XRD

First a nucleation process involving only Fe and sulfur precursor, followed by a growth process at a temperature lower than the nucleation temperature of CoS_2, where Co, Fe, S precursors were introduced in the flask. The $Fe_{1-x}Co_xS_2$ nanoparticles with different concentrations of Co (5, 10, 15 and 20 percent) were characterized using XRD, SEM-EDX. The XRD measurements of the doped nanoparticles are presented in Figure 38. It can clearly be seen that as the concentration of the cobalt increases, the peaks in the XRD of the nanoparticles move toward the peak of the cobalt pyrite reference and away from the peaks from the iron pyrite reference.

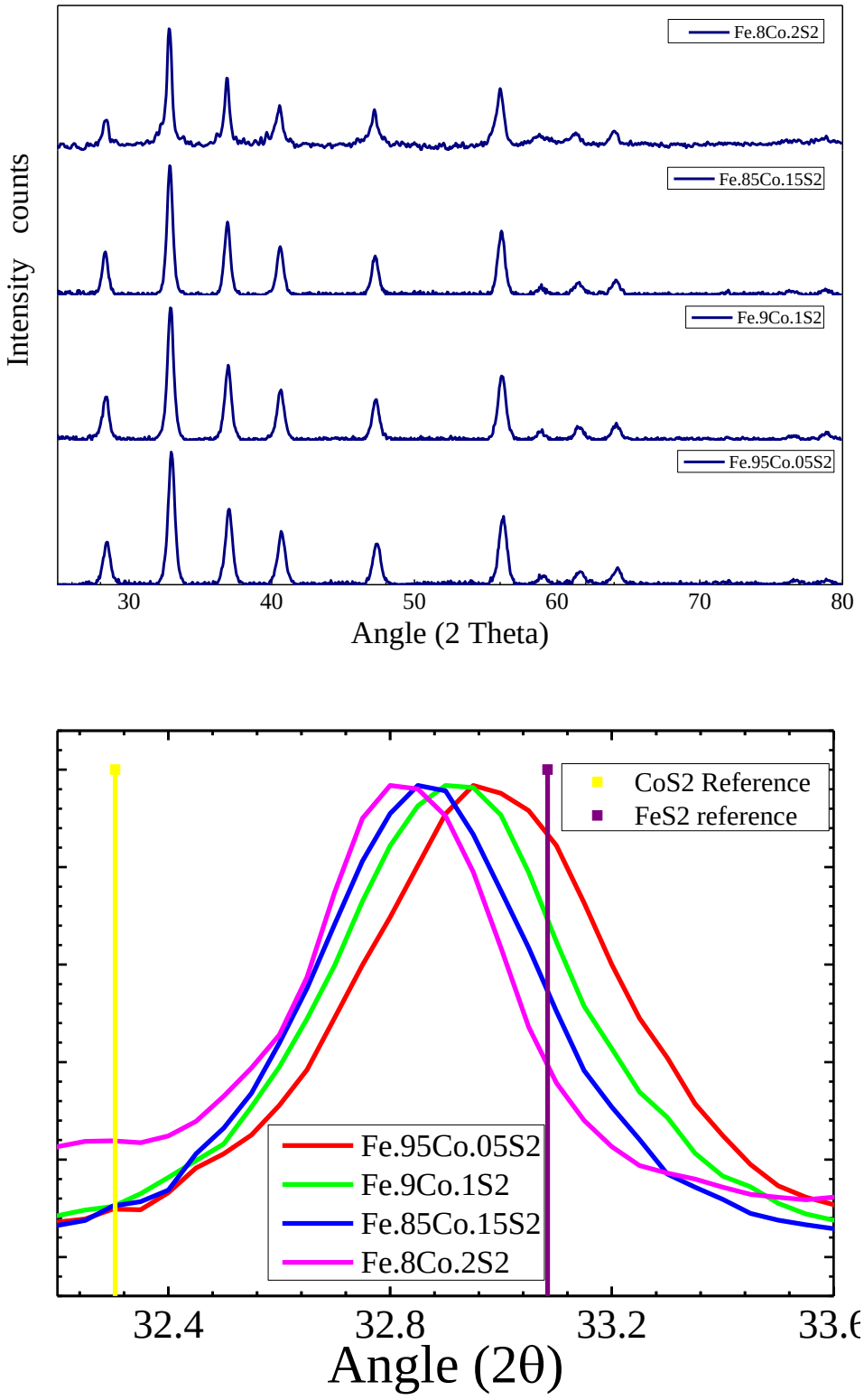

Figure 38: XRD of $Fe_{1-x}Co_xS_2$ nanoparticles

The cobalt doped FeS_2 nanoparticles were also dried, crushed and pressed to make pellets and their thermoelectric properties were measured. The Seebeck coefficient of the different pellets is presented in Figure 39.

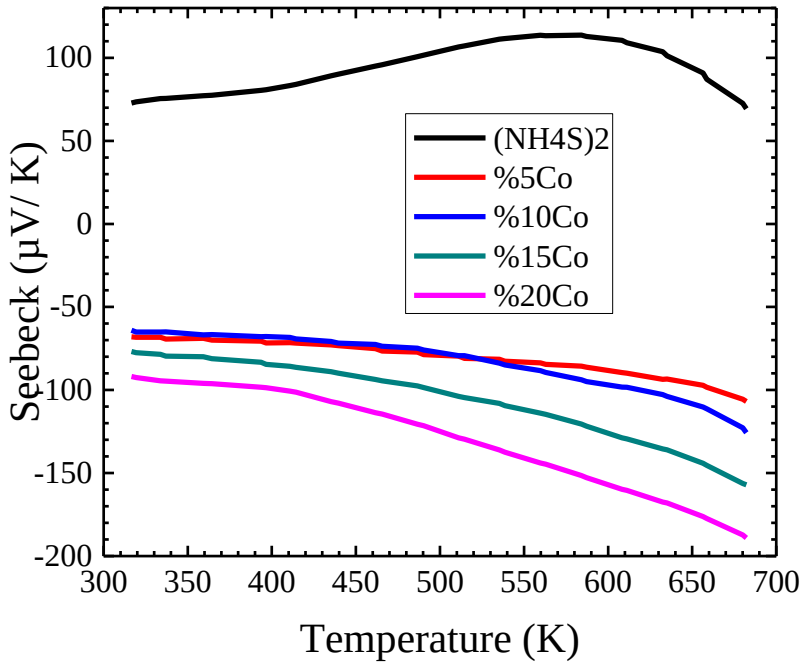

Figure 39: Seebeck of FeS_2 and cobalt doped FeS_2 pellets

When cobalt is introduced in the matrix of the iron pyrite, the seebeck coefficient changes sign and become negative. When the percentage of cobalt is 5, the seebeck coefficient goes from -67 to -107 µV/ K. When the percentage is 10, the seebeck coefficient goes from -64 to -125 µV/ K. When the percentage of cobalt is 15, the seebeck coefficient goes from -76 to -157 µV/ K. When the percentage is 20, the seebeck coefficient goes from -91 to -189 µV/ K. Unlike, the seebeck of the undoped material, the slope does not change sign. There are just more electrons participating in the conduction.

The electrical conductivity is presented in Figure 40. As expected because cobalt acts as a donor for iron pyrite, the conductivity of the nanoparticles switched from p-type to n-type after introduction of cobalt. With the mobility of electrons 2 order of magnitude higher than the mobility of hole, it is easy to understand why there is such an increase in the electrical conductivity after cobalt doping. The electrical conductivity in average was respectively multiplied by 18, 25, 61 and 112 when the concentration of cobalt in the iron pyrite matrix was 5, 10, 15 and 20 per cent.

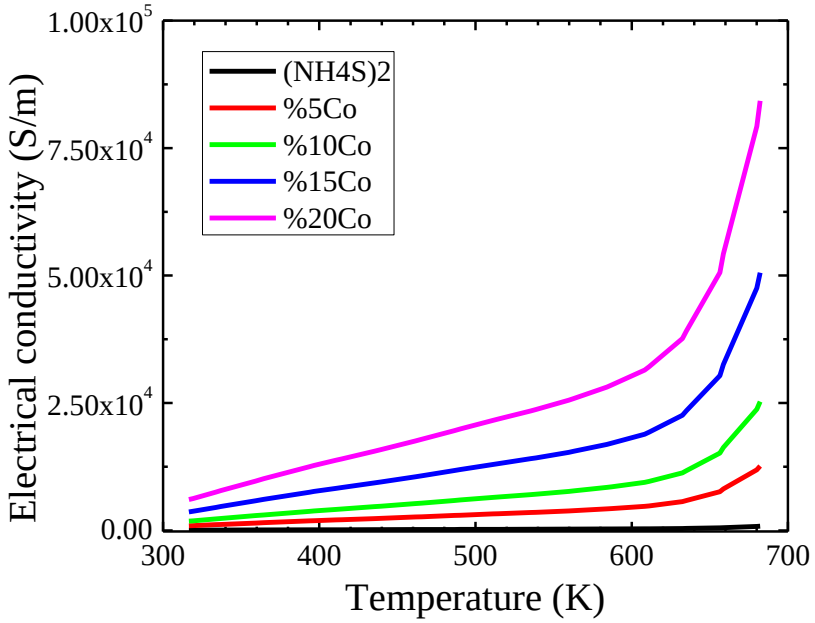

Figure 40: Electrical conductivity of FeS_2 and cobalt doped FeS_2 pellets

The thermal conductivity was calculated and the results are presented in Figure 41. The thermal conductivity also increases, but the percentage increase is not the same. This is due to the grain boundaries obstructing the propagation of phonons inside the pellet. It was around 1.5 for $Fe_{.95}Co_{.05}S_2$. It was around 2 for $Fe_{.9}Co_{.1}S_2$. It was around 3 for $Fe_{.85}Co_{.15}S_2$. For $Fe_{.8}Co_{.2}S_2$, it started at 4 and increase to later stay steady around 5.

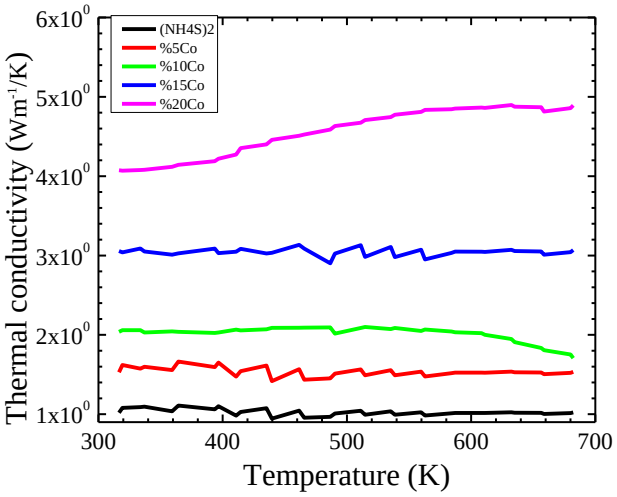

Figure 41: Thermal conductivities of FeS_2 and cobalt doped FeS_2 pellets

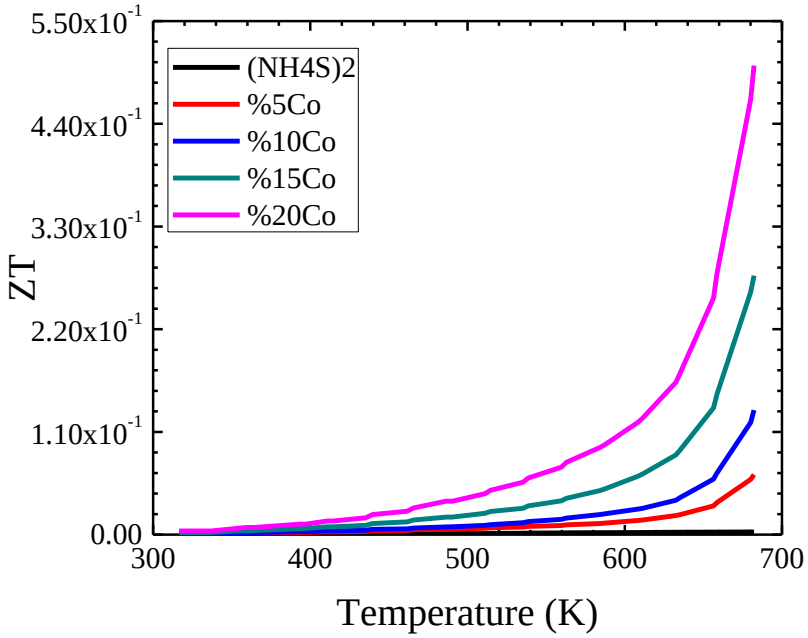

Figure 42: ZT values of Iron Pyrites and Iron pyrite doped with different concentration of cobalt

The ZT power was calculated from all the other parameters and the results are presented in Figure 42. The figure of merit almost gained two orders of magnitude because of the important increase of the electrical conductivity and the small increase of the thermal conductivity. This is one order of magnitude higher than the record ZT of iron pyrite material [78]. More work needs to be done to further improve the figure of merit but it is a step in the right direction. The scalability of the synthesis needs to be improved and the electrical conductivity can be further improved by changing the ligands at the surface of cobalt doped iron pyrite nanoparticles.

Cobalt doped iron pyrite nanoparticles were successfully synthesized using hot injection method. The record thermopower of 0.5 was found at 673 K for $Fe_{.8}Co_{.2}S_2$. This was achieved by considerably increasing the electrical conductivity, while at the same time only slightly increasing the thermal conductivity. Now, that the electrical conductivity was successfully increased the next step is to increase the optical properties.

CHAPTER 6: COUPLING WITH METALLIC MATERIALS AND SIMULATION

After showing that the electrical properties of iron pyrite could be greatly enhance, the next step was to try to do the same thing but this time with the optical properties. To do so, it was decided to couple FeS_2 with metallic nanostructures of gold and silver. The idea was to use the plasmonic behavior of the metal to increase the amount light absorbed from iron pyrite. In this chapter, it will be investigated if the metallic nanostructures act as traps for the photogenerated carriers. In the even such phenomenon occurs, it will be investigated if the plasmonic effects can overcome the effects of the traps. This investigation could help further decrease the thickness of the active layer of solar cells or other optoelectronic devices; therefore, decrease the cost of these devices. The first part of this chapter will deal with the experimental results of the coupled particles, while the second will present simulation results of the coupled nanoparticles.

6.1. Coupling with Au and Ag nanoparticles

6.1.1. FeS_2/Au synthesis

The coupling with Au nanoparticles was done in two steps. The two different particles were synthesized separately and then they were mixed together. The synthesis of the FeS_2 nanoparticles remained mainly the same than the one presented in chapter 4 with just small difference. At the end of the synthesis, instead of injecting chloroform at 75°C, toluene was injecting instead. Toluene was also the solvent that the nanoparticles were dispersed in, at the end of the purification steps. Toluene was used in this case because the Au nanoparticles were dispersed in toluene. The solvent of the two different nanoparticles needs to be the same for the coupling to happen, and the synthesized Au nanocrystals were not soluble in chloroform.

For the synthesis of Au nanocrystals, the procedure is shown in the Figure 43. Basically, gold chloride, was dissolved in toluene in the presence of didecyldemethylammonium bromide and dodecylamine. The mixture was sonicated at room temperature. The sonication was stopped when the previously dark orange colored solution changes to light yellow. The absorption spectra of the gold nanoparticles in toluene is presented in Figure 44. The spectrum is what is expected from the plasmonic peak of gold nanoparticles. The plasmonic peak here is around 530 nm.

EXPERIMENTAL NOTE

Page. 1

Sample name: Au Nanoparticles Num.

Date	Time	Chemicals	Temp.	Notes
03/10/15	*12:37*	$AuCl_3$: 40 mg	RT	Sonicate the mixture.
		Didecyldemethylammonium : 40 mg Bromide (DDAB)		Color: Orange
		Dodecylamine : 140 mg		
		Toluene : 4 mL		
	1:12		RT	Color: Light yellow

Figure 43: Procedure for the synthesis of Au nanoparticles

The synthesis of the couple FeS_2/Au nanoparticles was done by adding drop wise the solution of Au nanoparticles in the solution of iron pyrite. Here, it is imperative to make sure that the particles are well disperse in the solution. At least that they should not precipitate to the bottom before adding the metallic nanostructures, but to have optimum result a well disperse solution is a must. It is also important to add the Au dropwise, faster rates do not achieve the best results. With faster rates only some particles are coupled and not all of them. The coupling was done and the absorption spectra was measured. The spectra before and after did not show any difference, this is due to the big difference in size between the semiconductor particles and the metallic

nanostructures at their surface. The effects of the metallic were so negligible that they could not be measured using UV-Vis.

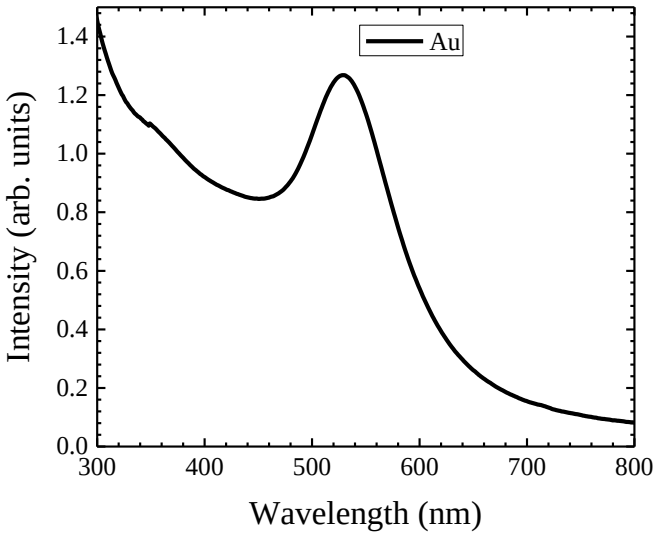

Figure 44: UV-Vis spectrum of Au nanoparticles

To approximate the ratio between the sizes of the semiconductor nanoparticle and the metallic nanostructures, the coupled nanoparticles were characterized using XRD. The results are presented in Figure 45. The XRD of the coupled nanoparticles shows that the iron pyrite did not change phase during, the coupling. The position of the peak of Au are a little bit shifted from the reference spectra. This shift put the (111) peak that is positioned at 38 degree on the reference spectra next to an iron pyrite peak. This results in the camouflage of the small gold peak by the bigger peak from the semiconductor. The peak corresponding to the (200) orientation that is located 44 degree can be seen, but it is weak. The ratio between the peak corresponding to the iron pyrite and the peak corresponding to gold was used to approximate the ratio in size between the semiconductor and the metallic nanostructure. The peak corresponding to the (200) orientation

were used for both FeS_2 and Au. The ratio was found to be about 20. This further explains the absence of the plasmonic peak in the absorption spectrum of the coupled nanoparticles.

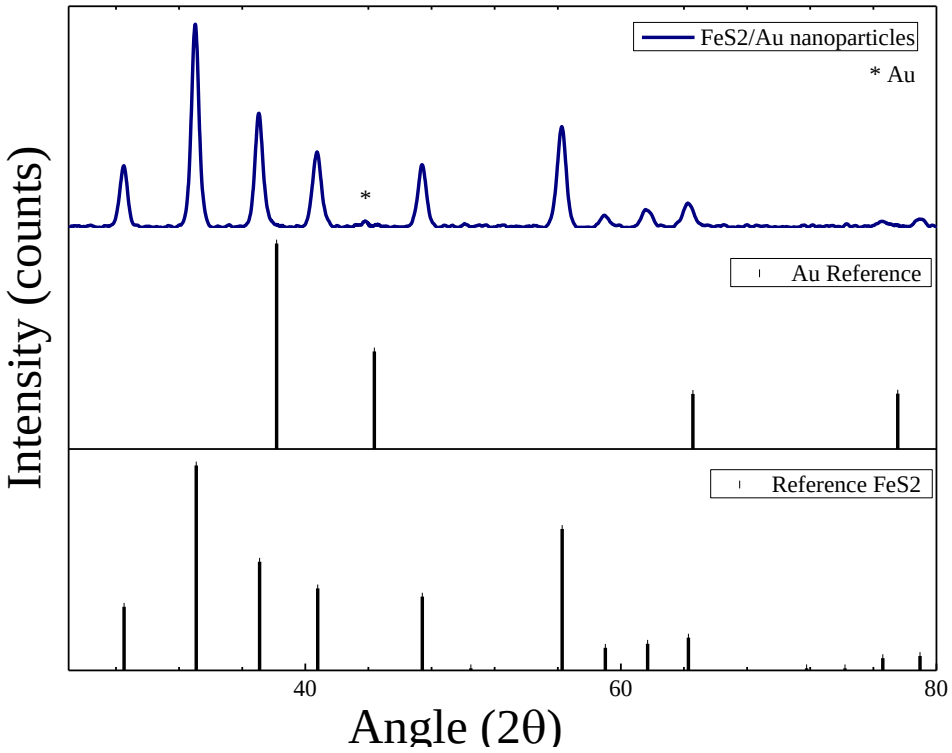

Figure 45: The XRD of the coupled FeS_2/Au nanoparticles

The next thing was to measure the PL of the nanoparticles before and after the coupling to see if a change could be notice in the luminescence spectra. The luminescence spectra of the particles before and after ligand exchange is presented in Figure 46. The results show that after the coupling, the luminescence was quenched. Just like in the case of the ligand exchange, the metallic particles introduced states within the band gap of the iron pyrite. These states act as traps that prevent some of the electrons from decaying to the ground state. This results in the reduction of the number of electrons that undergo radiative relaxation. The plasmonic effect of the gold nanoparticles could not overcome the effect of the traps.

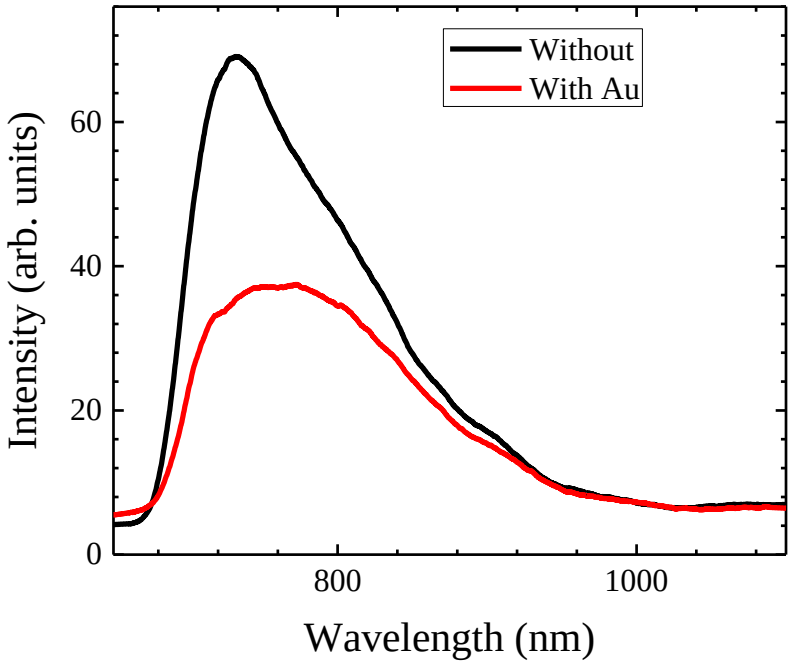

Figure 46: Photoluminescence spectra of FeS_2 nanoparticles before and after coupling with Au nanostructure.

6.1.2. FeS_2/Ag synthesis

For the coupling part with silver nanocrystals, two methods were used. In the first method, galvanic replacement was done on the FeS_2 coupled with Au nanoparticles using silver nitrate. For the second method after the synthesis of iron pyrite nanoparticles, the reactor was cooled down to room temperature. Silver nitrate dissolved in oleic acid was then injected in the reactor, the reactor was again heat up to the temperature required, 120˚C, for the formation of silver nanoparticles. After the synthesis, the product was washed with chloroform and acetone or ethanol and then dispersed in chloroform. The absorption spectrum of the silver nanoparticles when synthesized separately is presented in Figure 47. The plasmonic peak of the silver nanoparticles is around 410 nm.

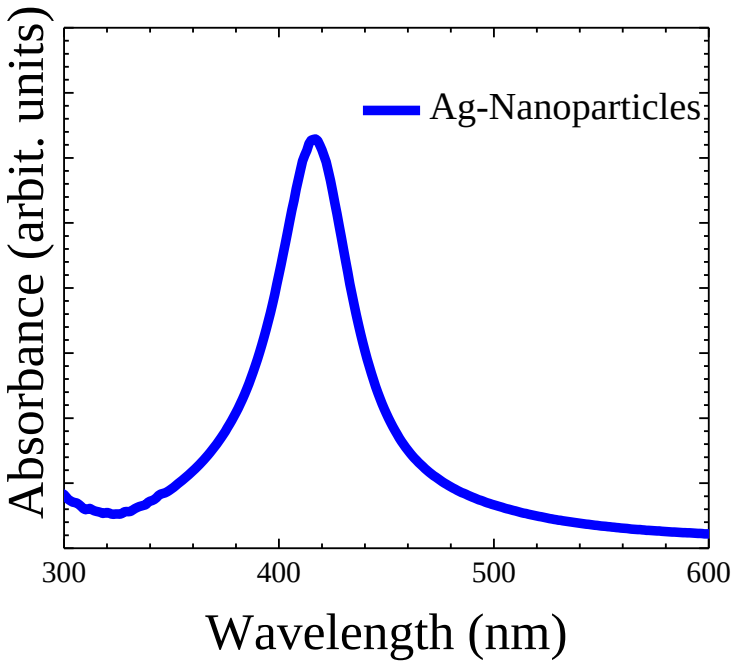

Figure 47: UV-Vis spectrum of Ag nanoparticles

Raman and XRD were measured for the coupled nanoparticles and presented in Figure 48. These characterizations were used to ensure that the iron pyrite did not change phase during the coupling and that there was no formation of silver sulfide (Ag_2S) during the synthesis. The raman spectrum of the nanoparticles after coupling shows that there is in fact just FeS_2 pyrite and no presence of Ag_2S. The XRD measurement confirmed the presence of the silver element. Using the same peak ratio method, the ratio between iron pyrite and silver was approximated to be around 15.

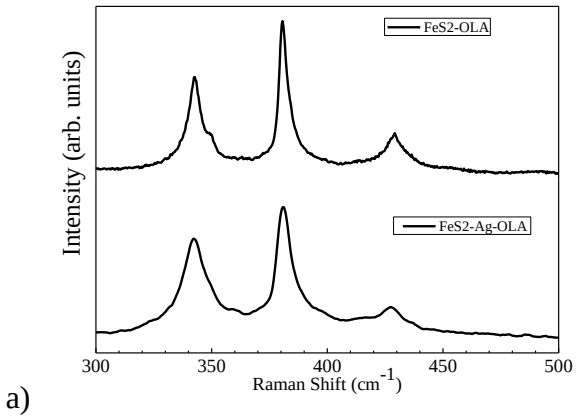

a)

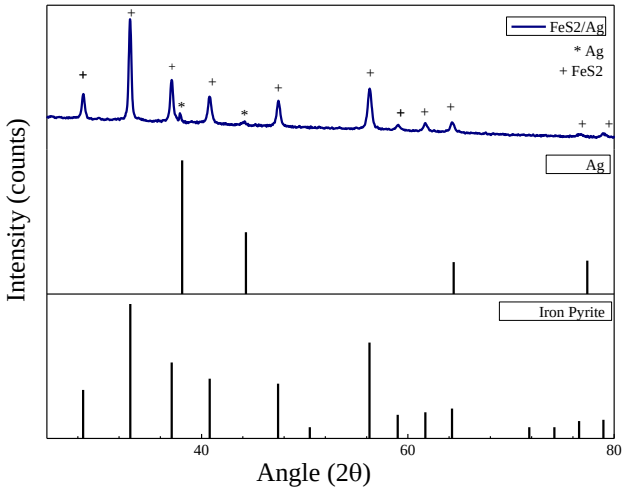

b)

Figure 48: a) Raman Spectra of FeS_2 and FeS_2/Ag nanoparticles and b) XRD of the coupled nanoparticles

The absorption spectra of the FeS_2 nanoparticles with and without Ag is shown. There is a small increase in the absorption around the silver plasmonic region. Caution is required before concluding that the increase is due to plasmonic enhancement from the silver nanoparticles, considering that it is just a small increase. Even if this increase was due to plasmonic enhancement, the metal nanoparticles do not need to be coupled to the FeS_2 nanoparticle for it to happen. The micro-PL spectra of FeS_2 nanoparticles with and without Ag nanocrystals is presented Figure 49.

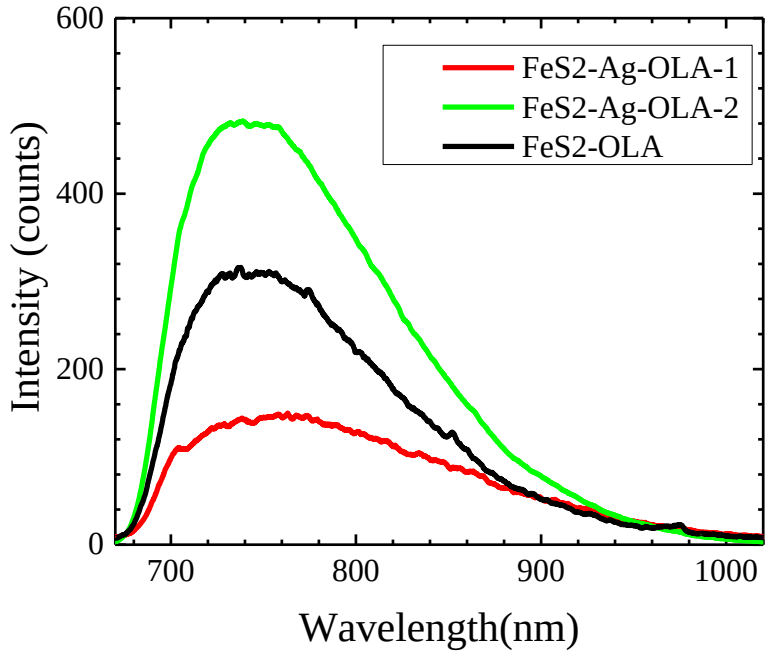

Figure 49: PL spectra of iron pyrite nanoparticle uncoupled and coupled with the two methods

For the FeS_2/Ag nanoparticles that were synthesized by galvanic replacement, here the red graph, the PL was lower than the PL of the particle before the coupling. The nanoparticles grown using the second method saw an increase in the PL. this change can be due to the size of the metallic nanostructures attached to the surface of the semiconductor. The bigger the size of the metallic particle, the more it can overcome the effect of the traps that were introduced inside the bandgap of iron pyrite during the coupling. The difference in size were approximated using the ratio between the peaks of pyrite and the metallic nanostructures in the XRD of the coupled nanoparticles, but this ratio could not be confirmed because of the lack of TEM images. Simulations of the optical properties of the coupled nanoparticles were done to study the effect of the size plasmonic nanostructures on the optical properties of the semiconductor.

6.2. Simulations

For the simulations, two methods will be investigated in this dissertation. These are finite-difference time-domain (FDTD) and finite-difference frequency-domain (FDFD). Formulation of both methods start with the Maxwell equations and the constitutive equations to fully describe classical electrodynamics.

6.2.1. Finite different time domain (FDTD)

$$\nabla \times \vec{H} = \vec{J} + \frac{\partial \vec{D}}{\partial t} \quad (19) \qquad \nabla \bullet \vec{B} = 0 \quad (21) \qquad \vec{D} = \varepsilon \vec{E} \quad (23)$$

$$\nabla \times \vec{E} = -\frac{\partial \vec{B}}{\partial t} \quad (20) \qquad \nabla \bullet \vec{D} = \rho_{\mathrm{v}} \quad (22) \qquad \vec{B} = \mu \vec{H} \quad (24)$$

Eqs. (19) to (22) are the Maxwell equations and Eqs. (23) and (24) are the constitutive equations. Assuming the device is far away from any source; therefore $\rho_{\mathrm{v}} = 0$ and there is no current, $\vec{J} = 0$, the 6 equations become:

$$\nabla \times \vec{H} = \frac{\partial \vec{D}}{\partial t} \quad (25) \qquad \nabla \bullet \vec{B} = 0 \qquad \vec{D} = \varepsilon \vec{E}$$

$$\nabla \times \vec{E} = -\frac{\partial \vec{B}}{\partial t} \qquad \nabla \bullet \vec{D} = 0 \quad (26) \qquad \vec{B} = \mu \vec{H}$$

To obtain the previous equations, it was assumed that the material was linear, isotropic and non-dispersive. Incorporating Eqs. (23) and (24) in Eqs. (25) and (20) gives

$$\nabla \times \vec{H} = \varepsilon \frac{\partial \vec{E}}{\partial t} \quad (27)$$

$$\nabla \times \vec{E} = -\mu \frac{\partial \vec{H}}{\partial t} \quad (28)$$

The time derivatives can now be approximated using finite differences

$$\nabla \times \vec{H} = \varepsilon \frac{\vec{E}(t+\Delta t) - \vec{E}(t)}{\Delta t} \qquad (29) \qquad\qquad \nabla \times \vec{E} = -\mu \frac{\vec{H}(t+\Delta t) - \vec{H}(t)}{\Delta t} \quad (30)$$

The right parts of the equations 9 and 10 exist at the middle point between $t + \Delta t$ and t, while the left parts of the equations exist at t; therefore, this formulation is not correct and may be unstable. Each term in the finite difference equation is most accurate when all the terms of the equation exist at the same point in time and space. To solve this problem, the fields E and H were staggered in time so that they exist at different time steps. The electric field E exists at integer time steps (0, Δt , 2 Δt ,…). The H field exists at half time steps, (Δt /2, 3/2 Δt ,…).

The time derivatives can be rewritten as

$$\nabla \times \vec{H}_{(t+\Delta t/2)} = \varepsilon \frac{\vec{E}_{(t+\Delta t)} - \vec{E}_{(t)}}{\Delta t} \qquad (31) \qquad\qquad \nabla \times \vec{E}_{(t)} = -\mu \frac{\vec{H}_{(t+\Delta t/2)} - \vec{H}_{(t-\Delta t/2)}}{\Delta t} \quad (32)$$

Eqs. (31) and (32) were rearranged to solve for the future terms of the H and E fields.

$$\vec{E}_{(t+\Delta t)} = \vec{E}_{(t)} + \frac{\Delta t}{\varepsilon} \nabla \times \vec{H}_{(t+\Delta t/2)} \qquad (33) \qquad\qquad \vec{H}_{(t+\Delta t/2)} = \vec{H}_{(t-\Delta t/2)} - \frac{\Delta t}{\mu} \nabla \times \vec{H}_{(t)} \qquad (34)$$

These are called the “update equations.” They will be used later. The grid that will be used is the “Yee grid”; where instead of positioning the field components within the grid cell at the origin of the cell, the field components are staggered within the grid cell. The reason for this choice is to have a divergence free model where $\nabla . \vec{D} = 0$ and $\nabla . \vec{B} = 0$ are satisfied implicitly. Further, the physical boundary conditions are satisfied and it is an elegant arrangement to approximate Maxwell curl equations with finite differences. The physical boundary conditions here are the continuity of the tangential components of E and H across an interface as well as the continuity of the normal components of D and B across an interface.

The E and H fields are three orders of magnitude different because they are related through impedance. This can cause rounding errors in the simulations. It is good practice to normalize the parameters in a simulation so that they are all the same order of magnitude. In this report, the magnetic field was normalized but the electric field could have been normalized instead.

$\overrightarrow{H} = \sqrt{\frac{\mu_0}{\varepsilon_0}}\vec{H}$, $\sqrt{\frac{\mu_0}{\varepsilon_0}}$ is the free space impedance. The curl equations of E and H become:

$$\nabla \times \overrightarrow{H} = \frac{\varepsilon_r}{c_0}\frac{\partial \vec{E}}{\partial t} \quad (35) \qquad \nabla \times \vec{E} = -\frac{\mu_r}{c_0}\frac{\partial \overrightarrow{H}}{\partial t} \quad (36)$$

ε_r and μ_r are the dielectric constant and the relative permeability of the material. Expanding the curl equation, the following equations can be derived

Curl of E

$$\frac{dE_z}{dy} - \frac{dE_y}{dz} = -\frac{1}{c_0}\left(\mu_{xx}\frac{dH_x}{dt} + \mu_{xy}\frac{dH_y}{dt} + \mu_{xz}\frac{dH_z}{dt}\right) \quad (37)$$

$$\frac{dE_x}{dz} - \frac{dE_z}{dx} = -\frac{1}{c_0}\left(\mu_{yx}\frac{dH_x}{dt} + \mu_{yy}\frac{dH_y}{dt} + \mu_{yz}\frac{dH_z}{dt}\right) \quad (38)$$

$$\frac{dE_y}{dx} - \frac{dE_x}{dy} = -\frac{1}{c_0}\left(\mu_{zx}\frac{dH_x}{dt} + \mu_{zy}\frac{dH_y}{dt} + \mu_{zz}\frac{dH_z}{dt}\right) \quad (39)$$

Curl of H

$$\frac{dH_z}{dy} - \frac{dH_y}{dz} = \frac{1}{c_0}\left(\varepsilon_{xx}\frac{dE_x}{dt} + \varepsilon_{xy}\frac{dE_y}{dt} + \varepsilon_{xz}\frac{dE_z}{dt}\right) \quad (40)$$

$$\frac{dH_x}{dz} - \frac{dHz}{dx} = \frac{1}{c_0}\left(\varepsilon_{yx}\frac{dE_x}{dt} + \varepsilon_{yy}\frac{dE_y}{dt} + \varepsilon_{yz}\frac{dE_z}{dt}\right) \quad (41)$$

$$\frac{dH_y}{dx} - \frac{dH_x}{dy} = \frac{1}{c_0}\left(\varepsilon_{zx}\frac{dE_x}{dt} + \varepsilon_{zy}\frac{dE_y}{dt} + \varepsilon_{zz}\frac{dE_z}{dt}\right) \quad (42)$$

Assuming the dielectric constant and the relative permeability are just diagonally anisotropic; therefore, just diagonal tensors, the curl equations can be reduced to:

Curl E

$$\frac{dE_z}{dy}-\frac{dE_y}{dz}=-\frac{1}{c_0}\left(\mu_{xx}\frac{dH_x}{dt}\right) \quad (43)$$

$$\frac{dE_x}{dz}-\frac{dE_z}{dx}=-\frac{1}{c_0}\left(\mu_{yy}\frac{dH_y}{dt}\right) \quad (44)$$

$$\frac{dE_y}{dx}-\frac{dE_x}{dy}=-\frac{1}{c_0}\left(\mu_{zz}\frac{dH_z}{dt}\right) \quad (45)$$

Curl H

$$\frac{dH_z}{dy}-\frac{dH_y}{dz}=\frac{1}{c_0}\left(\varepsilon_{xx}\frac{dE_x}{dt}\right) \quad (46)$$

$$\frac{dH_x}{dz}-\frac{dHz}{dx}=\frac{1}{c_0}\left(\varepsilon_{yy}\frac{dE_y}{dt}\right) \quad (47)$$

$$\frac{dH_y}{dx}-\frac{dH_x}{dy}=\frac{1}{c_0}\left(\varepsilon_{zz}\frac{dE_z}{dt}\right) \quad (48)$$

At this point the two methods start diverging. A finite-difference equation is written for each point on the grid. In FDTD, these equations are iterated over and over until the problem is solved. In FDFD, the equations are assembled into a matrix and solved using linear algebra. FDFD is also a frequency-domain method whereas FDTD is a time-domain method.

Finite Difference Equations for H

$$\frac{E_{z_t}^{i,j+1,k}-E_{z_t}^{i,j,k}}{\Delta y}-\frac{E_{y_t}^{i,j,k+1}-E_{y_t}^{i,j,k}}{\Delta z}=-\frac{\mu_{xx}^{i,j,k}}{c_0}\frac{H_{x_{t+\frac{\Delta t}{2}}}^{i,j,k}-H_{x_{t-\frac{\Delta t}{2}}}^{i,j,k}}{\Delta t} \quad (49)$$

$$\frac{E_{x_t}^{i,j,k+1}-E_{x_t}^{i,j,k}}{\Delta z}-\frac{E_{z_t}^{i+1,j,k}-E_{z_t}^{i,j,k}}{\Delta x}=-\frac{\mu_{yy}^{i,j,k}}{c_0}\frac{H_{y_{t+\frac{\Delta t}{2}}}^{i,j,k}-H_{y_{t-\frac{\Delta t}{2}}}^{i,j,k}}{\Delta t} \quad (50)$$

$$\frac{E_{y_t}^{i+1,j,k}-E_{z_t}^{i,j,k}}{\Delta x}-\frac{E_{x_t}^{i,j+1,k}-E_{y_t}^{i,j,k}}{\Delta y}=-\frac{\mu_{zz}^{i,j,k}}{c_0}\frac{H_{z_{t+\frac{\Delta t}{2}}}^{i,j,k}-H_{z_{t-\frac{\Delta t}{2}}}^{i,j,k}}{\Delta t} \quad (51)$$

Finite Difference Equations for E

$$\frac{H_{z_t}^{i,j+1,k} - H_{z_t}^{i,j,k}}{\Delta y} - \frac{H_{y_t}^{i,j,k+1} - H_{y_t}^{i,j,k}}{\Delta z} = \frac{\varepsilon_{xx}^{i,j,k}}{c_0} \frac{E_{x_{t+\frac{\Delta t}{2}}}^{i,j,k} - E_{x_{t-\frac{\Delta t}{2}}}^{i,j,k}}{\Delta t} \tag{52}$$

$$\frac{H_{x_t}^{i,j,k+1} - H_{x_t}^{i,j,k}}{\Delta z} - \frac{H_{z_t}^{i+1,j,k} - H_{z_t}^{i,j,k}}{\Delta x} = \frac{\varepsilon_{yy}^{i,j,k}}{c_0} \frac{E_{y_{t+\frac{\Delta t}{2}}}^{i,j,k} - E_{y_{t-\frac{\Delta t}{2}}}^{i,j,k}}{\Delta t} \tag{53}$$

$$\frac{H_{y_t}^{i+1,j,k} - H_{y_t}^{i,j,k}}{\Delta x} - \frac{H_{x_t}^{i,j+1,k} - H_{x_t}^{i,j,k}}{\Delta y} = \frac{\varepsilon_{zz}^{i,j,k}}{c_0} \frac{E_{z_{t+\frac{\Delta t}{2}}}^{i,j,k} - E_{z_{t-\frac{\Delta t}{2}}}^{i,j,k}}{\Delta t} \tag{54}$$

6.2.2. Finite difference frequency domain (FDFD)

It was decided to only implement the FDFD method because it seemed like the easiest and most beneficial path. The fact that the dielectric constant of the materials that will be studied changes with the frequency makes it more straightforward to implement in the frequency domain. It is possible to do this in the time-domain but it is not trivial. In the frequency-domain, accounting for dispersion is very easy. FDFD in three-dimension is very computationally intensive. For higher efficiency and faster simulation, the 3D configurations were modeled in 2D so that only 2D FDFD code was required.

Finite difference frequency domain is a frequency domain method, so Maxwell equations formulation was transformed from the time domain to the frequency domain.

$\nabla \times \vec{H} = j\omega \vec{D}$ (55) $\nabla \bullet \vec{B} = 0$ (57) $\vec{D} = \varepsilon \vec{E}$ (59)

$\nabla \times \vec{E} = -j\omega \vec{B}$ (56) $\nabla \bullet \vec{D} = 0$ (58) $\vec{B} = \mu \vec{H}$ (60)

Using the constitutive equations, the two curl equation can be rewritten as:

$$\nabla \times \vec{H} = j\omega\varepsilon \vec{E} \tag{61}$$

$$\nabla \times \vec{E} = -j\omega\mu\vec{H} \tag{62}$$

Here, the magnetic field was normalized according to

$$\tilde{\vec{H}} = -j\eta_0\vec{H}$$

The grid was also normalized according to

$$x' = k_0 x\,,\ y' = k_0 y \text{ and } z' = k_0 z$$

The two curl equations were expanded in Cartesian coordinates

Curl of E

$$\frac{\partial E_z}{\partial y'} - \frac{\partial E_y}{\partial z'} = \mu_{xx}\tilde{H}_x \tag{63}$$

$$\frac{\partial E_x}{\partial z'} - \frac{\partial E_z}{\partial x'} = \mu_{yy}\tilde{H}_y \tag{64}$$

$$\frac{\partial E_y}{\partial x'} - \frac{\partial E_x}{\partial y'} = \mu_{zz}\tilde{H}_z \tag{65}$$

Curl of H

$$\frac{\partial \tilde{H}_z}{\partial y'} - \frac{\partial \tilde{H}_y}{\partial z'} = \varepsilon_{xx}E_x \tag{66}$$

$$\frac{\partial \tilde{H}_x}{\partial z'} - \frac{\partial \tilde{H}_z}{\partial x'} = \varepsilon_{yy}E_y \tag{67}$$

$$\frac{\partial \tilde{H}_y}{\partial x'} - \frac{\partial \tilde{H}_x}{\partial y'} = \varepsilon_{zz}E_z \tag{68}$$

The partial derivative in these equations were then approximated using finite-difference to obtain the following equations.

Curl E

$$\frac{E_z^{i,j+1,k} - E_z^{i,j,k}}{\Delta y'} - \frac{E_y^{i,j,k+1} - E_y^{i,j,k}}{\Delta z'} = \mu_{xx}^{i,j,k}\tilde{H}_x^{i,j,k} \tag{69}$$

$$\frac{E_x^{i,j,k+1} - E_x^{i,j,k}}{\Delta z'} - \frac{E_z^{i+1,j,k} - E_z^{i,j,k}}{\Delta x'} = \mu_{yy}^{i,j,k}\tilde{H}_y^{i,j,k} \tag{70}$$

$$\frac{E_y^{i+1,j,k} - E_x^{i,j,k}}{\Delta x'} - \frac{E_x^{i,j+1,k} - E_x^{i,j,k}}{\Delta y'} = \mu_{zz}^{i,j,k}\tilde{H}_z^{i,j,k} \tag{71}$$

Curl H

$$\frac{\tilde{H}_z^{i,j+1,k} - \tilde{H}_z^{i,j,k}}{\Delta y'} - \frac{\tilde{H}_y^{i,j,k+1} - \tilde{H}_y^{i,j,k}}{\Delta z'} = \varepsilon_{xx}^{i,j,k}E_x^{i,j,k} \tag{72}$$

$$\frac{\tilde{H}_x^{i,j,k+1} - \tilde{H}_x^{i,j,k}}{\Delta z'} - \frac{\tilde{H}_z^{i+1,j,k} - \tilde{H}_z^{i,j,k}}{\Delta x'} = \varepsilon_{yy}^{i,j,k}E_y^{i,j,k} \tag{73}$$

$$\frac{\tilde{H}_y^{i+1,j,k} - \tilde{H}_x^{i,j,k}}{\Delta x'} - \frac{\tilde{H}_x^{i,j+1,k} - \tilde{H}_x^{i,j,k}}{\Delta y'} = \mu_{zz}^{i,j,k}E_z^{i,j,k} \tag{74}$$

For the next part of the FDFD, the fact that any linear operation on a vector can be performed using a square matrix was used. Six derivative matrices were introduced to perform the

derivative operations in Maxwell's equations. D^e_x, D^e_y , D^e_z perform respectively the x, y and z derivatives of the electric fields. D^h_x, D^h_y , D^h_z perform respectively the x, y and z derivatives of the magnetic fields. The bigger the size of the grid, the bigger the derivative matrices will be. They can be become relatively large and required a lot of memory to store. To mitigate this problem, the matrices were stored and manipulated as sparse matrices because they are mainly filled with zeros.

Curl E

$$D^e_y e_z - D^e_z e_y = \mu_{xx} \tilde{h}_x \qquad (75)$$

$$D^e_z e_x - D^e_x e_z = \mu_{yy} \tilde{h}_y \qquad (76)$$

$$D^e_x e_y - D^e_y e_x = \mu_{zz} \tilde{h}_z \qquad (77)$$

Curl H

$$D^h_y \tilde{h}_z - D^h_z \tilde{h}_y = \varepsilon_{xx} e_x \qquad (78)$$

$$D^h_z \tilde{h}_x - D^h_x \tilde{h}_z = \varepsilon_{yy} e_y \qquad (79)$$

$$D^h_x \tilde{h}_y - D^h_y \tilde{h}_x = \varepsilon_{zz} e_z \qquad (80)$$

Implementation of FDFD

Now, that the required equations are found, the next step is to look at the numerical boundary conditions. It can be seen from the curl equations that to find the values the electric and/or magnetic fields inside a cell, their values in adjacent cells are needed. It is easy to see that there will be problem at the boundaries of the grid. To solve this problem, numerical boundary conditions need to be applied.

Three types of boundary condition will be discussed here:

- Dirichlet: The value outside of the grid are set assumed to be 0
- Periodic: The value of the field outside of the grid is the same as the value of field at the other side of the grid.

- Periodic with Bloch's theorem adjustment: It is not the values of the field that are periodic but their amplitude-envelop; therefore, a phase tilt correction is applied to the periodic boundary conditions

Reduction to 2D model

Any physical problem is a 3D problem. Sometimes in particular situations, a 3D problem can be approximated to a 2D or even 1D problem. It was decided to use a 2 D approximation. To be able to simulate the model in 2D, it was assumed that the device was uniform along the z-direction and that the propagation was restricted to the x-y plane.

Leading to:

$$\frac{\partial}{\partial z} = 0 \rightarrow D_z^e = D_z^h = 0$$

Curl E

$$D_y^e e_z = \mu_{xx} \tilde{h}_x \qquad (81)$$

$$-D_x^e e_z = \mu_{yy} \tilde{h}_y \qquad (82)$$

$$D_x^e e_y - D_y^e e_x = \mu_{zz} \tilde{h}_z \qquad (83)$$

Curl H

$$D_y^h \tilde{h}_z = \varepsilon_{xx} e_x \qquad (84)$$

$$-D_x^h \tilde{h}_z = \varepsilon_{yy} e_y \qquad (85)$$

$$D_x^h \tilde{h}_y - D_y^h \tilde{h}_x = \varepsilon_{zz} e_z \qquad (86)$$

Maxwell's equations have decoupled into two distinct modes. The first mode only contains $\tilde{h}_y, \tilde{h}_x \text{ and } e_z$ and it is called the E mode. The second mode only contains $e_y, e_x, \text{and } \tilde{h}_z$, it is the H mode.

E Mode ($\tilde{h}_y, \tilde{h}_x \text{ and } e_z$)

$$D_x^h \tilde{h}_y - D_y^h \tilde{h}_x = \varepsilon_{zz} e_z \qquad (87)$$

$$D_y^e e_z = \mu_{xx} \tilde{h}_x \qquad (88)$$

H Mode ($e_y, e_x, \text{and } \tilde{h}_z$)

$$D_x^e e_y - D_y^e e_x = \mu_{zz} \tilde{h}_z \qquad (90)$$

$$D_y^h \tilde{h}_z = \varepsilon_{xx} e_x \qquad (91)$$

$$-D^{e}_{x'}e_z = \mu_{yy}\tilde{h}_y \qquad (89)$$

$$-D^{h}_{x'}\tilde{h}_z = \varepsilon_{yy}e_y \qquad (92)$$

Matrix wave equations

E Mode

$$\tilde{h}_x = \mu^{-1}_{xx}D^{e}_{y'}e_z$$

Substituting the expression into the first equation gives

$$D^{h}_{x'}(-\mu^{-1}_{yy}D^{e}_{z'}e_z) - D^{h}_{y'}(\mu^{-1}_{xx}D^{e}_{y'}e_z) = \varepsilon_{zz}e_z \qquad A_E e_z = 0$$

$$-D^{h}_{x'}\mu^{-1}_{yy}D^{e}_{z'}e_z - D^{h}_{y'}\mu^{-1}_{xx}D^{e}_{y'}e_z = \varepsilon_{zz}e_z \qquad \text{with } A_E = D^{h}_{x'}\mu^{-1}_{yy}D^{e}_{z'} + D^{h}_{y'}\mu^{-1}_{xx}D^{e}_{y'} + \varepsilon_{zz}$$

$$(D^{h}_{x'}\mu^{-1}_{yy}D^{e}_{z'} + D^{h}_{y'}\mu^{-1}_{xx}D^{e}_{y'} + \varepsilon_{zz})e_z = 0 \qquad (93)$$

Two wave equations

E Mode

$$A_E = D^{h}_{x'}\mu^{-1}_{yy}D^{e}_{z'} + D^{h}_{y'}\mu^{-1}_{xx}D^{e}_{y'} + \varepsilon_{zz} \qquad (94)$$

H Mode

$$A_H = D^{e}_{x'}\varepsilon^{-1}_{yy}D^{h}_{z'} + D^{e}_{y'}\varepsilon^{-1}_{xx}D^{h}_{y'} + \mu_{zz} \qquad (95)$$

Plane wave source

To have a solution of the wave equation that is not zero, a source has to be incorporated.

$$Ae = b$$

The sources used in this dissertation are a plane wave sources. Once the source is put on the grid, the next thing to do is to add an absorbing layer at the edge of the grid so that waves hitting the grid boundary are absorbed and not reflected. The first coming to mind would be to build loss at the boundary of the grid. The problem with this approach is that reflection depends on the extinction coefficient. This dependency is show in the formula from Eq. (96) below

$R = \frac{(1-n)^2 + \kappa^2}{(1+n)^2 + \kappa^2}$ (96), n and κ are the ordinary refractive index and the extinction coefficient

The problem is solved by using anisotropy. The loss is introduced without the reflection. To do so, a uniaxial perfectly matched layer (UPML) is added at the edge of the grid. The UPML is achieved by incorporating a lossy anisotropic material at the edge of the grid. It slowly absorbs any wave incident on it. The reflected portions of the source will be taken between the source and the UPML and the transmitted portions between the object and the UPML. The absorbance was calculated by subtracted the sum of the reflection and the transmission to one.

Now, it is time to simulate. The first step is to construct the device on a grid by assigning values of permittivity to each point in a 2D array representing the device and its surroundings. A representative device on a grid is presented in Figure 50 by ER2. The top part is the PML, then air, followed by the solvent and inside the solvent the material (one nanoparticle was used in this example), air and the PML again. There are also a periodic boundaries conditions on the sides of the grid. The second part is just to show the source and the last part shows what happens to the source when it interacts with the different components inside the grid.

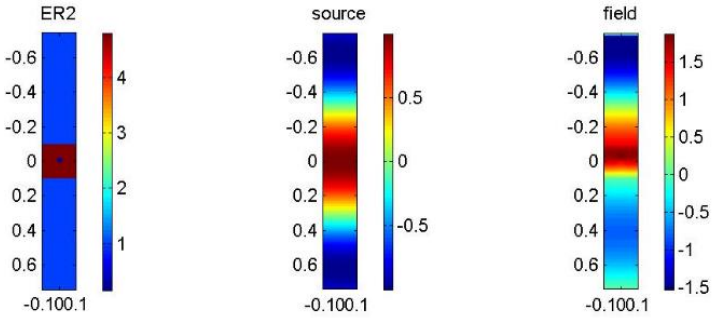

Figure 50: Presentation of the grid, the source and the source inside the field

Simulations with different size of Ag, Au and FeS_2 nanoparticles were performed. The results are respectively presented in Figure 51, Figure 52 and Figure 53.

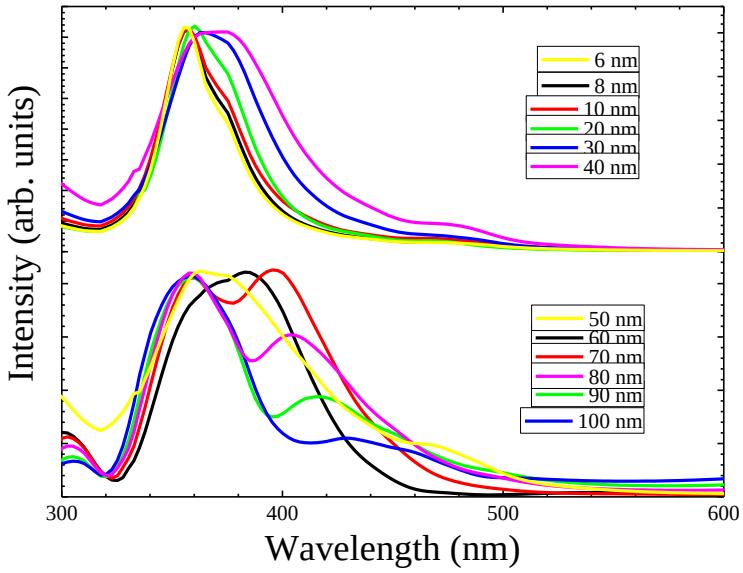

Figure 51: Simulated absorption spectra of different sizes of silver nanoparticles

The different sizes of the spherical metallic nanostructures simulated were 6, 8, 10, 20, 40, 50, 60, 70, 80, 90 and 100 nm. The sizes of the semiconductor nanoparticles simulated were 20, 30, 40 and 50 nm. The optical constants that were necessary for this part were not measured but taken from literature. The refractive index and the extinction coefficient of gold and silver were taken from [116]. The dielectric constant of iron pyrite was taken from [67]

When looking at the results for the absorption spectra of Ag and Au nanoparticles with different sizes, it is easy to see that the plasmonic peak shifts to the right as the size of the nanoparticles increases as it was expected. The peak broadens as the size of the nanoparticles increases. Also, in the case of silver, there is the presence of a second peak, which is attributed to the quadrupole. And as expected the quadrupole peak increases with the increase of the size of the particles. It can also be seen that the shifts of the peak and the position of the peak differ from what was observed in the absorption measured in the lab. This can be due to several things. The first one being the fact that the simulated nanoparticles were spherical, which might not be exactly the

case. The position of plasmonic peaks is related to shape of the particles, this approximation is one of the reasons of the shift in the peak. Another reason is the effect of the ligands. The ligands change the dielectric constant at the surface of the nanoparticle and this change will influence the position of the peak. The last thing is the 2D approximation that was done. There are also many particles with different sizes involved and the interaction between the particles of different sizes plays a role in the shift.

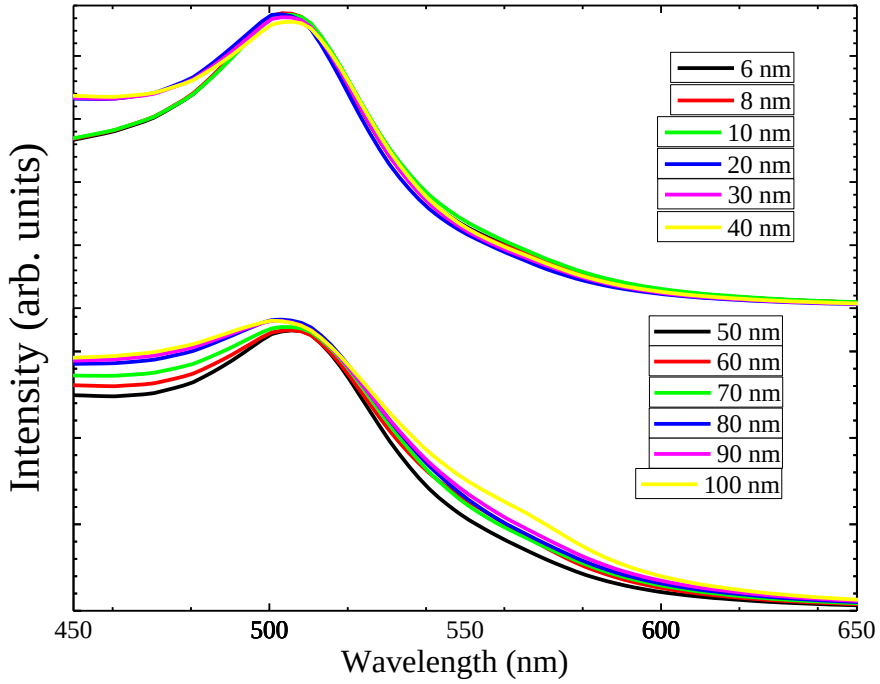

Figure 52: Simulated absorption spectra of different sizes of gold nanoparticles

In the case of the simulation of the absorption spectrum of iron pyrite, the bandgap was obtained around 0.9 eV for the large particle but increases as the size of the particles decreases. The shape of the absorption spectra looks more like the spectra of the smaller 20 nm particle, which is closed to the average size of the particles that was calculated using the Scherrer formula. The difference between the simulated absorption spectra and the measured absorption, just like in the metallic particles case can also come from the shape of the particles, the interaction between

particles, the actions of the ligand and the 2D approximation. The difference in the shape is even more pronounced for the iron pyrite particle. The synthesized Au and Ag particles are almost spherical, while FeS_2 nanoparticles have completely random shapes. Here, the goal is primarily to study the effects on the optical properties of the semiconductor when coupled with metallic nanostructure; therefore, reproducing the exact shape of the particle is only secondary and not necessary.

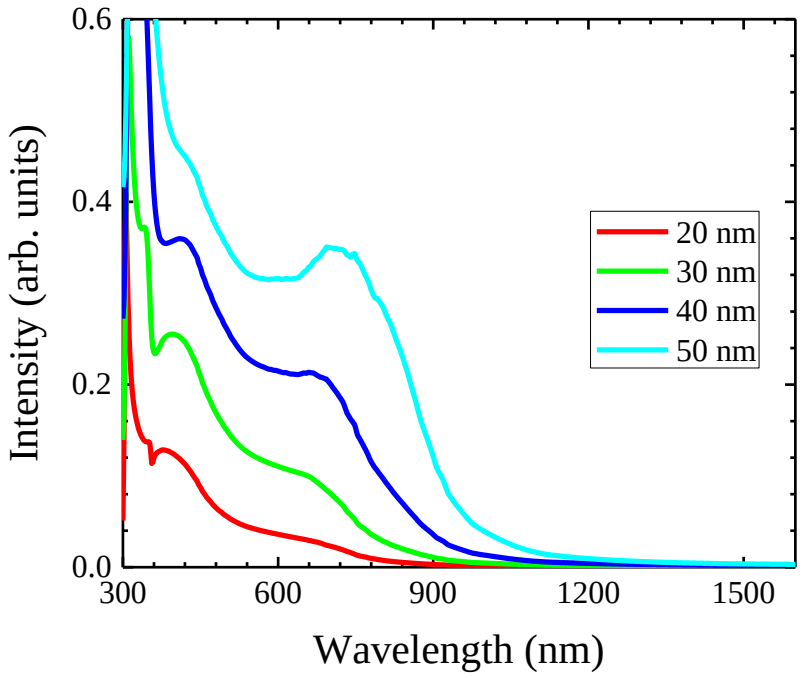

Figure 53: Simulation of the absorption spectra of different sizes of FeS_2 nanoparticle

To study the effects of the metallic nanocrystals, at the surface of the FeS_2 nanoparticles, on the optical properties, it was first decided to look at the effects of metallic shells at the surface of FeS_2 nanoparticles. Ag/Au and Au/Ag core shell were first investigated because of the availability of such examples in the literature [117], [118]. To simulate, it is imperative to make sure that the dielectric constant values of all material exist at the same set of wavelengths. To do

so, origin software was used to extrapolate values of the dielectric constant of Ag, Au and FeS_2 to make them exist at the exact same points. A presentation of the evolution of the shell thickness, while the core stays constant is presented in Figure 54. The left image just show the semiconductor without the shell, the second image shows the semiconductor with a thin metallic shell and the third image show nanoparticles with the thick shell. The size of the shell goes from zero to the radius of the core. The picture was made using the values of the respective dielectric constants at 1650 nm. The change in color of the dielectric constant from the first to the second image comes from the introduction of the metallic particle. The dielectrics from image one stay the same but the color bar changes because of the metal, inducing the color change.

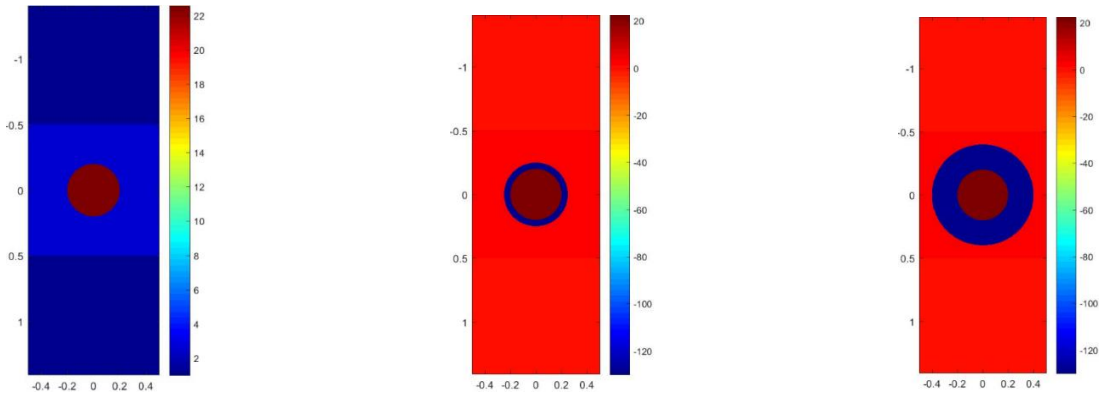

Figure 54: Iron pyrite core with thicknesses of metallic nanostructure shells

It was also investigated if the effective dielectric constant could be used. This was investigated because it could possibly speed up the simulation time if the formula for the effective dielectric works in this case. The formula for the effective dielectric constant is the following

$$\varepsilon_2^{'} = \varepsilon_2 \left\{ \left[\left(\frac{R_1}{R_2} \right)^3 + 2\left(\frac{\varepsilon_3 - \varepsilon_2}{\varepsilon_3 + 2\varepsilon_2} \right) \right] / \left[\left(\frac{R_1}{R_2} \right)^3 - \left(\frac{\varepsilon_3 - \varepsilon_2}{\varepsilon_3 + 2\varepsilon_2} \right) \right] \right\} \text{[119]} \quad (97)$$

The simulations of the Ag/Au and Au/Ag core shells and their effective refractive index are presented in Figure 55 and Figure 56. For these simulations, the core had a radius of 20 nm and the shell was varied from 0 to 18 nm by increments of 2 nm.

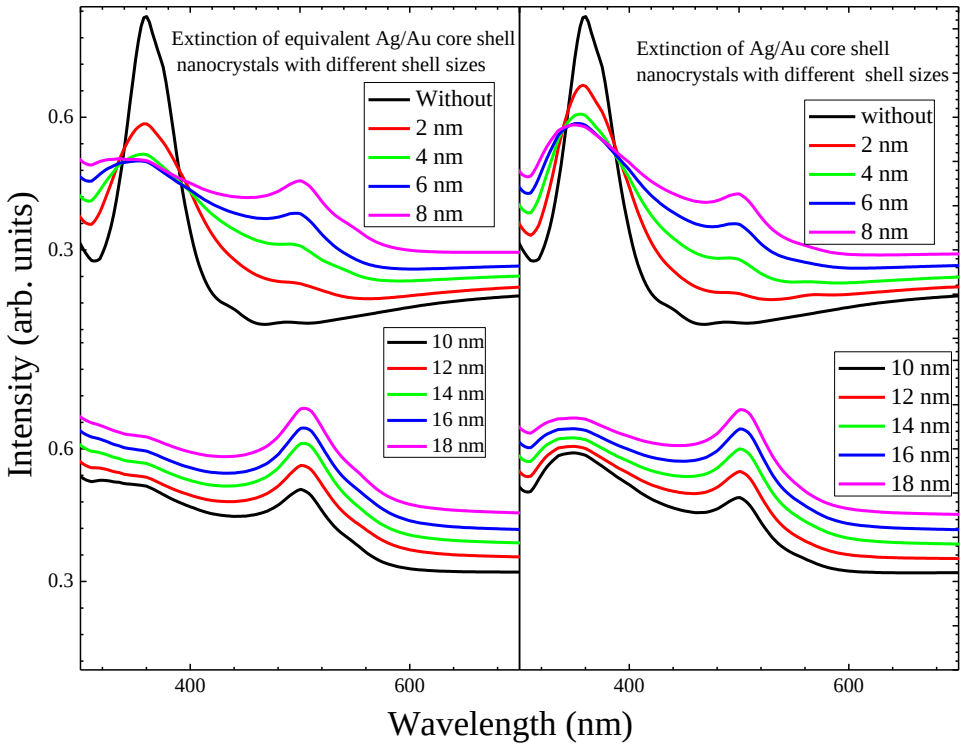

Figure 55: Simulated absorption spectra of Ag/Au core shell nanoparticles and their equivalent particles. The size of the Ag particle is 40 nm.

In the case of Ag/Au and Au/Ag core shell, the plasmonic peak of the shell gradually grows with the increase of the shell thickness; while the plasmonic of the core decreases as the size of the shell increase, to finish by eventually disappearing. This can be related to the results from the first part of this chapter. The plasmonic peak of the small gold nanostructure was not observed in the absorption spectra of FeS_2/Au nanoparticles, while the plasmonic peak of the big silver nanostructure was somehow responsible for the increase in the absorption spectra of FeS_2/Ag nanoparticles. There is a slight difference between the Ag/Au core shell and the Au/Ag core shell,

it takes more time for the peak of the core to disappear in the Au/Ag core shell case. This could be because the plasmonic peak of silver is mainly due to scattering, while the peak of gold is due to absorption. The shell might scatter a small portion of the light in the direction of the core. The effect of the surrounding refractive index on the position of the plasmonic peak can also be seen in the results.

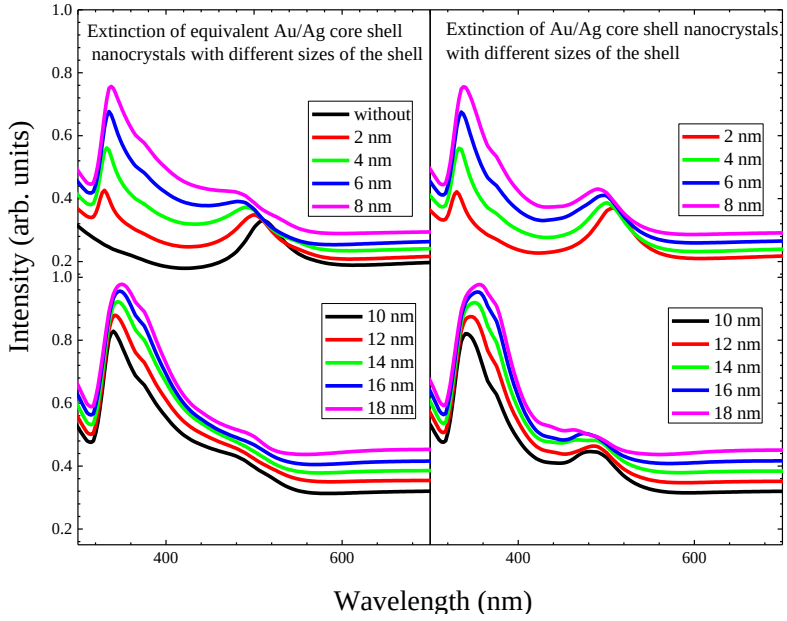

Figure 56: Simulated absorption spectra of Au/Ag core shell nanoparticles and their equivalent particles. The size of the Au particle is 20 nm

The position of the plasmonic peak silver in the Au/Ag core shell shifts and broaden as the silver shell is increased. When using the effective refractive index, the decrease of the plasmonic peak of the core is happening slower than in the normal core/shell configuration. This happened because, at this resonance wavelengths, the metal is not pure anymore but a hybrid composed of the original metal and a portion of the second metal; therefore, the strength of the resonance is decreased. For small thicknesses of the shell the effect of the effective refractive index matches

the effect of the original core/shell. This allows the possible use of the effective refractive index for the simulation of the actual nanoparticle as the shell is thin in that case.

After the simulations of Ag/Au and Au/Ag core shells and their effective refractive index, and seeing that the results are similar to experimental results in literature, it was time to do the simulations of the FeS_2/Au and FeS_2/Ag core/shells nanoparticles and their effective refractive index. The results of the simulations are presenting in Figure 57 and Figure 58.

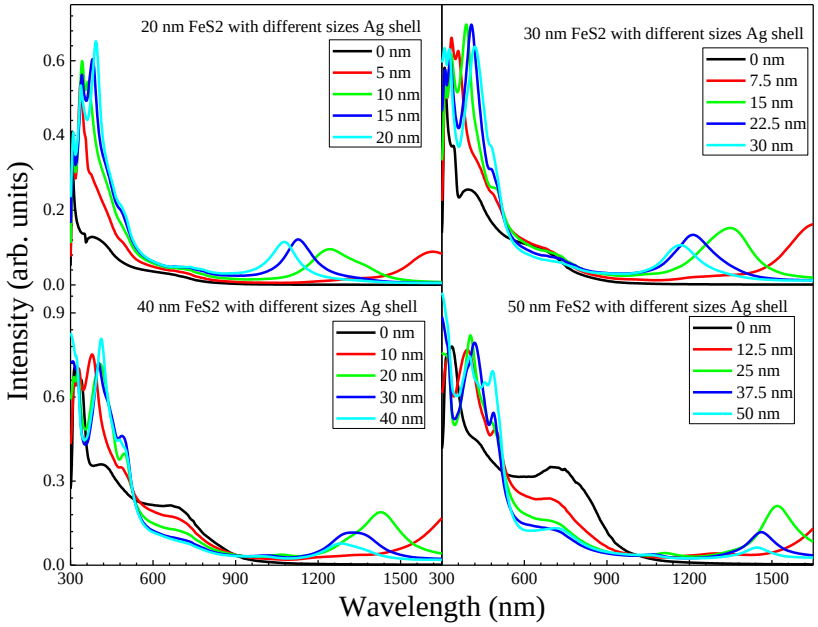

Figure 57: Simulated absorption spectra of FeS_2/Ag core shell nanoparticles. The size of the FeS_2 particles varies from 20 to 50 nm by 10 nm increments

In this case, the radius of the semiconductor changed from 20 to 50 nm with 10 nm increments. The thickness of the shell was varied from 0 to radius of the shell by increments of quarter of the radius. For the simulation of the semiconductor/metal core shell, just like in the experiment, toluene was used instead of chloroform leading to a small difference in the two spectra of the iron pyrite nanoparticles. In the FeS_2/Ag and FeS_2/Au just like for Ag and Au core shell, as

the thickness of the shell increases the spectrum starts looking more and more like the spectrum of the shell and less and less like the spectrum of the core. The noticeable difference between the metal/metal core shell and the semiconductor/shell is the feature in the near infrared (NIR) region.

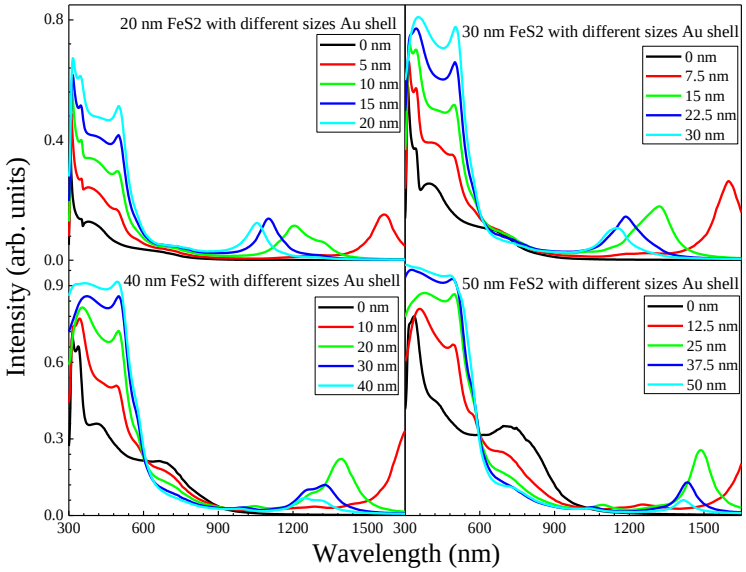

Figure 58: Simulated absorption spectra of FeS_2/Au core shell nanoparticles. The size of the FeS_2 particle varies from 20 to 50 nm by 10 nm increments

This feature appears with both silver and gold shell. The feature shifts to the left as the thickness of the shell increases. This peak is associated with the plasmonic peak of FeS_2. The position of the plasmonic peak of semiconductor just like the plasmonic peak of metal is affected by the dielectric constant of the surrounding. The shift is more pronounced than the shift of in the case of the metal. This is because semiconductor have less free electrons than metal. Plasmonic is a collective phenomenon of electrons; therefore, a perturbation of the surrounding will affect more the collective with less electrons. As the thickness of the shell increases the shift become less and less important.

The simulations of the emission of the particles proved to be quiet challenging, it was therefore decided to study, the ratio of the absorption before and after the shell and try to correlate it to an increase or a decrease in the emission of the semiconductor nanoparticle. The results of the absorption spectra ratios of the semiconductor/metal core/shell nanoparticles are presented in Figure 59 and Figure 60.

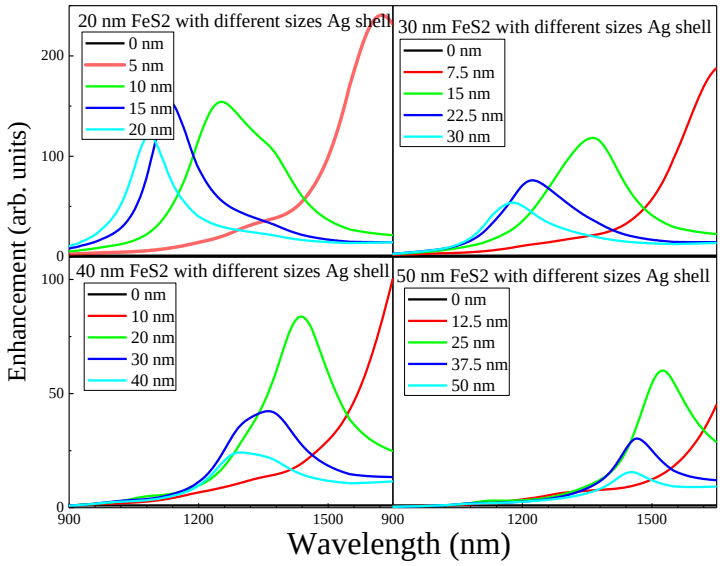

Figure 59: Absorption Enhancement of different size FeS_2 nanoparticles with Ag shell

The plasmonic peak of the iron pyrite is multiplied by 240 for the 20 nm iron pyrite nanoparticle when a silver shell of 5 nm. It is respectively multiplied by 150, 150 and 120, when the shell thicknesses are 10 nm, 15 nm and 20 nm. The plasmonic peak of the iron pyrite is multiplied by 390 for the 20 nm iron pyrite nanoparticle when a gold shell of 5 nm. It is respectively multiplied by 170, 160 and 115, when the shell thicknesses are 10 nm, 15 nm and 20 nm. For same size of the core and same thickness of the shell there was a right shift of the semiconductor plasmonic peak when gold was replaced by silver. The plasmonic peak shift right when the size of the semiconductor is increased but shift left when the thickness of the

core is increased. The plasmonic peak of the semiconductor is in the IR region above the wavelength of the first direct bandgap. Therefore, it is not going to affect the photoluminescence. Only the enhancement that happens before the direct bandgap can affect the luminescence.

The enhancement varied between 2 and 4 for the 20 nm core and the silver shell. The enhancement varied between 3 and 9 for the same size of the core but with gold instead of silver. Here, the enhancement increases with the increase of the thickness of the shell. This agrees with the hypothesis that the strength of the PL follows the same trend than the size of the shell. The PL not having a one to one relation with the absorption, the increase of the absorption will not be the same as the increase of the PL. On top of that, the effect of the coupling should also be considered; therefore, it is only passed a certain shell thickness threshold that the PL will start to increase, like it was observed in the experimental part.

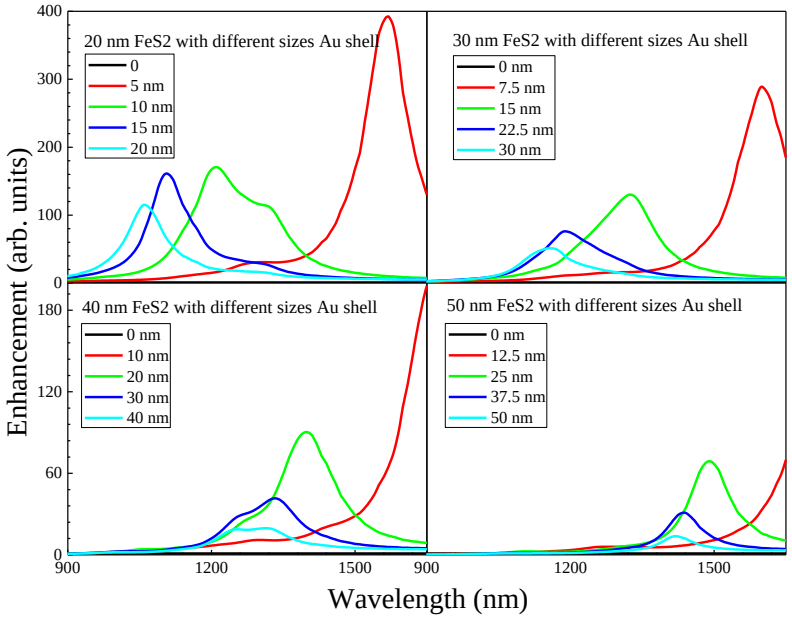

Figure 60: Absorption Enhancement of different size FeS_2 nanoparticles with Au shells

There is just a small problem with the core/shell model. The nanocrystals at the surface of the semiconductor are not forming a shell, but instead they are randomly arranged at the surface of the semiconductor just like it is the case in [120]. To simulate this, the size of a metallic nanostructure at the surface of the semiconductor will varies and the changed of the absorption was studied. The size change of the metallic nanostructure is presented in Figure 61

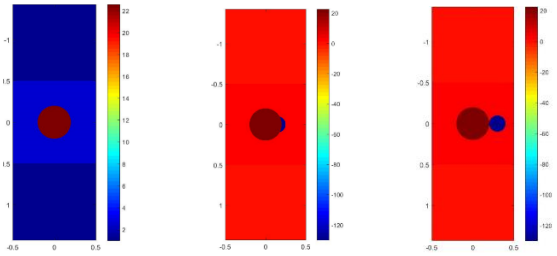

Figure 61: Iron pyrite nanoparticles with metallic nanostructure centers at different points

The results of the simulations are presented in Figure 62 and Figure 63 for the silver and gold. For the simulation, the size of the core was again varied from 20 to 50 nm. The radius of the metallic nanostructure was half of the radius of the semiconductor. The metallic nanostructure was centered at different points away from the center of the semiconductor nanoparticle in the x axis. The different positions were varied from the radius of the metal to the sum of the two radii by increments of the quarter of the radius of the semiconductor. The metallic nanostructure was placed on the grid first and the semiconductor second. Therefore, if there was an intersection, the place would have the value of the dielectric of the semiconductor, just like it can be seen from the first image of Figure 61.

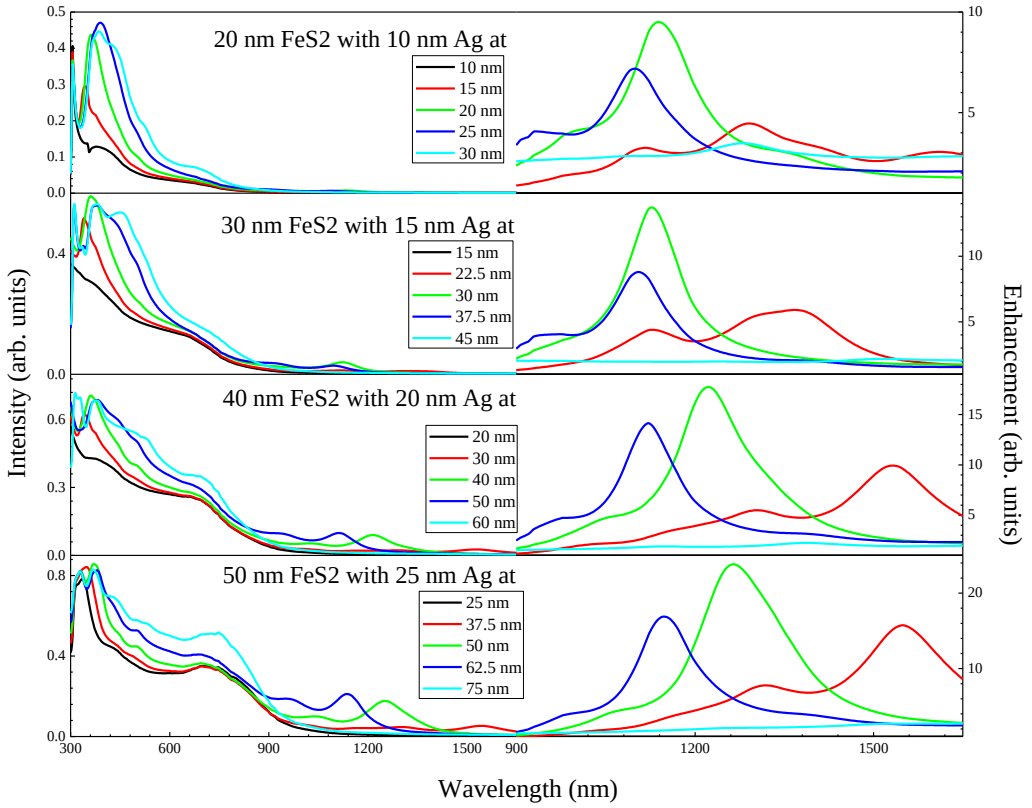

Figure 62: Absorption and enhancement spectra of FeS_2 nanoparticles with Ag

When looking at the results, there are some similarities and some differences with the results with the core shell model. Just like in semiconductor, the plasmonic peak of the semiconductor is present in the IR region and the peak shift to the left as the metallic structure moves to the right. This is again in agreement with the effect of the dielectric constant of the surrounding on the position of the peak. As the particles shifts right, the dielectric constant of the medium is more and more perturbed affecting differently the semiconductor. The enhancement is lower than the enhancement of the core shell. In the core shell, there is a bigger interface between the metal and the semiconductor. When metal located at three quarters of the radius of the semiconductor there are more than 2 peaks. For 20 nm particles, there are three peaks and one

shoulder. For 30 nm, there are two peaks and one shoulder and for 40 and 50 nm, there are two peaks. These peaks are probably higher modes of the resonance of the semiconductor.

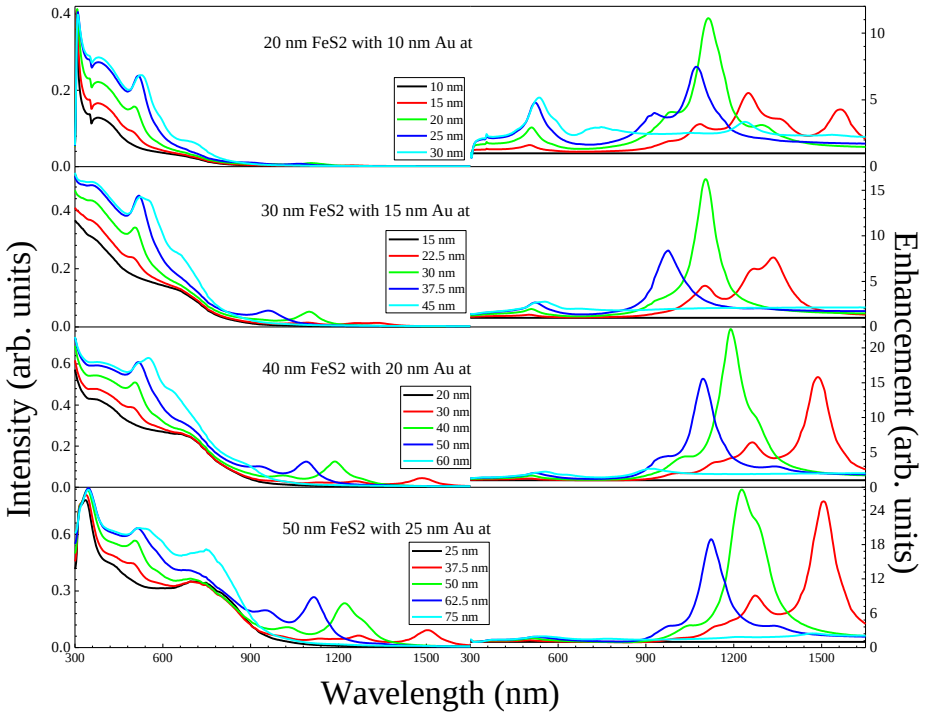

Figure 63: Absorption and enhancement spectra of FeS_2 nanoparticle with Au

The second peak becomes more of a shoulder as the metal moves away from the semiconductor. When the metal is located at three times the radius of metallic nanostructure, there is no more peak, the enhancement flattens. Contrary to the core shell, the shoulder feature presents in the absorption spectrum of the iron pyrite nanoparticle does not flatten but become even more pronounce as the metal moves to the right. In the core/shell case, the metal was absorbing or scattering the light before it reaches the semiconductor, reducing the amount of light the semiconductor could absorbed; therefore, resulting in the decrease in intensity of the shoulder feature. Here, there is more light going to the semiconductor because of scattering of the light from the Au or Ag

Iron pyrite nanoparticles were successfully coupled with metallic gold and silver nanostructures. The absorption spectra of the coupled nanoparticles did show little traces of the

metallic nanostructures, because of the small size of the gold or silver particles. A change was present in the photoluminescence spectra, where the particle with gold showed a reduction of emission. Some of the particles coupled with silver showed a decrease while the rest showed an increase. The nanostructures introduced trap states inside the bandgap of the iron pyrite and the metal needed to be big enough to overcome the effect of the traps with its plasmonic effect. The coupled nanoparticles were simulated using finite difference frequency domain and the results matched the experimental results. The simulations also showed an absorption in the IR region that was accredited to the plasmonic effect of this time the semiconductor. This absorption was not present in the experiment because of the size of the metal. When small nanoparticle sizes were used in the simulation this peak was weak.

CHAPTER 7: CONCLUSION

Iron pyrite nanoparticles were successfully synthesized using a hot injection method. The nanoparticles were characterized to ensure that the right phase was synthesized and to make sure that neither marcasite nor any other iron to sulfur ratio materials were synthesized along with pyrite. Characterization, XRD and Raman spectroscopy confirmed that the nanoparticles were pure pyrite. The ligands used during the synthesis were amines, either oleylamine or hexadecylamine. To passivate the surface of the particles and improve their stability, the native organic ligands were replaced by inorganic ligands. The ligands chosen were Sb, Fe and $(NH_4)_2S$. The ligand exchange was done using a bi-phase process between chloroform and formamide. The ligand exchange was confirmed using FTIR spectroscopy, because of the disappearance of the amine peak in the spectrum of the particles after the exchange. Characterization was again done to confirm that there was no pyrite phase change after the exchange. Two stabilities were studies, the long-term air stability and the stability to relatively high temperature.

To study the temperature stability, iron pyrite thin films were made by depositing the particles on a substrate of molybdenum deposited on soda lime glass using spray pyrolysis. The deposition temperatures were 300˚C, 250˚ C and 200˚C. Characterizations were once again done to verify the stability after deposition. The XRD and Raman measurement show that the nanoparticles stay pyrite. Some shift in the peak in the Raman spectra were noticed. These shifts were due to the ligand at the surface of the particles that affect the vibrational mode of the atoms in the FeS_2 crystal. For the air stability, the thin films and the nanoparticles were stored in atmosphere for one year and they were characterized before and after storing to study the difference. For this part, the particles were place in a different solvent than the solvent used for the thin film deposition. The solvent used for the deposition was dimethylformamide, this solvent was

chosen because of its high boiling point, but DMF was attacking the surface of the particles and their stability was greatly degraded. The solvent was replaced by ethanol. After 1 year, the phase of nanoparticle in solution and the films did not change. Solar cell of the particles were also made but the performances were poor, they did not exhibited any photovoltaic behavior. This was due to effect of ligands introducing trap states inside the band gap of the material, creating an almost metallic layer at the surface of the pyrite and the films. The absorption coefficient of pyrite being really high, most of its absorption happen at the surface; therefore as long as this problem is not fixed it will be difficult to make high efficiency iron pyrite solar cells.

The high conductivity of the film might have been detrimental for solar cell application but was interesting for another renewable energy application, mainly thermoelectric. The thermoelectric properties of the iron pyrite nanoparticles were investigated. First, the properties of the particles before ligand exchange was measured and/or calculated. The ZT power of the particles was low and the seebeck coefficient of the particles was positive, making the particles p-type. Then, the ligands of the particles were exchanged and the thermoelectric was measured, the electrical properties were improved by an order of magnitude, while the seebeck remained in the same range. The ZT was in the order of 10^{-3}. For state of the art thermoelectric material and even for iron pyrite this number was low. To further improve the ZT, iron pyrite was successfully doped by cobalt using a 2 steps hot injection method. Cobalt doped iron pyrite nanoparticles were successfully synthesized with the molar fraction of the dopant going from 0 to 20%. The ZT of the $Fe_{0.8}Co_{0.2}S_2$ nanoparticles was in the order of 10^{-1}. That is a 2 order of magnitude increase from the undoped iron pyrite after ligand exchange and one order of magnitude increase from the previous record of iron pyrite ZT. This increase was obviously attributed to the increase in charge carriers and the change in the type of conduction of the nanoparticles from p to n type. The electron

mobility in iron pyrite being two order of magnitude higher than its counterpart carrier. After the successful enhancement of the electrical properties of iron pyrite, the next step was to improve its optical properties.

To improve the optical properties of the iron pyrite nanoparticles, the particles were coupled with metallic particles of Au and Ag. First, the gold nanocrystals were successfully synthesized and their UV-Vis was measured to confirm; then the FeS_2 nanoparticles were synthesized, but for this part instead of chloroform as the solvent, toluene was used instead. Toluene was used to have the particles and the metallic in the same solvent. For the doping, the Au solution was added drop wise in the iron pyrite solution. The UV-Vis was again done after the coupling but no significant difference was noticed between the spectra before and after. It was speculated that the particle was too small to have an influence in the spectra of the combined particles. The PL spectroscopy of the combined particles was measure and compared with the spectrum of the particles before coupling. The PL saw an important decrease after the coupling. There could be an electron transfer between the iron pyrite and Au, but the conflicted values of the vacuum level of the iron pyrite did not allow a more affirmative answer. For synthesis of FeS_2/Ag two methods were used. The first method was done by galvanic replacement of gold in the FeS_2/Au nanoparticles by silver. For the second method after the synthesis of iron pyrite nanoparticles, silver precursor was introduced in the reactor to growth the metallic structure at the surface of the semiconductor. The absorption spectra of the coupled showed little difference from the uncoupled particles. The silver structure growth in the reactor with iron pyrite saw an increase, while the rest saw a decrease. The reason is thought to be that the metallic nanostructures were bigger and the enhancement in the absorption of the iron pyrite nanoparticles, cause by the strong scattering on light, overcame the traps that could have been introduced in the band gap.

Simulations of nanoparticles were done, to see, if the results could be reproduced by simulation. The simulation method used was finite difference frequency domain (FDFD). This method was used because of its ease to use and implement. The absorption spectra of Au, Ag and iron pyrite nanoparticles were simulated. The results were a little bit different to the experimental values but the trend seen in the simulations is in agreement with the results observed during the experiments. This was due, to the different approximations that were done during the simulation. Different core shells, Au/Ag, Ag/Au, FeS_2/Au and FeS_2/Ag were also simulated. Two things were taken from these simulations. First, for thin core shell, both peaks are visible but as the shell increases, the peak of the core eventually disappears. The second thing is the plasmonic peak of iron pyrite is in the infrared region. The plasmonic position of the peak could be tuned by changing the thickness of the shell.

OUTLOOK

As previously mentioned more work needs to be done before having high efficiency iron pyrite solar cells. The most important thing is to solve the surface detects, which combined with the high absorption coefficient of the materials make it detrimental for the efficiency of the cells. The culprit of the surface defect needs to be further investigated. Investigation of more ligands for surface passivation should as well be carried out.

The synthesis of cobalt doped iron pyrite should be improved, to have more monodispersed nanoparticles. More synthesis temperatures should also be investigated. Ligand exchange/displacement effects on the electrical properties of the doped nanoparticles needs to be studied, the doped particles used in this did not undergo ligand exchange. The ratio of Co to Fe ration should be increased and its effect on the electrical and thermal conductivities should be investigated.

The size of the metallic nanostructures attached to the iron pyrite nanoparticles should be increased and the effect of the size increase on the absorption spectrum should be studied. Experiments should be done to reproduce the plasmonic peak observed in the simulations. If confirmed by experiment, iron pyrite plasmonic peak could be used in biomedical and in infrared photodetectors. A shell should be approximated using the Maxwell-Garnett effective media formula, where the metallic nanocrystals will be considered to be randomly dispersed in the solvent for a more accurate simulation. The material with such a dielectric constant will then be used as shell with FeS_2 as a core. For the effects on the intensity of the photoluminescence, investigation of the implementation of the Purcell factor without using the Lumerica software, FDTD should be carried out. 3D simulation should be carried out. Simulation using FDTD and finite element method (FEM) should also be done and compared with the results from FDFD.

REFERENCES

[1] Panasonic, *Solar Cells Technical handbook*. 1999.

[2] D. Butler, "Thin films: ready for their close-up?," *Nature*, vol. 454, no. 7204, pp. 558–9, Jul. 2008.

[3] M. A. Green, K. Emery, Y. Hishikawa, W. Warta, and E. D. Dunlop, "Solar cell efficiency tables (version 40)," *Prog. Photovoltaics Res. Appl.*, vol. 20, no. 5, pp. 606–614, Aug. 2012.

[4] K. L. Chopra, P. D. Paulson, and V. Dutta, "Thin-film solar cells: an overview," *Prog. Photovoltaics Res. Appl.*, vol. 12, no. 23, pp. 69–92, Mar. 2004.

[5] F. Solar, "CdTe solar cells record," 2011. [Online]. Available: http://investor.firstsolar.com/releasedetail.cfm?ReleaseID=593994.

[6] B. Metin *et al.*, "Electroplating Based CIGS Technology for Roll-to-Roll Manufacturing," *23rd Eur. Photovolt. Sol. Energy Conf. Exhib. 1-5 Sept. 2008, Val. Spain*, no. 1–5 September, pp. 2137–2141, Nov. 2008.

[7] S. Aksu, J. Wang, and B. M. Basol, "Electrodeposition of In–Se and Ga–Se Thin Films for Preparation of CIGS Solar Cells," *Electrochem. Solid-State Lett.*, vol. 12, no. 5, p. D33, May 2009.

[8] M. Bär, I. Repins, M. A. Contreras, L. Weinhardt, R. Noufi, and C. Heske, "Chemical and electronic surface structure of 20%-efficient Cu(In,Ga)Se2 thin film solar cell absorbers," *Appl. Phys. Lett.*, vol. 95, no. 5, p. 52106, Aug. 2009.

[9] T. K. Todorov *et al.*, "Beyond 11% Efficiency: Characteristics of State-of-the-Art Cu 2 ZnSn(S,Se) 4 Solar Cells," *Adv. Energy Mater.*, vol. 3, no. 1, pp. 34–38, Jan. 2013.

[10] T. K. Todorov, K. B. Reuter, and D. B. Mitzi, "High-efficiency solar cell with Earth-abundant liquid-processed absorber.," *Adv. Mater.*, vol. 22, no. 20, pp. E156-9, May 2010.

[11] Y.-H. Tak, K.-B. Kim, H.-G. Park, K.-H. Lee, and J.-R. Lee, "Criteria for ITO (indium–tin-oxide) thin film as the bottom electrode of an organic light emitting diode," *Thin Solid Films*, vol. 411, no. 1, pp. 12–16, May 2002.

[12] T. Moriga, D. R. Kammler, T. O. Mason, G. B. Palmer, and K. R. Poeppelmeier, "Electrical and Optical Properties of Transparent Conducting Homologous Compounds in the Indium-Gallium-Zinc Oxide System," *J. Am. Ceram. Soc.*, vol. 82, no. 10, pp. 2705–2710, Dec. 2004.

[13] D. B. Mitzi *et al.*, "Torwards marketable efficiency solution-processed kesterite and chalcopyrite photovoltaic devices," *2010 35th IEEE Photovolt. Spec. Conf.*, pp. 000640–

000645, Jun. 2010.

[14] S. Seefeld *et al.*, “Iron pyrite thin films synthesized from an Fe(acac)3 ink.,” *J. Am. Chem. Soc.*, vol. 135, no. 11, pp. 4412–24, Mar. 2013.

[15] A. Ennaoui, S. Fiechter, H. Goslowsky, and H. Tributsch, “Photoactive Synthetic Polycrystalline Pyrite (FeS),” *J. Electrochem. Soc. Electrochem. Sci. Technol.*, pp. 1579–1582, 1985.

[16] M. Gong, A. Kirkeminde, and S. Ren, “Symmetry-defying iron pyrite (FeS_2) nanocrystals through oriented attachment.,” *Sci. Rep.*, vol. 3, p. 2092, Jan. 2013.

[17] Y. Bi, Y. Yuan, C. L. Exstrom, S. A. Darveau, and J. Huang, “Air stable, photosensitive, phase pure iron pyrite nanocrystal thin films for photovoltaic application.,” *Nano Lett.*, vol. 11, no. 11, pp. 4953–7, Nov. 2011.

[18] S. C. Mangham, M. Alam Khan, M. Benamara, and M. O. Manasreh, “Synthesis of iron pyrite nanocrystals utilizing trioctylphosphine oxide (TOPO) for photovoltaic devices,” *Mater. Lett.*, vol. 97, pp. 144–147, Apr. 2013.

[19] M. G. Panthani and B. A. Korgel, “Nanocrystals for electronics.,” *Annu. Rev. Chem. Biomol. Eng.*, vol. 3, pp. 287–311, Jan. 2012.

[20] A. Shah, “Photovoltaic Technology: The Case for Thin-Film Solar Cells,” *Science (80-.).*, vol. 285, no. 5428, pp. 692–698, Jul. 1999.

[21] G. E. Jellison, “Optical absorption coefficient of silicon at 1.152 μ at elevated temperatures,” *Appl. Phys. Lett.*, vol. 41, no. 7, p. 594, Oct. 1982.

[22] A. Slaoui and R. T. Collins, “Advanced Inorganic Materials for Photovoltaics,” *MRS Bull.*, vol. 32, no. 3, pp. 211–218, Jan. 2011.

[23] A. Chirilă *et al.*, “Highly efficient Cu(In,Ga)Se2 solar cells grown on flexible polymer films.,” *Nat. Mater.*, vol. 10, no. 11, pp. 857–61, Nov. 2011.

[24] K. Orgassa, H. W. Schock, and J. H. Werner, “Alternative back contact materials for thin film Cu(In,Ga)Se2 solar cells,” *Thin Solid Films*, vol. 431–432, pp. 387–391, May 2003.

[25] M. W. Wang, “Novel CdSe-based PV structure for high efficiency CdSe/CIGS tandem solar cells,” *2009 34th IEEE Photovolt. Spec. Conf.*, pp. 000489–000493, Jun. 2009.

[26] L. Kranz *et al.*, “Doping of polycrystalline CdTe for high-efficiency solar cells on flexible metal foil.,” *Nat. Commun.*, vol. 4, p. 2306, Jan. 2013.

[27] M. G. Panthani *et al.*, “High efficiency solution processed sintered CdTe nanocrystal solar cells: the role of interfaces.,” *Nano Lett.*, vol. 14, no. 2, pp. 670–5, Feb. 2014.

[28] B. M. Basol *et al.*, “Status of electroplating based CIGS technology development,” in *2009 34th IEEE Photovoltaic Specialists Conference (PVSC)*, 2009, pp. 002310–002315.

[29] C. B. Vining, “An inconvenient truth about thermoelectrics.,” *Nat. Mater.*, vol. 8, no. 2, pp. 83–5, Feb. 2009.

[30] D. M. Rowe, *Thermoelectrics Handbook: Macro to Nano*. CRC Press, 2005.
[31] H. J. Goldsmid, *Thermoelectric refrigeration*. Plenum Press, 1964.
[32] D. K. C. MacDonald, *Thermoelectricity: An Introduction to the Principles*. Courier Corporation, 2013.

[33] A. Shakouri, “Recent Developments in Semiconductor Thermoelectric Physics and Materials,” Jul. 2011.

[34] H. J. Goldsmid, *Introduction to thermoelectricity*. Heidelberg ; Springer, 2010.
[35] J. R. Szczech, J. M. Higgins, and S. Jin, “Enhancement of the thermoelectric properties in nanoscale and nanostructured materials,” *J. Mater. Chem.*, vol. 21, no. 12, p. 4037, 2011.

[36] M. Zebarjadi *et al.*, “Power factor enhancement by modulation doping in bulk nanocomposites.,” *Nano Lett.*, vol. 11, no. 6, pp. 2225–30, Jun. 2011.

[37] M. Zebarjadi, B. Liao, K. Esfarjani, M. Dresselhaus, and G. Chen, “Enhancing the thermoelectric power factor by using invisible dopants.,” *Adv. Mater.*, vol. 25, no. 11, pp. 1577–82, Mar. 2013.

[38] N. Mingo, “Thermoelectric figure of merit and maximum power factor in III–V semiconductor nanowires,” *Appl. Phys. Lett.*, vol. 84, no. 14, p. 2652, Apr. 2004.

[39] Z. Tian, S. Lee, and G. Chen, “Heat Transfer in Thermoelectric Materials and Devices,” *J. Heat Transfer*, vol. 135, no. 6, p. 61605, May 2013.

[40] R. Franz and G. Wiedemann, “Ueber die Wärme-Leitungsfähigkeit der Metalle,” *Ann. der Phys. und Chemie*, vol. 165, no. 8, pp. 497–531, 1853.

[41] A. J. Minnich, M. S. Dresselhaus, Z. F. Ren, and G. Chen, “Bulk nanostructured thermoelectric materials: current research and future prospects,” *Energy Environ. Sci.*, vol. 2, no. 5, p. 466, May 2009.

[42] M. Christensen *et al.*, “Avoided crossing of rattler modes in thermoelectric materials.,” *Nat. Mater.*, vol. 7, no. 10, pp. 811–5, Oct. 2008.
[43] C. J. Vineis *et al.*, “Carrier concentration and temperature dependence of the electronic transport properties of epitaxial PbTe and PbTe/PbSe nanodot superlattices,” *Phys. Rev. B*, vol. 77, no. 23, p. 235202, Jun. 2008.

[44] H. Ikeda and F. Salleh, “Influence of heavy doping on Seebeck coefficient in silicon-on-

insulator," *Appl. Phys. Lett.*, vol. 96, no. 1, p. 12106, Jan. 2010.

[45] D. Vashaee and A. Shakouri, "Improved thermoelectric power factor in metal-based superlattices.," *Phys. Rev. Lett.*, vol. 92, no. 10, p. 106103, Mar. 2004.

[46] W. Liu, X. Yan, G. Chen, and Z. Ren, "Recent advances in thermoelectric nanocomposites," *Nano Energy*, vol. 1, no. 1, pp. 42–56, Jan. 2012.

[47] H. Alam and S. Ramakrishna, "A review on the enhancement of figure of merit from bulk to nano-thermoelectric materials," *Nano Energy*, vol. 2, no. 2, pp. 190–212, Mar. 2013.

[48] K. Nielsch, J. Bachmann, J. Kimling, and H. Böttner, "Thermoelectric Nanostructures: From Physical Model Systems towards Nanograined Composites," *Adv. Energy Mater.*, vol. 1, no. 5, pp. 713–731, Oct. 2011.

[49] P. Vaqueiro and A. V. Powell, "Recent developments in nanostructured materials for high-performance thermoelectrics," *J. Mater. Chem.*, vol. 20, no. 43, p. 9577, Nov. 2010.

[50] M. G. Kanatzidis, "Nanostructured Thermoelectrics: The New Paradigm? †," *Chem. Mater.*, vol. 22, no. 3, pp. 648–659, Feb. 2010.

[51] G. Mahan, B. Sales, and J. Sharp, "Thermoelectric Materials: New Approaches to an Old Problem," *Phys. Today*, vol. 50, no. 3, p. 42, Jan. 1997.

[52] M. A. Green and M. J. Keevers, "Optical properties of intrinsic silicon at 300 K," *Prog. Photovoltaics Res. Appl.*, vol. 3, no. 3, pp. 189–192, 1995.

[53] J. Geist, A. Migdall, and H. P. Baltes, "Analytic representation of the silicon absorption coefficient in the indirect transition region.," *Appl. Opt.*, vol. 27, no. 18, pp. 3777–9, Sep. 1988.

[54] J. SEOL, S. LEE, J. LEE, H. NAM, and K. KIM, "Electrical and optical properties of CuZnSnS thin films prepared by rf magnetron sputtering process," *Sol. Energy Mater. Sol. Cells*, vol. 75, no. 1–2, pp. 155–162, Jan. 2003.

[55] H. Katagiri, N. Sasaguchi, S. Hando, S. Hoshino, J. Ohashi, and T. Yokota, "Preparation and evaluation of Cu2ZnSnS4 thin films by sulfurization of E□B evaporated precursors," *Sol. Energy Mater. Sol. Cells*, vol. 49, no. 1–4, pp. 407–414, Dec. 1997.

[56] W. W. Yu, L. Qu, W. Guo, and X. Peng, "Experimental Determination of the Extinction Coefficient of CdTe, CdSe, and CdS Nanocrystals," *Chem. Mater.*, vol. 15, no. 14, pp. 2854–2860, Jul. 2003.

[57] K. Mitchell, A. L. Fahrenbruch, and R. H. Bube, "Photovoltaic determination of optical-absorption coefficient in CdTe," *J. Appl. Phys.*, vol. 48, no. 2, p. 829, Aug. 1977.

[58] H. Vogt, T. Chattopadhyay, and H. J. Stolz, "Complete first-order Raman spectra of the

pyrite structure compounds FeS_2, MnS_2 AND SiP_2," *J. Phys. Chem. Solids*, vol. 44, no. 9, pp. 869–873, Jan. 1983.

[59] W. Paszkowicz and J. A. Leiro, "Rietveld refinement study of pyrite crystals," *J. Alloys Compd.*, vol. 401, no. 1–2, pp. 289–295, Sep. 2005.

[60] J. L. Verble and R. F. Wallis, "Infrared Studies of Lattice Vibrations in Iron Pyrite," *Phys. Rev.*, vol. 182, no. 3, pp. 783–789, Jun. 1969.

[61] K. Prince, M. Matteucci, K. Kuepper, S. Chiuzbaian, S. Bartkowski, and M. Neumann, "Core-level spectroscopic study of FeO and FeS_2," *Phys. Rev. B*, vol. 71, no. 8, p. 85102, Feb. 2005.

[62] W. L. Bragg, "The Analysis of Crystals by the X-ray Spectrometer," *Proc. R. Soc. London. Ser. A, Contain. Pap. a Math. Phys. Character*, vol. 89, no. 613, pp. 468–489, 1914.

[63] G. Willeke, O. Blenk, C. Kloc, and E. Bucher, "Preparation and electrical transport properties of pyrite (FeS_2) single crystals," *J. Alloys Compd.*, vol. 178, no. 1–2, pp. 181–191, Feb. 1992.

[64] S. Ushioda, "Raman scattering from phonons in iron pyrite (FeS_2)," *Solid State Commun.*, vol. 10, no. 3, pp. 307–310, Feb. 1972.

[65] R. M. Macfarlane, S. Ushioda, and K. W. Blazey, "Resonant Raman scattering from FeS_2 (pyrite)," *Solid State Commun.*, vol. 14, no. 9, pp. 851–855, May 1974.

[66] E. Anastassakis, "Light scattering and ir measurements in XS2 pryite-type compounds," *J. Chem. Phys.*, vol. 64, no. 9, p. 3604, Aug. 1976.

[67] A. Schlegel and P. Wachter, "Optical properties, phonons and electronic structure of iron pyrite (FeS 2)," *J. Phys. C Solid State Phys.*, vol. 9, no. 17, pp. 3363–3369, Sep. 1976.

[68] H. D. Lutz, G. Kliche, and H. Haeuseler, "Far-Infrared Reflection Spectra, Optical and Dielectric Constants," pp. 2–8, 1981.

[69] H. D. Lutz, G. Kliche, and H. Haeuseler, "Lattice Vibration Spectra XXIV*. Far-Infrared Reflection Spectra, Optical and Dielectric Constants, and Effective Charges of the Pyrite Type Compounds FeS_2, MnS2, $MnSe_2$, and $MnTe_2$," *Zeitschrift für Naturforsch. A*, vol. 36, no. 2, pp. 184–190, Jan. 1981.

[70] H. A. Lauwers and M. A. Herman, "Force field of FeS_2 with pyrite structure at zero wave vector," *J. Phys. Chem. Solids*, vol. 37, no. 9, pp. 831–834, Jan. 1976.

[71] C. M. Hartwig, E. Wiener-Avnear, and S. P. S. Porto, "Analysis of the Temperature-Dependent Phonon Structure in Sodium Nitrite by Raman Spectroscopy," *Phys. Rev. B,*

vol. 5, no. 1, pp. 79–91, Jan. 1972.

[72] W. Shockley and H. J. Queisser, “Detailed Balance Limit of Efficiency of p-n Junction Solar Cells,” *J. Appl. Phys.*, vol. 32, no. 3, p. 510, Jun. 1961.

[73] P. P. Altermatt, T. Kiesewetter, K. Ellmer, and H. Tributsch, “Specifying targets of future research in photovoltaic devices containing pyrite (FeS_2) by numerical modelling,” *Sol. Energy Mater. Sol. Cells*, vol. 71, no. 2, pp. 181–195, Feb. 2002.

[74] K. P. Bhandari *et al.*, “Analysis and characterization of iron pyrite nanocrystals and nanocrystalline thin films derived from bromide anion synthesis,” *J. Mater. Chem. A*, vol. 3, no. 13, pp. 6853–6861, Mar. 2015.

[75] L. Samad, M. Cabán-Acevedo, M. J. Shearer, K. Park, R. J. Hamers, and S. Jin, “Direct Chemical Vapor Deposition Synthesis of Phase-Pure Iron Pyrite (FeS 2) Thin Films,” *Chem. Mater.*, vol. 27, no. 8, pp. 3108–3114, Apr. 2015.

[76] A. Ennaoui *et al.*, “Iron disulfide for solar energy conversion,” *Sol. Energy Mater. Sol. Cells*, vol. 29, no. 4, pp. 289–370, May 1993.

[77] S. W. Lehner, K. S. Savage, and J. C. Ayers, “Vapor growth and characterization of pyrite (FeS_2) doped with Co, Ni, and As: Variations in semiconducting properties,” *J. Cryst. Growth*, vol. 286, no. 2, pp. 306–317, Jan. 2006.

[78] C. Uhlig, E. Guenes, A. S. Schulze, M. T. Elm, P. J. Klar, and S. Schlecht, “Nanoscale FeS_2 (Pyrite) as a Sustainable Thermoelectric Material,” *J. Electron. Mater.*, vol. 43, no. 6, pp. 2362–2370, Feb. 2014.

[79] O. Blenk, E. Bucher, and G. Willeke, “p-type conduction in pyrite single crystals prepared by chemical vapor transport,” *Appl. Phys. Lett.*, vol. 62, no. 17, p. 2093, Apr. 1993.

[80] K. Kato, Y. Okamoto, J. Morimoto, and T. Miyakawa, “The thermoelectric properties of FeS_2,” *J. Mater. Sci. Lett.*, vol. 16, no. 11, pp. 914–916, Jun. 1997.

[81] D. J. Vaughan and J. R. Craig, *Mineral Chemistry of Metal Sulfides*. Cambridge University Press, 1978.

[82] J. R. Ares *et al.*, “Evolution of the Seebeck coefficient during the formation and crystallization of pyrite thin films,” *J. Phys. Condens. Matter*, vol. 10, no. 19, pp. 4281–4289, May 1998.

[83] M. Morsli, A. Bonnet, L. Cattin, A. Conan, and S. Fiechter, “Electrical Properties of a Synthetic Pyrite FeS 2 Non Stoichiometric Crystal,” *J. Phys. I*, vol. 5, no. 6, pp. 699–705, Jun. 1995.

[84] K. Sato, “Reflectivity Spectra and Optical Constants of Pyrites (FeS 2 , CoS 2 and NiS 2)

between 0.2 and 4.4 eV," *J. Phys. Soc. Japan*, vol. 53, no. 5, pp. 1617–1620, May 1984.

[85] J. Puthussery, S. Seefeld, N. Berry, M. Gibbs, and M. Law, "Colloidal iron pyrite (FeS_2) nanocrystal inks for thin-film photovoltaics.," *J. Am. Chem. Soc.*, vol. 133, no. 4, pp. 716–9, Feb. 2011.

[86] A. K. Abass, Z. A. Ahmed, and R. E. Tahir, "Interband transitions of chemically deposited pyrite FeS_2 films in the fundamental absorption region between 1 and 3.8 eV," *Phys. status solidi*, vol. 97, no. 1, pp. 243–247, Sep. 1986.

[87] X. Chen, Z. Wang, X. Wang, J. Wan, J. Liu, and Y. Qian, "Single-source approach to cubic FeS_2 crystallites and their optical and electrochemical properties," *Inorg. Chem.*, vol. 44, pp. 951–954, 2005.

[88] D. Colombara *et al.*, "Crystal growth of Cu2ZnSnS4 solar cell absorber by chemical vapor transport with I2," *J. Cryst. Growth*, vol. 364, pp. 101–110, Feb. 2013.

[89] S. Levcenco *et al.*, "Influence of anionic substitution on the electrolyte electroreflectance study of band edge transitions in single crystal Cu2ZnSn(SxSe1−x)4 solid solutions," *Opt. Mater. (Amst).*, vol. 34, no. 8, pp. 1362–1365, Jun. 2012.

[90] L. A. Burton *et al.*, "Synthesis, Characterization, and Electronic Structure of Single-Crystal SnS, Sn 2 S 3 , and SnS 2," *Chem. Mater.*, vol. 25, no. 24, pp. 4908–4916, Dec. 2013.

[91] T. Shibata, T. Miura, T. Kishi, and T. Nagai, "Synthesis of single crystal SnS2 by chemical vapor transport method at low temperature using reverse temperature gradient," *J. Cryst. Growth*, vol. 106, no. 4, pp. 593–604, Dec. 1990.

[92] S. Fiechter, J. Mai, A. Ennaoui, and W. Szacki, "Chemical vapour transport of pyrite (FeS_2) with halogen (Cl, Br, I)," *J. Cryst. Growth*, vol. 78, no. 3, pp. 438–444, Dec. 1986.

[93] D. Siebert, J. Dahlem, S. Fiechter, and A. Hartmann, "An ESR Investigation of Synthetic Pyrite Crystals," *Zeitschrift für Naturforsch. A*, vol. 44, no. 1, pp. 59–66, Jan. 1989.

[94] E. K. Li, K. H. Johnson, D. E. Eastman, and J. L. Freeouf, "Localized and Bandlike Valence-Electron States in Fe S 2 and Ni S 2," *Phys. Rev. Lett.*, vol. 32, no. 9, pp. 470–472, Mar. 1974.

[95] S. G. Kwon and T. Hyeon, "Colloidal chemical synthesis and formation kinetics of uniformly sized nanocrystals of metals, oxides, and chalcogenides.," *Acc. Chem. Res.*, vol. 41, no. 12, pp. 1696–709, Dec. 2008.

[96] W. Li, M. Döblinger, A. Vaneski, A. L. Rogach, F. Jäckel, and J. Feldmann, "Pyrite nanocrystals: shape-controlled synthesis and tunable optical properties via reversible self-assembly," *J. Mater. Chem.*, vol. 21, no. 44, p. 17946, Nov. 2011.

[97] A. Kirkeminde and S. Ren, “Thermodynamic control of iron pyrite nanocrystal synthesis with high photoactivity and stability,” *J. Mater. Chem. A*, vol. 1, no. 1, p. 49, 2013.

[98] H. A. Macpherson and C. R. Stoldt, “Iron pyrite nanocubes: size and shape considerations for photovoltaic application.,” *ACS Nano*, vol. 6, no. 10, pp. 8940–9, Oct. 2012.

[99] *Nanoscale Materials in Chemistry*. John Wiley & Sons, 2009.

[100] M. Ibáñez *et al.*, “Crystallographic Control at the Nanoscale To Enhance Functionality: Polytypic Cu 2 GeSe 3 Nanoparticles as Thermoelectric Materials,” *Chem. Mater.*, vol. 24, no. 23, pp. 4615–4622, Dec. 2012.

[101] M. Ibáñez *et al.*, “Core-shell nanoparticles as building blocks for the bottom-up production of functional nanocomposites: PbTe-PbS thermoelectric properties.,” *ACS Nano*, vol. 7, no. 3, pp. 2573–86, Mar. 2013.

[102] M. Ibáñez *et al.*, “Composition Control and Thermoelectric Properties of Quaternary Chalcogenide Nanocrystals: The Case of Stannite Cu 2 CdSnSe 4,” *Chem. Mater.*, vol. 24, no. 3, pp. 562–570, Feb. 2012.

[103] M. Iba *et al.*, “Cu 2 ZnGeSe 4 Nanocrystals: Synthesis and Thermoelectric Properties,” *J. Am. Chem. Soc.*, vol. 130, pp. 4060–4063, 2012.

[104] D. V Talapin, J.-S. Lee, M. V Kovalenko, and E. V Shevchenko, “Prospects of colloidal nanocrystals for electronic and optoelectronic applications.,” *Chem. Rev.*, vol. 110, no. 1, pp. 389–458, Jan. 2010.

[105] A. Ennaoui, S. Fiechter, G. Smestad, and H. Tributsch, “Preparation of Iron Disulfide and its use for Solar Energy Conversion,” in *1st. World Renewable Energy Congress. Vol. 1 pages 458-464 Pergamon Press, 23-28 September 1990*, 1990.

[106] M. Cabán-Acevedo *et al.*, “Ionization of high-density deep donor defect states explains the low photovoltage of iron pyrite single crystals.,” *J. Am. Chem. Soc.*, vol. 136, no. 49, pp. 17163–79, Dec. 2014.

[107] C. Wadia, a P. Alivisatos, and D. M. Kammen, “Materials availability expands the opportunity for large-scale photovoltaics deployment.,” *Environ. Sci. Technol.*, vol. 43, no. 6, pp. 2072–7, Mar. 2009.

[108] D. Zhang, X. L. Wang, Y. J. Mai, X. H. Xia, C. D. Gu, and J. P. Tu, “Enhanced electrochemical performance of FeS_2 synthesized by hydrothermal method for lithium ion batteries,” *J. Appl. Electrochem.*, vol. 42, no. 4, pp. 263–269, Feb. 2012.

[109] L. Yu *et al.*, “Iron Chalcogenide Photovoltaic Absorbers,” *Adv. Energy Mater.*, vol. 1, no. 5, pp. 748–753, Oct. 2011.

[110] T. Hogan *et al.*, “Complex bismuth chalcogenides as thermoelectrics,” in *XVI ICT “97.*

Proceedings ICT''97. 16th International Conference on Thermoelectrics (Cat. No.97TH8291), 1997, pp. 459–462.

[111] M. Ibáñez *et al.*, "Electron doping in bottom-up engineered thermoelectric nanomaterials through HCl-mediated ligand displacement.," *J. Am. Chem. Soc.*, vol. 137, no. 12, pp. 4046–9, Apr. 2015.

[112] G. J. Snyder and E. S. Toberer, "Complex thermoelectric materials.," *Nat. Mater.*, vol. 7, no. 2, pp. 105–14, Feb. 2008.

[113] K. A. Shore, "Electronic Processes in Non-crystalline Materials (Second Edition), by N.F. Mott and E.A. Davis," *Contemp. Phys.*, vol. 55, no. 4, pp. 337–337, Jun. 2014.

[114] M. Davidson and M. Abramowitz, "Optical Microscopy," 1999. [Online]. Available: http://www.olympusmicro.com/primer/opticalmicroscopy.html. [Accessed: 07-Jul-2015].

[115] F. Grønvold and E. F. Westrum, "Heat capacities of iron disulfides Thermodynamics of marcasite from 5 to 700 K, pyrite from 300 to 780 K, and the transformation of marcasite to pyrite," *J. Chem. Thermodyn.*, vol. 8, no. 11, pp. 1039–1048, Nov. 1976.

[116] A. D. Rakic, A. B. Djurišic, J. M. Elazar, and M. L. Majewski, "Optical Properties of Metallic Films for Vertical-Cavity Optoelectronic Devices," *Appl. Opt.*, vol. 37, no. 22, p. 5271, Aug. 1998.

[117] L. Lu, G. Burkey, I. Halaciuga, and D. V Goia, "Core-shell gold/silver nanoparticles: synthesis and optical properties.," *J. Colloid Interface Sci.*, vol. 392, pp. 90–5, Feb. 2013.

[118] Y. Kim, R. C. Johnson, J. Li, J. T. Hupp, and G. C. Schatz, "Synthesis, linear extinction, and preliminary resonant hyper-Rayleigh scattering studies of gold-core/silver-shell nanoparticles: comparisons of theory and experiment," *Chem. Phys. Lett.*, vol. 352, no. 5–6, pp. 421–428, Feb. 2002.

[119] T. B. Jones, "Basic theory of dielectrophoresis and electrorotation," *IEEE Eng. Med. Biol. Mag.*, vol. 22, no. 6, pp. 33–42, Nov. 2003.

[120] X. Yu, A. Shavel, X. An, Z. Luo, M. Ibáñez, and A. Cabot, "Cu(2)ZnSnS(4)-Pt and Cu(2)ZnSnS(4)-Au heterostructured nanoparticles for photocatalytic water splitting and pollutant degradation - Supporting Information," no. 20 mL, pp. 1–8.

APPENDIX

Matlab Codes

calcpml2d, function that calculates the PML parameters on a 2D grid

```
function [sx,sy] = calpml2d(NGRID, NPML)
% CALCPML2D             calculate the PML parameters on a 2D grid
%
% [sx,sy] = calpml2d(NGRID, NPML)
%
% This MATLAB function calculates the PML parameters sx and sy
% to absorb outgoing waves on a 2D grid
%
% Input Arguments
% ================
% NGRID Array containing the number of points in the grid
%       = [ Nx Ny ]
% NPML Array containing the size of the PML at each boundary
%      = [ Nxlo Nxhi Nylo Nyhi ]
%
% Output Arguments
% ================
% sx,sy 2D arrays containing the PML parameters on a 2D grid
%

%%%%%%%%%%%%%%%%%%%%%%%%%%%%%%%%%%%%%%%%%%%%%%%%%%%%%%%%%%%%%%%%%%%%%%%%%%%%%%%
%% Initialize
%%%%%%%%%%%%%%%%%%%%%%%%%%%%%%%%%%%%%%%%%%%%%%%%%%%%%%%%%%%%%%%%%%%%%%%%%%%%%%%

clc;

%%%%%%%%%%%%%%%%%%%%%%%%%%%%%%%%%%%%%%%%%%%%%%%%%%%%%%%%%%%%%%%%%%%%%%%%%%%%%%%
%% Dashboard
%%%%%%%%%%%%%%%%%%%%%%%%%%%%%%%%%%%%%%%%%%%%%%%%%%%%%%%%%%%%%%%%%%%%%%%%%%%%%%%
N0   = 376.73032165;                %free space impedance
amax = 3;
cmax = 1;
p    = 3;
Nx2  = NGRID(1)*2;
Ny2  = NGRID(2)*2;
Nxlo = NPML(1);
Nxhi = NPML(2);
```

```
Nylo = NPML(3);
Nyhi = NPML(4);


%%%%%%%%%%%%%%%%%%%%%%%%%%%%%%%%%%%%%%%%%%%%%%%%%%%%%%%%%%%%%%%%%%%%%%%%
%% PML
%%%%%%%%%%%%%%%%%%%%%%%%%%%%%%%%%%%%%%%%%%%%%%%%%%%%%%%%%%%%%%%%%%%%%%%%

% Initialization of [sx sy]
sx = ones(Nx2,Ny2);
sy = ones(Nx2,Ny2);


% Add Xlo PML
for nx = 1 : Nxlo
   cx = cmax * (sin (pi*nx/(2*Nxlo)))^2;
   ax = 1 + amax * (nx/Nxlo)^p
   sx(Nxlo-nx+1,:) = ax * ( 1 +1i*N0*cx);
end


% Add Xhi PML
for nx = 1 : Nxhi
   cx = cmax * (sin (pi*nx/(2*Nxhi)))^2;
   ax = 1 + amax * (nx/Nxhi)^p
   sx(Nx2-Nxhi+nx,:) = ax * ( 1 +1i*N0*cx);
end

% Add Ylo PML
for ny = 1 : Nylo
   cy = cmax * (sin (pi*ny/(2*Nylo)))^2;
   ay = 1 + amax * (ny/Nylo)^p
   sy(:,Nylo-ny+1) = ay * ( 1 +1i*N0*cy);
end

% Add Yhi PML
for ny = 1 : Nyhi
   cy = cmax * (sin (pi*ny/(2*Nyhi)))^2;
   ay = 1 + amax * (ny/Nyhi)^p
   sy(:,Ny2-Nyhi+ny) = ay * ( 1 +1i*N0*cy);
end
```

Yeeder, function that constructs Yee Grid Derivative operators on a 2D grid

```
function [DEX,DEY,DHX,DHY] = yeeder(NGRID,RES,BC,kinc)
% YEEDER Construct Yee Grid Derivative Operators on a 2D Grid
%
% [DEX,DEY,DHX,DHY] = yeeder(NGRID,RES,BC,kinc);
%
% Note for normalized grid, use this function as follows:
%
% [DEX,DEY,DHX,DHY] = yeeder(NGRID,k0*RES,BC,kinc/k0);
%
% Input Arguments
% ================
% NGRID [Nx Ny] grid size
% RES [dx dy] grid resolution of the 1X grid
% BC [xbc ybc] boundary conditions
% -2: periodic (requires kinc)
% 0: Dirichlet
% kinc [kx ky] incident wave vector
% This argument is only needed for periodic boundaries.
%
% Note: For normalized grid coordinates, you may need to use
% [DEX,DEY,DHX,DHY] = yeeder(NGRID,k0*RES,BC,kinc/k0);


%%%%%%%%%%%%%%%%%%%%%%%%%%%%%%%%%%%%%%%%%%%%%%%%%%%%%%%%%%%%%%%%%%%%%%%
%% Initialize
```

```
%%%%%%%%%%%%%%%%%%%%%%%%%%%%%%%%%%%%%%%%%%%%%%
%%%%%%%%%%%%%%%%%%%%%%%%%%%%
clc;


%%%%%%%%%%%%%%%%%%%%%%%%%%%%%%%%%%%%%%%%%%%%%%
%%%%%%%%%%%%%%%%%%%%%%%%%%%%
%% Dashboard
%%%%%%%%%%%%%%%%%%%%%%%%%%%%%%%%%%%%%%%%%%%%%%
%%%%%%%%%%%%%%%%%%%%%%%%%%%%

a =1; % size of the material
Nx = NGRID(1);
Ny = NGRID(2);
dy = RES(2);
dx = RES(1);

%Nx = 5;
%Ny = 6;
%dy = 1;
%dx = 1;

GAMx  = Nx*dx;
GAMy  = Ny*dy;



%%%%%%%%%%%%%%%%%%%%%%%%%%%%%%%%%%%%%%%%%%%%%%
%%%%%%%%%%%%%%%%%%%%%%%%%%%%
%% Construct the derivative Matrices
%%%%%%%%%%%%%%%%%%%%%%%%%%%%%%%%%%%%%%%%%%%%%%
%%%%%%%%%%%%%%%%%%%%%%%%%%%%

% initialize the matrices
DEX = sparse(Nx*Ny,Nx*Ny);
DEY = sparse(Nx*Ny,Nx*Ny);
DHX = sparse(Nx*Ny,Nx*Ny);
DHY = sparse(Nx*Ny,Nx*Ny);

DIAG = ones(Nx*Ny,1); % Colon vector to put in the diagonal

%%%%%%%%%%%%%%%%%%%%%%%%%%%%%%%%%%%%%%%%%%%%%%
%%%%%%%%%%%%%%%%%%%%%%%%%%%%
%% Derivative matrix for Ex
%%%%%%%%%%%%%%%%%%%%%%%%%%%%%%%%%%%%%%%%%%%%%%
%%%%%%%%%%%%%%%%%%%%%%%%%%%%
```

```
if ((BC(1)+Nx) ~= 1) || ((BC(1)~=0))
    % Put the diagonal terms
    DEX = spdiags(-DIAG,0,DEX);
    DEX = spdiags(DIAG,1,DEX);

    % Boundary condition corrections

    % First Dirichlet

    for i = 1 : Ny-1
        qi = Nx*(i-1) + Nx;
        j = qi+1;
        DEX(qi,j)=0;
    end
    switch BC(1)
        case 0,

        case -1,% Periodic
        for i = 1 : Ny
            qi = Nx*(i-1)+Nx;
            j  = Nx*(i-1) +1;
            DEX(qi,j)= 1;
        end

        case -2,% Pseudo-periodic
            deltapx = exp(1i*kinc(1)*GAMx);
            if (BC(1)+Nx) == -1 % For when Nx == 1 and BC(1) is -2
                deltapx = 1i*abs(deltapx)*kinc(1);
            end
            for i = 1 : Ny
            qi = Nx*(i-1)+Nx;
            j  = Nx*(i-1) +1;
            DEX(qi,j)= deltapx;
        end
    otherwise,
            error('Improper boundary condition.');
    end
    DEX = DEX / dx;
End


%%%%%%%%%%%%%%%%%%%%%%%%%%%%%%%%%%%%%%%%%%%%%%%%
%%%%%%%%%%%%%%%%%%%%%%%%%%%%%%
%% Derivative matrix for Ey
```

```
%%%%%%%%%%%%%%%%%%%%%%%%%%%%%%%%%%%%%%%%%%%%%%%%%%%%%%%%%%%%%%%%%%%%%%%%
%%%%%%%%%%%%%%%%%%%%%%%%%%%%%%%%%%%%%%%%%%%%%%%%%%%%%%%%%%%%%%%%%%%%%%%%

if ((BC(2)+Ny) ~= 1) || ((BC(2)~=0))
   % Put the diagonal terms
   DEY = spdiags(-DIAG,0,DEY);
   DEY = spdiags(DIAG,Nx,DEY); % Takes also care of Dirichlet

   switch BC(2)
      case 0, % Dirichlet

      case -1,% Periodic
         for i = 1 : Nx
            qi = Nx*(Ny-1) +i;
            j = i;
            DEY(qi,j)= deltapy;
         end

      case -2,% Pseudo Periodic
         deltapy = exp(1i*kinc(2)*GAMy);
         if (BC(2)+Ny) == -1 % For when Ny == 1 and BC(2) is -2
            deltapy = 1i*abs(deltapy)*kinc(2);
         end
         for i = 1 : Nx
            qi = Nx*(Ny-1) +i;
            j = i;
            DEY(qi,j)= deltapy;
         end
   otherwise,
         error('Improper boundary condition');
   end
   DEY = DEY / dy;
end
%%%%%%%%%%%%%%%%%%%%%%%%%%%%%%%%%%%%%%%%%%%%%%%%%%%%%%%%%%%%%%%%%%%%%%%%
%%%%%%%%%%%%%%%%%%%%%%%%%%%%%%%%%%%%%%%%%%%%%%%%%%%%%%%%%%%%%%%%%%%%%%%%
%% Derivative matrix for Hx
%%%%%%%%%%%%%%%%%%%%%%%%%%%%%%%%%%%%%%%%%%%%%%%%%%%%%%%%%%%%%%%%%%%%%%%%
%%%%%%%%%%%%%%%%%%%%%%%%%%%%%%%%%%%%%%%%%%%%%%%%%%%%%%%%%%%%%%%%%%%%%%%%

if ((BC(1)+Nx) ~= 1) || ((BC(1)~=0))
   % Put the diagonal terms
   DHX = spdiags(DIAG,0,DHX);
   DHX = spdiags(-DIAG,-1,DHX);
   %full(DHX)

   % First Dirichlet
```

```
    for i = 2 : Ny
        qi = Nx*(i-1) + 1;
        j = qi-1;
        DHX(qi,j)=0;
        end
    switch BC(1)
        case 0,

        case -1,% Periodic
            for i = 1 : Ny
                qi = Nx*(i-1)+ 1;
                j = Nx*(i-1) + Nx;
                DHX(qi,j)= -1;
            end

        case -2,% Pseudo-Periodic
            deltapx = exp(-1i*kinc(1)*GAMx);
            if (BC(1)+Nx) == -1 % For when Nx == 1 and BC(1) is -2
                deltapx = -1i*abs(deltapx)*kinc(1);
            end
            for i = 1 : Ny
                qi = Nx*(i-1)+ 1;
                j = Nx*(i-1) + Nx;
                DHX(qi,j)= -deltapx;
            end

        otherwise,
                error('Improper boundary condition');
    end
    DHX = DHX / dx;
end
%%%%%%%%%%%%%%%%%%%%%%%%%%%%%%%%%%%%%%%%%%%%%%%%%%%%%%%%%%%%%%%%%%%%%%%
%% Derivative matrix for Hy
%%%%%%%%%%%%%%%%%%%%%%%%%%%%%%%%%%%%%%%%%%%%%%%%%%%%%%%%%%%%%%%%%%%%%%%

if ((BC(2)+Ny) ~= 1) || ((BC(2)~=0))
    % Put the diagonal terms
    DHY = spdiags(DIAG,0,DHY);
    DHY = spdiags(-DIAG,-Nx,DHY);  % Already covers Dirichlet

    switch BC(2)
        case -0,% Dirichlet

        case -1,% Periodic
```

```
        for i = 1 : Nx
            j = Nx*(Ny-1) + i;
            DHY(i,j)= -1;
        end

    case -2,% Pseudo Periodic
        deltapy = exp(-1i*kinc(2)*GAMy);
        if (BC(2)+Ny) == -1 % For when Ny == 1 and BC(2) is -2
            deltapy = -1i*abs(deltapy)*kinc(2);
        end
        for i = 1 : Nx
            j = Nx*(Ny-1) + i;
            DHY(i,j)= -deltapy;
        end
    otherwise,
            error('Improper boundary condition.');
  end
  DHY = DHY / dy;
End
```

Fdfd 2d program that performs 2d finite difference frequency domain of different size of iron pyrite nanoparticles

```
% FeS2_particles.m
% Program that calculates the absorption, transmission
% , reflection spectra of FeS2 nanoparticle and plot the different spectra
% It also saves the spectra on a csv file.

% Initialize Matlab

close all;
clc;
clear all;

% Units
micrometers = 1;
nanometers  = 1e-3 * micrometers;
degrees     = pi/180;


%%%%%%%%%%%%%%%%%%%%%%%%%%%%%%%%%%%%%%%%%%%%%%%%%%%%%%%%%%%%%%%%%%%%%%%
%% Dashboard
```

```
%%%%%%%%%%%%%%%%%%%%%%%%%%%%%%%%%%%%%%%%%%%%%%
%%%%%%%%%%%%%%%%%%%%%%%%%%%%%

% Read dielectric constant file
LAM0  = xlsread('FeS2_dielectric.xlsx','A1:A702')' * nanometers;
ereal = xlsread('FeS2_dielectric.xlsx','B1:B702')';
eimag = xlsread('FeS2_dielectric.xlsx','C1:C702')';

% source
MODE = 'H';
theta =  0 * degrees; % the angle of the
NLAM = numel(LAM0);


    % Device parameters
    r =  60* nanometers;

    % Iterate over the wavelength
    while r >= 10*nanometers
        close all;
        % Open figure window
        fig = figure('color','w','Units','normalized','Outerposition',[0 0 1 1]);
        tx = .2 * micrometers;
        ty = 200 * nanometers;
        er1 = 1.0^2;
        er2 = 1.0^2;
        %erf = 1.44^2;
        erf = 4.81;% Chloroform
        NP  = 1; % Can also iterate over the number of nanoparticles

        % Grid parameters
        ermax = max([er1 er2 erf]);
        nmax = sqrt(ermax);
        Nres = 10;
        NDIM = 20; % Make sure that the smaller feature size is at least 10 points
        Buff = max(LAM0) * [0.5 0.5]; % The buffer region needed between the object and the
PML
        NPML = [20 20];


%%%%%%%%%%%%%%%%%%%%%%%%%%%%%%%%%%%%%%%%%%%%%%
%%%%%%%%%%%%%%%%%%%%%%%%%%%%%
        %% Calculate optimized grid

%%%%%%%%%%%%%%%%%%%%%%%%%%%%%%%%%%%%%%%%%%%%%%
%%%%%%%%%%%%%%%%%%%%%%%%%%%%%
```

```
        % Starting resolution
        dx = min(LAM0)/nmax/Nres;
        dy = min(LAM0)/nmax/Nres;

        % Resolve nanoparticles
        nx = ceil(r/dx); % Here the smaller feature size is the radius of the nanoparticle
        if nx < NDIM
            dx = r/NDIM;
        end

        ny = ceil(r/dy);
        if ny < NDIM
            dy = r/NDIM;
        end

        % Size Grid
        Sx = tx;
        Nx = 2*ceil(Sx/dx/2) + 1;
        dx = Sx/Nx;
        Sy = ty + sum(Buff);
        Ny = ceil(Sy/dy) + sum(NPML);
        Sy = Ny*dy;

        % Calculate the 2X grid
        Nx2 = 2*Nx;         dx2 = dx/2;
        Ny2 = 2*Ny;         dy2 = dy/2;

        % Grid Axes
        xa = [0:Nx-1]*dx;
        xa = xa - mean(xa);
        ya = [0:Ny-1]*dy;
        ya = ya - mean(ya);
        xa2 = [0:Nx2-1]*dx2;
        xa2 = xa2 - mean(xa2);
        ya2 = [0:Ny2-1]*dy2;
        ya2 = ya2 - mean(ya2);

%%%%%%%%%%%%%%%%%%%%%%%%%%%%%%%%%%%%%%%%%%%%%%%%%%%%%%
%%%%%%%%%%%%%%%%%%%%%%%%%%%%%%%%%
        %% Build device on grid

%%%%%%%%%%%%%%%%%%%%%%%%%%%%%%%%%%%%%%%%%%%%%%%%%%%%%%
%%%%%%%%%%%%%%%%%%%%%%%%%%%%%%%%%

        % Initialize to free space
```

```
ER2 = ones(Nx2,Ny2);
UR2 = ones(Nx2,Ny2);

% Create device
ny1 = 2*NPML(1) + round(Buff(1)/dy2) +1;
ny2 = ny1 + round(ty/dy2) - 1;
ER2(:,1:ny1-1) = er1;
ER2(:,ny1:ny2) = erf;
ER2(:,ny2+1:Ny2) = er2;

% Randomly add Nanoparticles
erfes2 = zeros(NLAM);
erfes2(1) = ereal(1) + 1i*eimag(1);
[ER2] = rand_particles(NP,ny1,dy2,ty,ER2,Sy,Sx,xa2,ya2,r,erfes2,nanometers);


% Initialize data records
REF = zeros(1,NLAM);
TRN = zeros(1,NLAM);
CON = zeros(1,NLAM);
%
% Main Loop -- Iterate over wavelengths
%
for nlam = 1 : NLAM

   if nlam ~= 1
      % Replace the dielectric constant of the previous
      % wavelength with the new dielectric constant
      erfes2(nlam) = ereal(nlam) + 1i*eimag(nlam);
      ER2(ER2 == erfes2(nlam-1)) = erfes2(nlam);
   end

   % Show device
   subplot(231)
   imagesc(xa2,ya2,real(ER2'));
   axis equal tight;
   colorbar;
   title('ER2');
   colormap jet;
   drawnow;
```

```
%%%%%%%%%%%%%%%%%%%%%%%%%%%%%%%%%%%%%%%%%%
%%%%%%%%%%%%%%%%%%%%%%%%%%%
    %% Perform FDFD analysis

%%%%%%%%%%%%%%%%%%%%%%%%%%%%%%%%%%%%%%%%%%
%%%%%%%%%%%%%%%%%%%%%%%%%%%

    % Incorporate PML
    NGRID   = [Nx2 Ny2];
    [sx,sy] = calcpml2d(NGRID,[0 0 2*NPML]);
    ERxx    = ER2./sx.*sy;
    ERyy    = ER2.*sx./sy;
    ERzz    = ER2.*sx.*sy;
    URxx    = UR2./sx.*sy;
    URyy    = UR2.*sx./sy;
    URzz    = UR2.*sx.*sy;

    % Parse to 1X GRID
    ERxx = ERxx(2:2:Nx2,1:2:Ny2);
    ERyy = ERyy(1:2:Nx2,2:2:Ny2);
    ERzz = ERzz(1:2:Nx2,1:2:Ny2);

    URxx = URxx(1:2:Nx2,2:2:Ny2);
    URyy = URyy(2:2:Nx2,1:2:Ny2);
    URzz = URzz(2:2:Nx2,2:2:Ny2);

    % Diagonalize material
    ERxx = diag(sparse(ERxx(:)));
    ERyy = diag(sparse(ERyy(:)));
    ERzz = diag(sparse(ERzz(:)));
    URxx = diag(sparse(URxx(:)));
    URyy = diag(sparse(URyy(:)));
    URzz = diag(sparse(URzz(:)));

    % Get next wavelength
    lam0 = LAM0(nlam);
    % Compute source terms
    k0   = 2*pi/lam0;
    ninc = sqrt(ER2(1,1)*UR2(1,1)); % Refractive index where source injected
    kinc = (k0*ninc)*[sin(theta);cos(theta)];

    % Build derivative matrices
    NGRID = [Nx Ny];
    Res   = [dx dy];
```

```
BC    = [-2 0];
[DEX,DEY,DHX,DHY] = yeeder(NGRID,k0*Res,BC,kinc/k0);

% Construct wave matrix
if MODE == 'E'
   A = DHX/URyy*DEX + DHY/URxx*DEY + ERzz; % E mode
elseif  MODE == 'H'
   A = DEX/ERyy*DHX + DEY/ERxx*DHY + URzz; % H mode
else
   error('Unrecognized mode.');
end
% Calculate source field
[Y X] = meshgrid(ya,xa);
fsrc = exp(1i*(kinc(1)*X + kinc(2)*Y));

% Show source
subplot(232)
imagesc(xa2,ya2,real(fsrc'));
axis equal tight;
colorbar;
title('source');
drawnow;


% Construct q matrix
nys = NPML(1) + 2; % where to record the reflected field from the device
Q = zeros(Nx,Ny);
Q(:,1:nys) = 1; % Everywhere there is a zeros it is total and 1 is for scattered fields
Q = diag(sparse(Q(:)));

% Compute source vector
b = (Q*A - A*Q)*fsrc(:);


% Solve for field
f = A\b;
f = reshape(f,Nx,Ny); % reshape f to a matrix, as it is a column vector

% Show field
subplot(233)
imagesc(xa2,ya2,real(f'));
axis equal tight;
colorbar;
title('field');
drawnow;
```

```
% Extract reflected and transmitted fields
nyr  = NPML(1) + 1;
nyt  = Ny - NPML(2) -1;
Eref = f(:,nyr);
Etrn = f(:,nyt);

% Wave vector expansion
m    = [-floor(Nx/2):floor(Nx/2)]';
kx   = kinc(1) - 2*pi*m/Sx;
nref  = sqrt(ER2(1,1)*UR2(1,1));
ntrn  = sqrt(ER2(1,Ny2)*UR2(1,Ny2));
kyref = -sqrt((k0*nref)^2 - kx.^2);
kytrn = sqrt((k0*ntrn)^2 - kx.^2);


% Remove phase tilt
Eref = Eref./fsrc(:,nyr);
Etrn = Etrn./fsrc(:,nyr);

% Calculate Plane wave amplitude
Aref = flipud(fftshift(fft(Eref)))/Nx;
Atrn = flipud(fftshift(fft(Etrn)))/Nx;

% Reflectance and transmittance
R = abs(Aref).^2.*real(-kyref/kinc(2));
if MODE == 'E'
   T = abs(Atrn).^2.*real(kytrn/kinc(2));
else
   T = abs(Atrn).^2.*real(er1*kytrn/kinc(2)/er2);
end
REF(nlam) = sum(R);
TRN(nlam) = sum(T);
CON(nlam) = REF(nlam) + TRN(nlam);
ABS(nlam) = 1 - CON(nlam);

% Report results
subplot(212);
plot(LAM0(1:nlam)/nanometers,REF(1:nlam),'r');
hold on
%plot(LAM0(1:nlam)/nanometers,TRN(1:nlam),'b');
plot(LAM0(1:nlam)/nanometers,1-CON(1:nlam),'-k');
%hold off
xlim([min(LAM0) max(LAM0)]/nanometers);
ylim([0 1.01]);
legend('Reflectance','Absorption');
```

```
        drawnow;

    end

    r1 =  2*r*1000;
    csvFilename = strcat('Abs_FeS2_', num2str(r1), 'nm_', num2str(NP), 'nano_chloroform');
    jpgFilename = strcat('Abs_FeS2_', num2str(r1), 'nm_', num2str(NP),
'nano_chloroform.jpg');
    csvwrite(csvFilename,[LAM0',REF',ABS']); % Save the reflection and the absorption
    saveas(fig,jpgFilename);                % Save the figure
    r = r - 5 * nanometers;
  end
```